Chiral Vibration Bands in ^{104,106}Mo and High Neutron Yields for Ba-Mo and Ce-Zr from Spontaneous Fission of ^{252}Cf

By

Brooks Musangu Musangu

Dissertation

Submitted to the Faculty of the

Graduate School of Vanderbilt University

in partial fulfillment of the requirements

for the degree of

DOCTOR OF PHILOSOPHY

in

Physics

March 31st, 2021

Nashville, Tennessee

Approved:

Professor Joseph Hamilton, Ph.D.

Professor Akunuri Ramayya, Ph.D.

Professor Sait Umar, Ph.D.

Professor David Ernst, Ph.D.

Professor William Holmes, Ph.D.

To my family, friends and mentors,

and the whole scientific community.

ACKNOWLEDGMENTS

The work accomplished while at Vanderbilt University was made possible by the help of many people and it would be impossible to name them all. However, it would be very remiss of me if I don't acknowledge certain key players.

First and foremost, I would like to acknowledge my privilege and opportunity to work with some of the world renown nuclear physicist; Profs. Joseph H. Hamilton and, now retired, Akunuri Ramayya. Their advise and mentorship has helped me grow into a well rounded scientist. I would also like to say thank you to Dr. William Brantley, my academic advisor from Furman University without whom I would not have met Prof. Hamilton. Not forgetting other committee members: Professor Sait Umar, Ph.D., Professor David Ernst, Ph.D. and Professor William Holmes, Ph.D.. Additionally, my former lab mates Drs. En-hong Wang, Christopher Zachary and Jonathan Eldridge. Their continued support fostered a great working environment. Thank you also to our collaborators; Drs. S. Jehangir, G. H. Bhat, J. A. Sheikh, S. Frauendorf and A. C. Dai.

And lastly, I would like to thank my family for all the love and support their have shown to me. My friends for their support, especially Bubotu Hachitapika, and my church family.

The work at Vanderbilt University and Lawrence Berkeley National Laboratory are supported by the US Department of Energy under Grant No. DE-FG05-88ER40407 and Contract No. DE-AC03-76SF00098. The work at Tsinghua University was supported by the National Natural Science Foundation of China under Grant No. 11175095. The work at JINR was supported by the Russian Foundation for Basic Research Grant No. 08-02-00089 and by the INTAS Grant No. 03-51-4496. S. F. acknowledges support by the US Department of Energy under Grant DF-FG02-95ER40934.

Thank you, also, to the reader of this thesis.

TABLE OF CONTENTS

LIST OF TABLES

LIST OF FIGURES

Chapter 1

Introduction: The Fundamentals of Nuclear Physics

1.1 The Big Picture

Understanding atomic nuclei is a quantum many-body problem of incredible richness and diversity, and studies of nuclei address some of the great challenges that are common throughout modern science. In this thesis, the role of nuclear physics in providing a better description of the nuclear model will be reviewed in the context of the nuclear structure. Particular attention will be given to the high spin states of the neutron-rich ^{104,106}Mo nuclei which have been reinvestigated by analyzing the γ-rays in the spontaneous fission of ^{252}Cf with Gammasphere data. The results will show a definite form of a class of chiral vibrational bands. Furthermore, nuclear fission reaction processes will be reviewed in the context of neutron multiplicity yields of Ba-Mo, Ce-Zr, Te-Pd, and Nd-Sr fragment fission pairs. It will be demonstrated that the Ba-Mo and Ce-Zr fragment fission pairs exhibit a rare fission mode known as "extra-hot fission mode".

The primary goal of science is to build knowledge about the natural world by studying and probing the systems in it, thereby, drawing meaning from it. This knowledge is open to question and revision upon the discovery of new ideas and new evidence. Nature has dealt us with some really complicated systems such as the brain and its complex neural networks, and in nuclear physics, it's the nucleus. All these systems have so many moving parts, such that, when one probes into these systems, the data obtained are very complex and have high dimensionality. Consequently, making the analysis of the data very challenging. In nuclear physics, an ultimate goal is to understand the nucleus in terms of a nuclear model. Such a model would give a detailed description of what a nucleus is, it's constituents and how it interacts with matter. In other words, the model would tell us everything there is to know about the nucleus.

We know that an atom is made of electrons, protons and neutrons. We understand fairly well how small nuclei (containing a couple of protons and neutrons) behave. However, what if there are hundreds protons and neutrons? How does this change the system? How does one go about analyzing such a system? These are the kinds of problems that nuclear physicists are thinking of. And if there was a model to provide answers to such questions simultaneously, that would be great. Unfortunately, such a model doesn't exist. Therefore, nuclear physicists rethought the problem and broke it down to ask more specific questions, such as: (i) what happens to the shape of the nucleus as the number of protons and neutrons increases? (ii) what happens to the energy of the nucleus? (iii) what causes the nucleus to split into pieces? (iv) what happens after a nucleus splits? Such questions are asked to provide insights into what an ideal nuclear model would look like. This is achieved by relying on both experimental data and theoretical interpretation.

Theory recommends observables that are testable experimentally using various means. In the present work, these observables are accessed by means of measuring the γ-rays emitted from excited states in a nucleus populated from spontaneous fission (see chapter 2.2 for more details on this process). Coincidence information is gathered, and with that information inferences are made regarding the quantized energy levels present in a nucleus. A level scheme is built and this picture can lend itself to a structure interpretation. It is also possible to measure the quantum mechanical character of the radiation emitted from a nucleus. The γ radiation can be classified as electric or magnetic and carries angular momentum away from the nucleus. Measurement of these properties can also help identify the spins and parities of nuclear states. However, the question becomes: why should anyone care about such knowledge? There are a few reasons as to why one should care: (a) because it is science (we do it because we love science)–however, in a more practical sense, (b) it is useful for designing better nuclear research facilities, (c) building nuclear energy facilities, and (d) useful in the field of nuclear medicine.

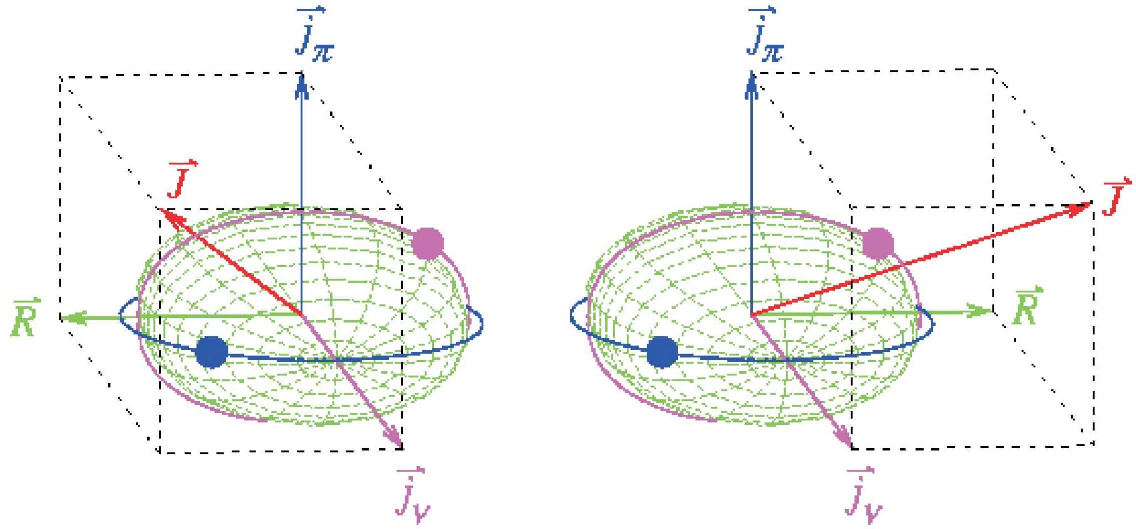

Figure 1.1: The possible alignments of the angular momentum vector in a chiral nucleus. The two alignments result in a pair of nearly degenerate odd-parity bands.

1.2 Motivation

Unlike molecules, nuclei were long thought to be achiral. However, Frauendorf and Meng [7] pointed out in 1997 that triaxial nuclei with significant components of angular momentum along the three principle axes could meet the conditions of nuclear chirality. The conditions they proposed are a particle in a high-j orbital along one axis, a hole in a high-j orbital aligned along another axis, and the rotational angular momentum along the third axis such that the total angular momentum is not aligned along any of the principal axes (see chapter 5 for more details). This configuration is pictured in figure 1.1. The experimental signature for nuclear chirality is two sets of nearly degenerate odd-parity bands corresponding to the two-reflected orientations of the total angular momentum. This experimental signature of a pair of nearly degenerate in energy, $\Delta I=1$ bands, has been found around ^{136}Nd [8] and ^{104,105,106}Rh [9, 10, 11]. Possible perturbed chiral bands related to γ-softness have also been proposaled in ^{106}Ag [12].

If chirality is a global nuclear property, then it might be seen in odd-even or even-even nuclei. Chirality in an even-even nucleus was first proposed for ^{106}Mo by Zhu et al. [13]. The chiral bands were interpreted as soft chiral vibrations with a complex structure where the configuration of quasi-neutrons nearly fills the $g_{7/2}$ orbital (hole) and the $h_{11/2}$ orbital is just beginning to fill (particle). Recent theoretical calculations of all nuclei found that nuclei around ^{108}Ru should have a deformed triaxial shape [14]. The ^{108,110,112}Ru nuclei were searched by Luo et al. [15] for the chiral signature bands, and a set of nearly degenerate bands was found in each nucleus. The discovery of chirality in even-even nuclei, especially that found ^{106}Mo, was the major motivation for the present work given the similarities in the population of ^{104}Mo and ^{106}Mo. More significantly, with the development of large Ge detector arrays, such as Gammasphere and Eurogam which offer high degree of sensitivity and selectivity, experimental investigations of high spin states of neutron-rich nuclei have been made feasible.

Additionally, ^{252}Cf yields of individual correlated pairs in barium (Z = 56) and molybdenum (Z = 42) binary fission have been observed to undergo fission splits via an extra "hot fission mode" (also called second mode) [3]. In this mode, it has been observed that the Ba-Mo fragment pair emits high neutron multiplicities of 7 to 10 neutrons in spontaneous fission of ^{252}Cf [3, 16, 17]. To explain this phenomenon, theorists have attributed the presence of this mode to a possible hyperdeformation of ^{144,145,146}Ba fragments at scission [16, 18, 19]. This is justified by referring back to the theory which predicts that a large nuclear deformation is more likely to yield higher neutron multiplicities [20]. Other theorists have raised skepticism, since the hot fission mode has only been observed in Ba-Mo fragment pairs of ^{252}Cf and not in spontaneous fission of ^{248}Cm [21]. However, this private communication [21] has never been published.

Furthermore, some earlier analysis in spontaneous fission of ^{252}Cf did not confirm the second hot mode [5] without reporting the 9 and 10 channel yields (see later discussion), while others did show some irregularity around the eight-neutron channel [4, 22, 23, 24]. Because of the importance of understanding this extra hot fission mode, pairs of Ba-Mo, Ce-Zr, Te-Pd, and Nd-Sr have been studied with improved precision using γ-γ-γ-γ as well as γ-γ-γ coincidence data and the latest level structures of these nuclei. Also, relative intensities of transitions in these nuclei made available through our work likewise improved the accuracy of the analysis. See chapter 4 for the full discussion of the experimental details and results.

Chapter 2

Nuclear Decay

Before a full discussion of the present work, it is important to first discuss basic nuclear radioactive processes and useful mathematical structures and tools for analyses of radioactive processes which are essential concepts for the analyses of nuclear decay. Various atomic nuclei undergo spontaneous decay processes in order to decrease their total energy. There are four main decay modes; spontaneous fission, α decay, β decay, and γ decay. The first two decay modes occur via the strong interaction, β decay is an electroweak process, and γ decay is an electromagnetic process. Spontaneous fission and α decay involve the emission of nucleons, β decay involves the conversion of a proton to a neutron (or vice versa) in order for the nucleus to become more stable, whereas γ decay decreases the energy of the nucleus through transitions from excited nuclear states to (eventually) the ground state. Here, only spontaneous fission (SF), γ decay, and Internal Conversion (IC) will be discussed in full as they are the only decay processes used in this study. The source of information for the introductory material presented here is taken from the following [25, 26] sources unless otherwise stated. Extensive details for all of these decay modes, as well as others not listed here, can be found in the same sources.

2.1 Decay Statistics

Radioactive nuclei are characterized by the rate at which they decay. This rate is given by the decay constant λ, which has dimensions of inverse time. Due to the statistical nature of radioactive decay, no specific prediction can be given for an individual nucleus. The characterization of these decays is reliant instead on decay probabilities. The probability that a nucleus decays within the time interval dt is λdt. Therefore, in a collection of identical radioactive nuclei, the number of decays per unit time is proportional to the number of nuclei that are present:

$$-dN(t) = \lambda N(t)dt \tag{2.1}$$

This result can be integrated to give an expression for the number of nuclei remaining as a function of time known as the exponential decay law:

$$N(t) = N_0 e^{-\lambda t} \tag{2.2}$$

where N_0 is the number of parent nuclei present at t = 0. Equation 2.2 can be used to determine the time required for half of the nuclei present to decay. This is known as the *half-life*, denoted by $t_{1/2}$. By substituting N(t) = N(0)/2 into Eqn. 2.2 and rearranging we obtain:

$$t_{1/2} = \frac{\ln(2)}{\lambda} \tag{2.3}$$

A more physically useful number is the nuclear lifetime, τ, or the average time it takes for a single nucleus to decay. While λ and τ are mathematically convenient, it is traditional to speak of nuclear half-lives, $t_{1/2}$, or the time it takes for half the nuclei to decay (i.e. $N(t_{1/2}) = \frac{1}{2}N_0$). From these definitions it should be obvious that

$$\lambda = \frac{1}{\tau} = \frac{\ln(2)}{t_{1/2}} \tag{2.4}$$

Furthermore, if a nucleus is being produced at a rate, P, then equation 2.1 becomes

$$\frac{\partial N}{\partial t} = P - \lambda N \tag{2.5}$$

for which the solution – if we assume P is constant – is

$$N(t) = \frac{P}{\lambda}\left(1 - e^{-\lambda t}\right) + N_0 e^{-\lambda t} \tag{2.6}$$

Normally, in a case of production, $N_0 = 0$, thus (in terms of τ);

$$N(t) = P\tau\left(1 - e^{-t/\tau}\right) \tag{2.7}$$

If P is not constant, then the solutions to equation 2.5 depend on the form of $P(t)$. In all cases considered in this work, P can be assumed or approximated to be constant.

There are many cases in which there is more than one decay mode of the parent nuclear state. These are known as *multi-modal decays*. For example, if the parent nucleus decays by way of two branches, there would be two distinct decay constants λ_1 and λ_2. These are known as partial decay constants. For the total decay of the parent, $\lambda = \lambda_1 + \lambda_2$, where λ is the total decay constant. These decay constants represent decay rates for each branch of the decay. The branching fraction (or branching ratio) is a measure of the fraction of the total decays that proceed via a given branch:

$$B_1 = \frac{\lambda_1}{\lambda},\ B_2 = \frac{\lambda_2}{\lambda} \text{ and in general } B_n = \frac{\lambda_n}{\lambda} \tag{2.8}$$

where B_n is the branching ratio for the nth branch. Other cases where the daughter nucleus is also unstable and decays to a granddaughter occur as well. These are referred to as *sequential decays*. Sequential decays often lead to large decay chains which may contain many generations of α and β decays, as well as cascades of γ-rays from excited nuclear states.

2.2 Fission

Nuclear fission is a process where an atomic heavy nucleus divides into two (sometimes three) smaller nuclei, plus a few neutrons as given in the equation 2.9

$$^{A}_{Z}X_N \rightarrow {}^{A'}_{Z'}X'_{N'} + {}^{A-A'-x}_{Z-Z'}X''_{N-N'-x} + x\left({}^{1}_{0}n_1\right) + \text{energy} \tag{2.9}$$

The daughters, ${}^{A'}X'$ and ${}^{A-A'-x}X''$, are left in excited states, usually with large spin, in addition to the kinetic energy of both daughters and the x neutrons.

Fission can be either a reaction or decay process depending on whether it is induced or spontaneous, respectively. Fission has a unique importance among nuclear reactions. The discovery of fission, and the developments that proceeded from it, have altered the world forever and have impinged on the consciousness of every literate human being. This process occurs when a nucleus with some degree of deformation absorbs energy, becoming excited and deforms to a configuration know as the "transition state" or "saddle point" configuration. This deformation results in the average distance between the nuclear protons to increase thus, reducing the Coulomb energy. At the same time, the nuclear surface energy increases as the area of the nucleus increases. Therefore, at the saddle point, it is true that the rate of change of the Coulomb energy is equal to the rate of change of the nuclear surface energy. The formation and decay of this transition state nucleus are the rate determining step in the fission process and corresponds to the passage over an activation energy barrier to the reaction. If the nucleus deforms beyond this point it is irretrievably committed to fission. When this happens, then in a very short time, the neck between the nascent fragments disappears and the nucleus divides into two fragments at the "scission point", while emitting neutrons.

In fact, the neutrons emitted by fission are typically emitted by *primary fragments*, the highly excited nuclei directly produced by the fission process, and not emitted in the fission process itself. Fission occurs in stages, with the primary fragments being populated well above their neutron separation energies in under 10^{-20} s during the "saddle to scission" phase. The prompt neutron emission phase occurs when the primary fragments emit neutrons by around 10^{-18} s, producing the excited daughters, or *secondary fragments*, as shown in equation 2.9. At around 10^{-16}s, the daughter nuclei will emit prompt γ-rays, which are the emissaries from the nuclear world studied in this work (as described in section 2.4 below). Finally, from 10^{-6} s to infinity, one will often see β-delayed neutrons and

γ-rays, as the ground states (or isomers) of the secondary fragments β-decay, causing both neutrons and γ-rays to be emitted from their daughters, who also will eventually β-decay, continuing the process until the nuclei decay to stability.

The term "saddle to scission" refers to the path the fissioning nucleus takes from a saddle point in its potential energy surface to the point that the nucleus actually scissions into two distinct nuclei. Fission (and α-decay) occurs by quantum tunneling through a potential energy barrier in the nucleus' deformation potential energy surface. As will be described in greater detail in section 3.3 below, the shape of a nucleus can be described in terms of deformation parameters, β_i, where i represents the multipole order of the electromagnetic field produced by the charge distribution of the nucleus. Figure 2.1a shows the potential energy surface for ^{252}Cf, as a function of β_2 and β_3, along with a few different paths the nucleus might take as it tunnels through the fission barrier to scission. Figure 2.1b shows an one dimensional slice of the potential energy surface, showing the shape of the potential energy barrier that a nucleus must tunnel through before scission.

Equation 2.9 and figure 2.1 assume that it is the ground state of a nucleus that is fissioning. When the ground state of a nucleus fissions without an external stimulus, this is known as *spontaneous fission* (or SF). Spontaneous fission has a long half-life and competes with α decay. Spontaneously fissile nuclides have many useful applications. For example, ^{252}Cf is a very efficient compact energy source for many application. Also, ^{252}Cf is a useful very compact source of neutrons that eliminates the need for accelerators or reactors for many applications. While ^{252}Cf – whose decay products are studied in this work – spontaneously fissions $\sim 3\%$ of the time[1], most fission reactions studied by physicists are *induced fission*. Induced fission occurs when an external stimulus excites the nucleus to an energy where tunneling across the fission barrier is substantially easier, or perhaps even above the barrier altogether;

[1]The other $\sim 97\%$ is α-decay

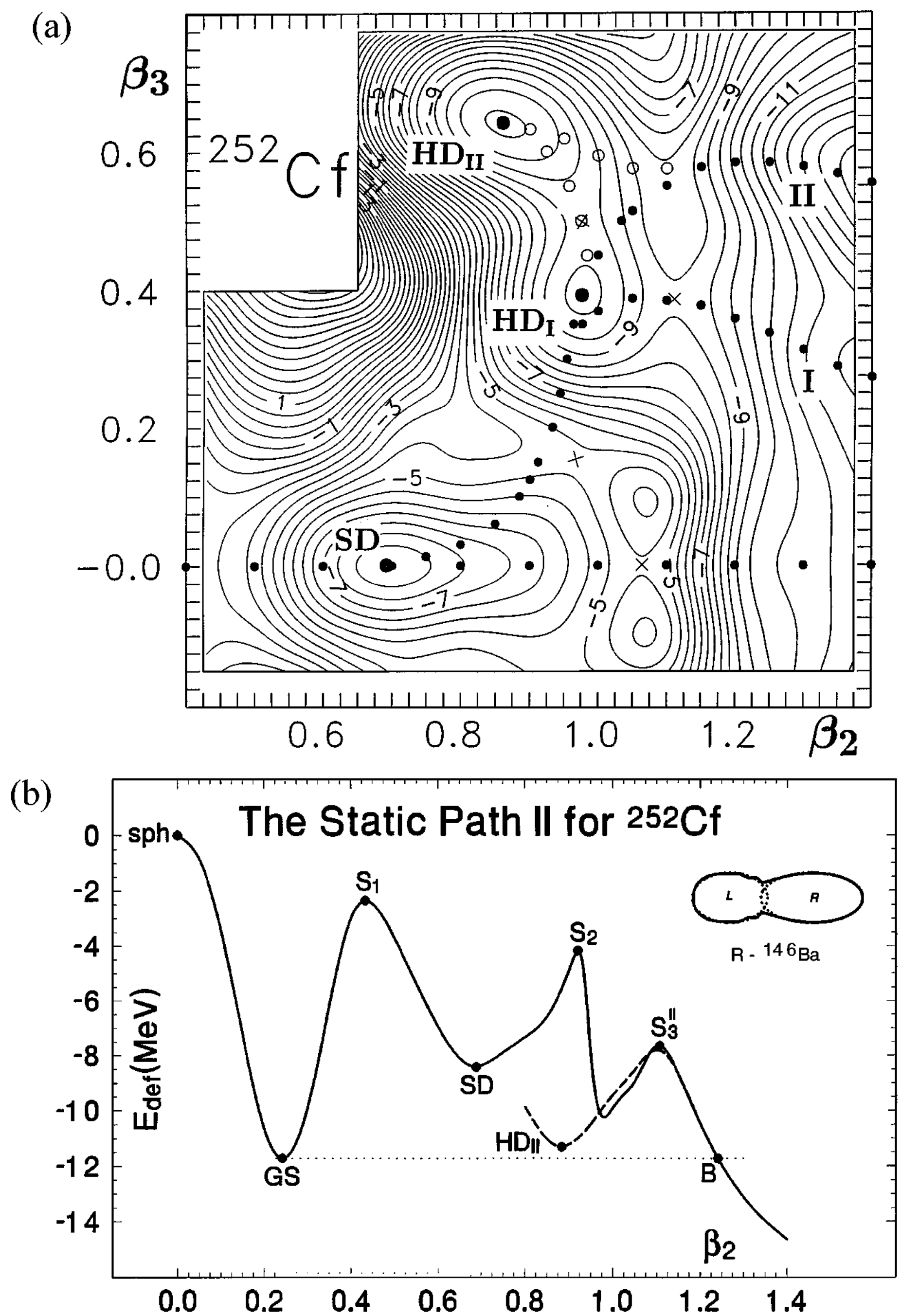

Figure 2.1: (a) A two dimensional potential energy surface for spontaneous fission as a function of quadrupole (β_2) and octupole (β_3) deformation paramaters with dotted lines representing possible paths ^{252}Cf might take toward scission. (b) one dimensional potential for the fission path along $\beta_3 = 0$, with points marked corresponding to points shown in a. Additionally "GS" represents the ground state of ^{252}Cf and "sph" represents the $\beta_2 = \beta_3 = 0$ point of perfect spherical symmetry. This figure is copied from Ter-Akopian *et al.* [16]

$$ {}^{1}_{0}n_1 + {}^{A}_{Z}X_N \rightarrow {}^{A'}_{Z'}X'_{N'} + {}^{A-A'-x+1}_{Z-Z'}X''_{N-N'-x} + x\left({}^{1}_{0}n_1\right) + \text{energy} \tag{2.10} $$

Neutron induced fission is commonly used in nuclear power reactors, because the excess neutrons produced by one fission event can be used to start other fission events, causing a chain reaction. However, neutrons, being neutral, are difficult to accelerate to precise energies, or directions.

$$ {}^{1}_{1}\mathrm{H}_0 + {}^{A}_{Z}X_N \rightarrow {}^{A'}_{Z'}X'_{N'} + {}^{A-A'-x+1}_{Z-Z'+1}X''_{N-N'-x} + x\left({}^{1}_{0}n_1\right) + \text{energy} \tag{2.11} $$

to produce isotopes of interest.

2.3 Types of Nuclear Decay

There are three primary modes of decay for a nucleus, traditionally known as α, β, and γ decay. Alpha decay typically occurs in heavy nuclei, and consists of the emission of a ^{4}He, nucleus;

$$ {}^{A}_{Z}X_N \rightarrow {}^{A-4}_{Z-2}X'_{N-2} + {}^{4}_{2}\mathrm{He}_2 + \text{energy} \tag{2.12} $$

where ${}^{A}_{Z}X_N$ is an arbitrary isotope of an element consisting of Z protons, N neutrons, and $Z+N=A$ total nucleons. Beta decay occurs for nuclei that have too many neutrons resulting in a neutron changing into a proton by emission of an electron and an anti-electron-neutrino;

$$ {}^{A}_{Z}X_N \rightarrow {}_{Z+1}{}^{A}X'_{N-1} + \mathrm{e}^- + \bar{\nu}_e + \text{energy} \tag{2.13} $$

Gamma decay occurs when a nucleus, being in an excited state (often denoted by *), emits a photon;

$$ {}^{A}_{Z}X^{*}_{N} \rightarrow {}^{A}_{Z}X_N + {}^{0}_{0}\gamma_0 \tag{2.14} $$

To iterate, in addition to these three primary modes, nuclei may also decay by SF, IC , positron emission (β^+), orbital electron capture (EC), neutron emission, proton emission, pair production, and cluster emission. Furthermore, a nucleus may be caused to decay by external stimuli in processes such as neutrino absorption, neutron (or otherwise) induced fission, and inverse internal conversion[2].

2.4 γ-Decay

As mentioned earlier, nuclei that are in an excited state generally decay via the emission of a γ-ray or through internal electron conversion to decrease the energy of the nucleus. The transitions can occur between two excited states or an excited state and the ground state. This decrease in energy does not change the isotope, it merely re-configures the nucleons within the nucleus. In the γ-decay process, electromagnetic radiation of a specific energy is released when the nucleus undergoes a transition from an excited state to a lower energy state. With internal conversion, the energy that would be emitted through electromagnetic radiation instead liberates an atomic electron, causing it to move into an unbound state. These two processes generally compete with each other. The study of γ-rays emitted by an excited nucleus has long been a valuable tool in the study of nuclear structure. From the measured observables of γ-rays, many properties of the nuclei that emitted them may be determined.

2.4.1 Multipole Radiation and Magnetic Properties of Nuclei

In order to understand the energy transfer in γ decay, we must consider the initial and final states of the nucleus as well as its recoil momentum. Using conservation of energy and momentum, we obtain:

$$\text{Conservation of Momentum: } \mathbf{p}_R + \mathbf{p}_\gamma = 0 \tag{2.15}$$

$$\text{Conservation of Energy: } E_i = E_f + E_\gamma + T_R \tag{2.16}$$

[2]Only recently observed experimentally; see Chiara *et al.* [27].

$$\text{where: } T_R = \frac{p_R^2}{2M_x} = \frac{p_\gamma^2}{2M_x} = \frac{E_\gamma^2}{2M_x c^2}, \tag{2.17}$$

is the corresponding recoil total energy and is assumed to be non-relativistic. Therefore;

$$\Delta E = E_\gamma + \frac{E_\gamma^2}{2M_x c^2}, \tag{2.18}$$

$$E_\gamma \approx \Delta E(1 - \frac{\Delta E}{2M_x c^2}). \tag{2.19}$$

It can be seen that the energy released in the electromagnetic transition is slightly less than the energy difference between the initial and final nuclear states due to the recoil of the daughter nucleus.

The emitted γ-ray photon can be understood in a simple model using classical electrodynamics, where a radiation field can be described in terms of a multipole expansion. This classical theory is then supplemented using a quantum mechanical description for the electric and magnetic multipoles in terms of the power radiated for each:

$$\lambda_e(L) = \frac{P_e(L)}{\hbar\omega} \text{ and } \lambda_m(L) = \frac{P_m(L)}{\hbar\omega} \tag{2.20}$$

where the subscripts *m* and *e* represent magnetic and electric multipoles, respectively, L is the multipolarity of the respective transition (see Table 2.1), and $E_\gamma = \hbar\omega$, where ω is the angular frequency of the oscillating field.

The decay constants can then be expanded in multipoles by expanding the radiation powers. In order to obtain order of magnitude expressions for the expected transition rates, a number of approximations can be made. These are referred to as the *Weisskopf estimates*. They are: (i) that the initial and final states are given by the single particle wave functions:

$$\Psi_i = R_i(r)Y_{l_i m_i}(\Theta,\Phi) \text{ and } \Psi_f = R_f(r)Y_{l_f m_f}(\Theta,\Phi) \tag{2.21}$$

Table 2.1: Properties and nomenclature for electromagnetic multipole radiation. [28]

Radiation Nomenclature	Symbol	Multipolarity (L)	Parity
Electric Dipole	E1	1	-1
Magnetic Dipole	M1	1	+1
Electric Quadrupole	E2	2	+1
Magnetic Quadrupole	M2	2	-1
Electric Octopole	E3	3	-1
Magnetic Octopole	M3	3	+1
.	.	.	.
.	.	.	.
.	.	.	.

and (ii) the radial terms in the wave functions are constant over the entire nuclear volume, and zero elsewhere. Once these approximations are made, the electric and magnetic multipole decay constants can be expressed as [28]:

$$\lambda_e(L) = \frac{2e^2(L+1)}{4\pi\varepsilon_0\hbar L[(2L+1)!!]^2}\left[\frac{3}{L+3}\right]^2\left(\frac{E_\gamma}{\hbar c}\right)^{2L+1}R^{2L} \tag{2.22}$$

and

$$\lambda_m(L) = \frac{20e^2\hbar(L+1)}{4\pi\varepsilon_0 c^2 m_p^2 L[(2L+1)!!]^2}\left[\frac{3}{L+3}\right]^2\left(\frac{E_\gamma}{\hbar c}\right)^{2L+1}R^{2L-2} \tag{2.23}$$

where R is the nuclear radius, and E_γ is expressed in MeV.

The total angular momentum (L) of the photon is subject to selection rules, which are related to the angular momentum of the initial and final nuclear states by:

$$|J_i - J_f| \leq L \leq J_i + J_f \tag{2.24}$$

where L = 1, 2, 3, ...

It is important to note that the angular selection rules do not include $0 \rightarrow 0$ transitions since they can only be satisfied with L = 0, and there are no L = 0 photons. There are also parity selection rules that are dependent on the angular momentum of the photon,

$$\text{For EL transitions, } \pi_i = \pi_f(-1)^L \tag{2.25}$$

$$\text{For ML transitions, } \pi_i = \pi_f(-1)^{L+1} \tag{2.26}$$

For various initial and final nuclear spin and parity states there are in general a number of allowed γ-ray transitions that can occur. In the case where the lowest multipole permitted by the selection rules is electric, it will dominate the decay. If the lowest allowed multipole L is magnetic, there will, in general, be a competition between ML and E(L+1) multipole radiation.

2.4.2 Reduced Transition Probabilities

The probability per unit time, λ, that a nucleus will undergo a certain transition from state $|J_i\rangle$ to state $|J_f\rangle$ by emitting a photon of energy E and angular momentum L, with either magnetic ($\Pi = M$) or electric ($\Pi = E$) qualities is

$$\lambda(\Pi L; J_i \to J_f) = \frac{8\pi(L+1)}{L((2L+1)!!)^2} \frac{1}{\hbar} \left(\frac{E}{\hbar c}\right)^{2L+1} \left|\left\langle J_f \left| \hat{O}(\Pi L) \right| J_i \right\rangle\right|^2 \tag{2.27}$$

where $\hat{O}$ is the multipole transition operator, and $x!! \equiv 1 \times 3 \times 5 \times \cdots \times x$ is a double factorial. This λ is the same as defined in equation 2.4. It is common to define a reduced transition probability, $B(\Pi L; J_i \to J_f)$, that is independent of energy, and only depends on the nuclear properties of the two states involved. When this is done, equation 2.27 becomes

$$\lambda(\Pi L; J_i \to J_f) = \frac{8\pi(L+1)}{L((2L+1)!!)^2} \frac{1}{\hbar} \left(\frac{E}{\hbar c}\right)^{2L+1} B(\Pi L; J_i \to J_f) \tag{2.28}$$

Greater detail on the derivation of equations 2.27 and 2.28 can be found in Eisenberg and Greiner [29].

The experimental techniques discussed in this work are incapable of directly measuring $B(\Pi L)$ values. However, the ratios of such values for transitions from the same state are still useful. In general when multiple transitions de-excite the same nuclear state, their measured intensities, I, will be proportional to their respective transition probabilities, T. Thus we can use equation 2.28 to find a general relationship between the reduced transition probabilities and measured intensities of transitions from the same state;

$$\frac{B(\Pi_1 L_1; J_i \to J_f)}{B(\Pi_2 L_2; J_i \to J'_f)} = \frac{(L_2+1)L_1((2L_1+1)!!)^2}{(L_1+1)L_2((2L_2+1)!!)^2}(\hbar c)^{2(L_1-L_2)}\frac{J_1 E_2^{2L_2+1}}{J_2 E_1^{2L_1+1}} \tag{2.29}$$

In most cases $\Pi_1 L_1 = \Pi_2 L_2 \equiv \Pi L$, and thus,

$$\frac{B(\Pi L; J_i \to J_f)}{B(\Pi L; J_i \to J'_f)} = \frac{J_1 E_2^{2L+1}}{J_2 E_1^{2L+1}} \tag{2.30}$$

which is an elegantly simple equation useful for calculating experimental $B(\Pi L)$ ratios.

Furthermore, for collective states, especially those involving quadrupole vibrations, the ratio of $B(EL)$ values for transitions out of the same state can be calculated simply by the ratio of the square of Clebsch Gordon Coeficients;

$$\frac{B(EL : J_i \to J_f)}{B(EL : J_i \to J'_f)} = \frac{\langle J_i K_i, L\Delta K | J_f K_f \rangle^2}{\langle J_i K_i, L\Delta K' | J'_f K'_f \rangle^2} \tag{2.31}$$

Where K is the projection of the nuclear spin on the nuclear axis of symetry (usually the same as the spin of the bandhead), and $\Delta K = K_f - K_i$. Equation 2.31 allows one to calculate what are known as Alaga rules which are useful tools giving a first order approximation for $B(E2)$ ratios, and can be very powerful for identifying the K values for various band structures seen in data, thus aiding in the assignment of observed bands with different structure properties. A deeper discussion of Alaga rules can be found in Casten [30].

Equation 2.31 assumes that the properties of the collective bands it connects are unmixed. This assumption is rarely valid for β- and γ-vibrational bands, meaning that the experimental $B(E2)$ ratios rarely match equation 2.31. We can define γ-ground, β-ground, and γ-β mixing parameters respectively as

$$\begin{aligned} Z_\gamma &\equiv \sqrt{24}\varepsilon_\gamma \left(\frac{\langle 00|\hat{O}(E2)|00\rangle}{\langle 12|\hat{O}(E2)|00\rangle} \right) \\ Z_\beta &\equiv 2\varepsilon_\beta \left(\frac{\langle 00|\hat{O}(E2)|00\rangle}{\langle 10|\hat{O}(E2)|00\rangle} \right) \\ Z_{\beta\gamma} &\equiv \sqrt{6}\varepsilon_{\beta\gamma} \left(\frac{\langle 12|\hat{O}(E2)|00\rangle}{\langle 10|\hat{O}(E2)|00\rangle} \right) \end{aligned} \tag{2.32}$$

where $|nK\rangle$ is the band head of a band consisting of n quadrupole phonons with a projection K of the spin on the symmetry axis, and the ε_i are constants dependent on the nuclear moment of inertia and the exact form of the Hamiltonian. The effect of this mixing can be found as a multiplicative correction to the $B(E2)$ values found by equation 2.31 by

$$B(E2; J_i \to J_f) = B_0(E2; J_i \to J_f) \left[1 + Z_\gamma F_\gamma(J_i, J_f) + Z_{\beta\gamma} F_{\beta\gamma}(J_i, J_f) \right]^2 \tag{2.33}$$

where $B_0(E2)$ is the unmixed $B(E2)$ (as given by equation 2.31) and

$$\begin{aligned} F_\gamma(J_i, J_f) &= \frac{1}{\sqrt{24}} \left(f_\gamma(J_f) \frac{\langle J_i 2, 20|J_f 2\rangle}{\langle J_i 2, 2-2|J_f 0\rangle} - \frac{1}{2}\left(1 + (-1)^{J_i}\right) f_\gamma(J_i) \frac{\langle J_i 0, 20|J_f 0\rangle}{\langle J_i 2, 2-2|J_f 0\rangle} \right) \\ F_{\beta\gamma}(J_i, J_f) &= \frac{1}{2}\left(1 + (-1)^{J_i}\right) \frac{f_\gamma(J_i)}{\sqrt{6}} \frac{\langle J_i 0, 20|J_f 0\rangle}{\langle J_i 2, 2-2|J_f 0\rangle} \end{aligned} \tag{2.34}$$

with $f_\gamma(J) \equiv \sqrt{J(J-1)(J+1)(J+2)}$. Equations 2.33 and 2.34 result in relatively simple corrections to theoritical $B(E2)$ values as tabulated in table 2.2. These results (equations 2.33 and 2.34 and table 2.2) are specifically for γ-band to ground state band transitions. For more information on this theory, including its application to β-band to ground band transitions, see Lipas [31], Riedinger [32], and Marshalek [33]. More recent theories, such as described in Gupta [34], still explain deviations from the Alaga rules in terms of mixing

Table 2.2: Correction Factors for $B(E2)$ values based on equations 2.33 and 2.34. The correction factors listed here are only valid for γ-band to ground state band transitions. Z_γ and $Z_{\beta\gamma}$ are defined in equation 2.32. These correction factors first appeard in Lipas [31], though this work uses the sign conventions of Riedinger [32] and Marshalek [33].

J_i	J_f	$B(E2;J_i \to J_f)/B_0(E2;J_i \to J_f)$
$J-2$	J	$\left[1+(2J+1)Z_\gamma+J(J-14)Z_{\beta\gamma}\right]^2$
$J-1$	J	$\left[1+(J+2)Z_\gamma\right]^2$
J	J	$\left[1+2Z_\gamma-\frac{1}{3}J(J+1)Z_{\beta\gamma}\right]^2$
$J+1$	J	$\left[1-(J-1)Z_\gamma\right]^2$
$J+2$	J	$\left[1-(2J+1)Z_\gamma+(J+1)(J+2)Z_{\beta\gamma}\right]^2$

between the β-, γ-, and yrast-bands, but tend to rely on complex computer codes which are beyond the scope of this work.

2.5 Internal Conversion

The internal conversion decay constant is, in general, a sum of the decay constants for the conversion of electrons from the various atomic shells (K, L, M, etc.). As mentioned previously, this process competes with photon emission, which implies that the total decay constant for a transition between the initial and final nuclear states is a sum of the γ and internal conversion decay constants, $\lambda = \lambda_e + \lambda_\gamma$, where the γ-decay constant is given above for ML and EL transition. The internal conversion coefficient, α, is defined as the ratio of the decay constant for electron conversion to the decay constant for γ emission,

$$\alpha = \frac{\lambda_e}{\lambda_\gamma} \tag{2.35}$$

which is then expressed in terms of the total decay constant

$$\lambda = \lambda_\gamma(1+\alpha) \tag{2.36}$$

The internal conversion coefficients can be calculated theoretically for each atomic shell [35]. An internal conversion coefficient (ICC), combined with a measurement of the γ-decay constant, will therefore yield the total electromagnetic decay constant.

Unlike β-decay electrons, IC electrons have discrete energies determined by the energy of the transition and the binding energy of the electron that gets converted;

$$E_{e:IC} = E_{\gamma} - B_{e} \tag{2.37}$$

where $E_{e:IC}$ is the kinetic energy of the conversion electron, E_{γ} is the energy of the transition (which is the energy of the emitted γ-ray, if the transition decays by γ instead of IC), and B_e is the binding energy of the orbital electron. This inherently means that there is a minimum transition energy before IC is possible, namely B_e. However, this depends on which electron is internally converted, the more bound the electron (and thus the greater overlap between electron and nuclear wave functions) the higher the energy threshold for IC, causing discontinuities in the value α vs transition energy. Additionally, with the exception of these discontinuities, α increases as the transition energy decreases. The energy dependence of α is seen clearly in figure 2.2.

Furthermore, α (equation 2.35) is also dependent on Z such that, as Z increases, the probability of IC increases for two connected reasons. Since there are more electrons orbiting a nucleus with higher Z (number of electrons = Z), there are more candidates for internal conversion. Of greater effect, however, is the generally greater amount of charge present in the system, especially the nucleus itself, causing the strength of the interaction between the nucleus and the electrons to increase. This means that the most bound electrons are more and more tightly bound with increasing Z, causing their wave functions to be in greater overlap with the wave function of the nucleus. Figure 2.2 shows plots for four different values of Z; 25, 50, 75, and 100.

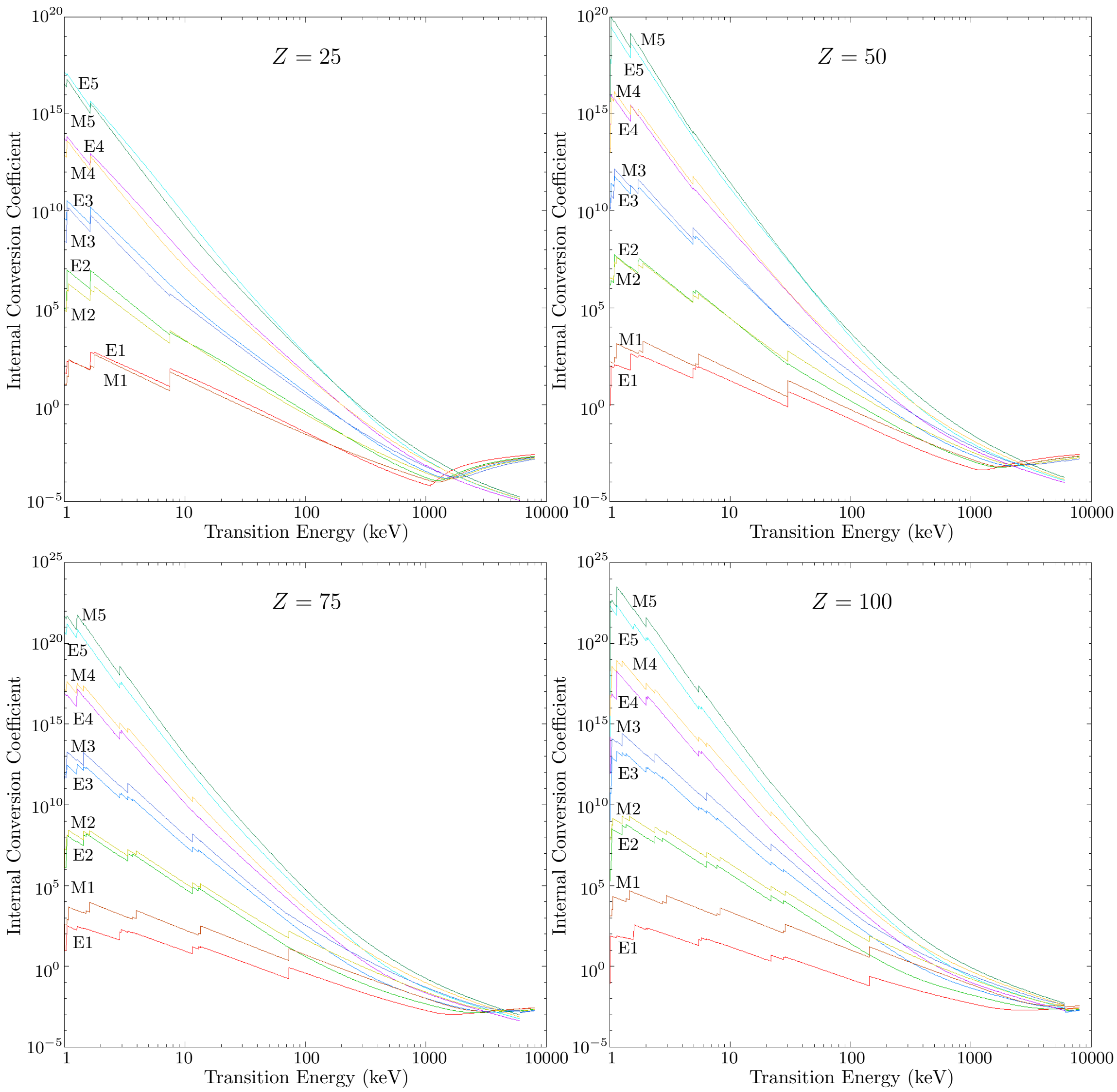

Figure 2.2: Four different plots of internal conversion coefficients as a function of Energy for different values of Z and transition multipolarities. Top left; $Z = 25$. Top right; $Z = 50$. Bottom left; $Z = 75$. Bottom right; $Z = 100$. These graphs were generated by brIcc using the brIccFO database [35].

For γ-ray transitions, as shown in equations 2.27 through 2.31, the lifetime of decay increases as the multipole order increases and magnetic transitions typically have longer lifetimes than electric. These lengthening of the γ-ray lifetimes provides more opportunities for orbital electrons to be internally converted, causing the multipolarity dependence of α shown in figure 2.2. Since γ-ray transitions are impossible for $0^{\pm} \rightarrow 0^{\pm}$ ($E0$ or $M0$) transitions, $E0$ and $M0$ transitions always transition by IC (or decay by β- or other mode), being equivalent to $\alpha = \infty$. Because nearly all data discussed in this work are from γ-decay, no $\Pi0$ transitions are observed.

Chapter 3

Nuclear Theory

3.1 Nuclear Models Describing Excited State Properties

The nucleus, like the atom, has discrete energy levels whose location and properties are governed by the rules of quantum mechanics. The locations of the excited states differ for each nucleus. The excitation energy, E_x, depends on the internal structure of each nucleus. Each excited state is characterized by quantum numbers that describe its nuclear spin (angular momentum) and parity just to name a few that are relevant to this work and are represented by J^{π}. Figure 3.1 shows a few of the excited states of the ^{12}C nucleus. The nuclear spin, J, is the sum of the individual spins of the nucleons as well as their orbital angular momentum and collective motion of the nucleus. The nuclear spin quantum number, J, is the integer or half-integer that is the measure of the total angular momentum of the energy state in units of $\hbar$ (Planck's constant h divided 2π).

Protons and neutrons are both $J=\frac{1}{2}\hbar$ particles that "prefer" to pair off (protons with protons and neutrons with neutrons) with anti-aligned spins, making the total spin become 0 for the pair. This means the ground states of all even-even nuclei have spin 0, and, for at least the lowest lying levels, the spin and parity of all other nuclei are determined by the properties of the last odd proton and/or neutron. The parity (π) of a nuclear energy level is a statement about what the nuclear structure of the state would look like if the spatial coordinates of all the nucleons were reversed. Therefore, when π = + means the reversed state would look the same as the original; π = - means the reversed state differs from the original. These quantum numbers are results of the basic symmetries of the underlying force law that governs the binding of nucleons in a nucleus. They determine how an excited state will decay into another state in the same nucleus (γ decay) or into a specific state in a different nucleus (β or α decay).

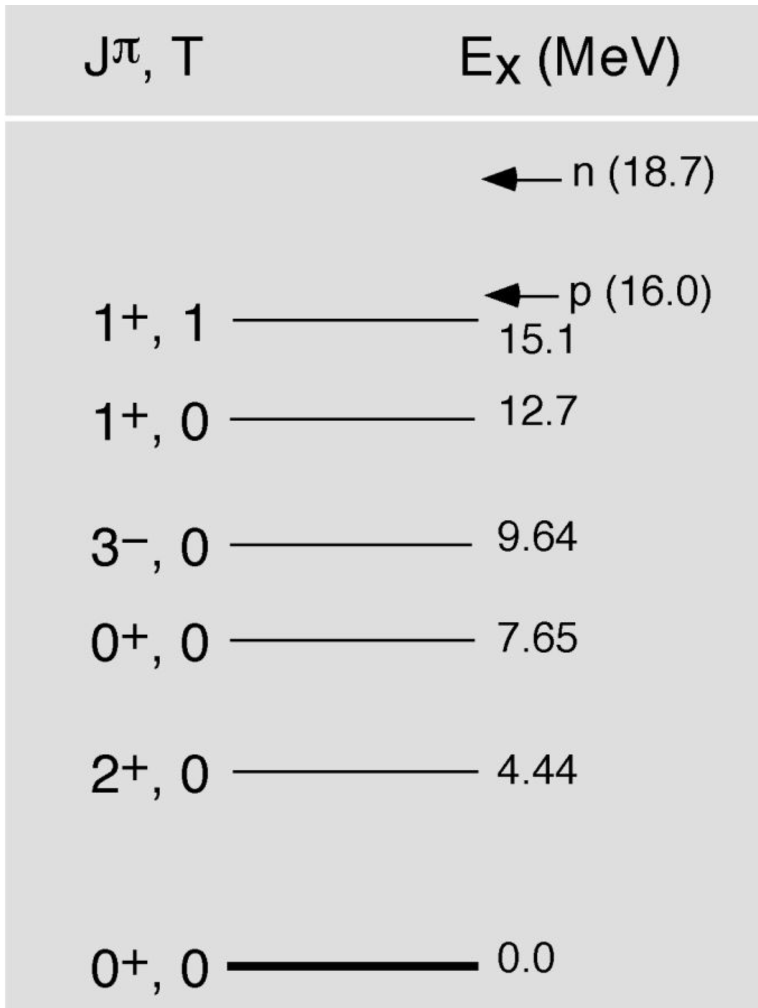

Figure 3.1: Energy level diagram of some of the excited states of the ^{12}C nucleus. The spin (angular momentum) (J), parity (P), and isospin (T) quantum numbers of the states are indicated on the left using the notation J^{π}, P and n respectively at the top of the diagram indicate the separation energies for a proton and a neutron. [36]

Analyzing the interactions among many nucleons to calculate the energy levels and their properties is a complicated mathematical task. Instead, nuclear scientists have developed several nuclear models that simplified the description the nucleus and the mathematical calculations. These simpler models still preserve the main features of nuclear structure.

Several empirical models have been formulated over the last 70 years in an attempt to describe observed nuclear-structure characteristics. There are two basic types of models used: (i) Those which describe the nucleus as individual nucleons that interact with each other, and give rise to the observed structure (microscopic models), and (ii) Those that attempt to describe nuclear structure by considering the motion of many nucleons simultaneously (collective models). The nuclear shell model is an example of the former. The shell model has been among the most successful, and widely used, microscopic models of the nucleus. The following material attempts to lay the groundwork necessary for an understanding of the primary motivation for this study, as well as describing the theoretical framework behind the experimental reaction mechanisms used to probe the specific shell-model methods.

3.2 The Shell Model

The Shell Model accounts for many features of the nuclear energy levels. According to this model, the motion of each nucleon is governed by the average attractive force of all the other nucleons. The resulting orbits form "shells," just as the orbits of electrons in atoms do. As nucleons are added to the nucleus, they drop into the lowest-energy shells permitted by the Pauli Principle, which requires that each nucleon have an unique set of quantum numbers to describe its motion. When a shell is full (that is, when the nucleons have used up all of the possible sets of quantum number assignments), a nucleus of unusual stability forms. This concept is similar to that found in an atom where a filled set of electron quantum numbers results in an atom with unusual stability–an inert gas. When all the protons or neutrons in a nucleus are in filled shells, the number of protons or neutrons is called a “magic number”. Some of the magic numbers are 2, 8, 20, 28, 50, 82, and 126. For example, ^{116}Sn has a magic number of protons (50) and ^{54}Fe has a magic number of neutrons (28). Some nuclei, for example ^{40}Ca and ^{208}Pb, have magic numbers of both protons and neutrons; these nuclei have exceptional stability and are called “doubly magic”.

Filled shells have a total angular momentum, J, equal to zero due to the anti-aligned spins as mentioned ear. The next added nucleon (a valence nucleon) determines the J of the new ground state. When nucleons (singly or in pairs) are excited out of the ground state they change the angular momentum of the nucleus as well as its parity. The shell model describes how much energy is required to move nucleons from one orbit to another and how the quantum numbers change. Promotion of a nucleon or a pair of nucleons to an unfilled shell puts the nucleus into one of the excited states shown in Fig. 3.1.

Excited nuclear states decay to more stable states, i.e., more stable nucleon orbitals. Measuring transition rates between nuclear energy levels requires specialized α, β, and γ detectors and associated electronic circuitry to precisely determine the energy and half-life of the decay (See Chapter: 4 for further details). Quantum mechanics and shell-model theory permit nuclear scientists to compute the transition probability (rate of decay) between nuclear states (as discussed in Section: 2.4). For nuclei whose structure can be described by a small number of valence nucleons outside filled shells, the Shell Model calculations agree very well with measured values of spin and parity assignments and transition probabilities.

3.3 The Collective Model

In addition to individual nucleons changing orbits to create excited states of the nucleus as described by the Shell Model, there are nuclear transitions that involve many (if not all) of the nucleons. Since these nucleons are acting together, their properties are called collective and their transitions are described by a Collective Model of nuclear structure. High-mass nuclei have low-lying excited states that are described as vibrations or rotations of non-spherical nuclei (deformed nuclei). Many of these collective properties are similar to those of a rotating or vibrating drop of liquid, and in its early development the Collective Model was called the Liquid-Drop Model. The first important application of the Liquid Drop model was in the analysis of nuclear fission, in which a massive nucleus splits into two lower-mass fragments. The Liquid Drop Model calculates an energy barrier to fission as a sum of the repulsive Coulomb forces between the protons of the nucleus and the attractive surface tension of the skin of the "liquid drop" nucleus. If the barrier is low enough the nucleus might fission spontaneously. For higher barriers, it takes a nuclear reaction to induce fission.

3.3.1 Rotational Bands

Quantum mechanically, it is impossible for a nucleus to rotate about an axis of symmetry, and thus impossible for a spherical nucleus to rotate about any axis. This is because, quantum mechanically, two indistinguishable states are in fact, the same state, thus any rotation about an axes of symmetry reproduces the original state that was rotated.

It is well known that the eigenvalues of quantum mechanical angular momentum operator L^2 are $l(l+1)\hbar^2$, where l is any non-negative integer. Thus it should be obvious that the eigenvalues of the quantum mechanical rotational Hamiltonian, $H_{rot} = \frac{L^2}{2\mathscr{L}}$ (assuming no external potential) are $l(l+1)\frac{\hbar^2}{2\mathscr{L}}$, where $\mathscr{L}$ is the moment of inertia of the system about the axis of rotation[1]. For nuclei, the quantum number l corresponds to the spin, J, of the nuclear state. Thus when a deformed nucleus rotates, the energy of each successively more rapidly rotating state is

$$E_{rot} = J(J+1)\frac{\hbar^2}{\mathscr{L}}, \tag{3.1}$$

for any non-spherical nucleus with moment of inertia $\mathscr{L}$.

In principal, any non-spherical state of a nucleus can rotate, not just the ground state. Thus, for all of the nuclei observed in this work, multiple *rotational bands* are observed.

[1]For a full derivation and definition of these operators see Shankar [37] or another introductory quantum mechanics textbook.

Since most excited states – be they single particle, vibrational, or otherwise – have rotational bands built on top of them, it is common to refer to a rotational band by the properties of its band-head. For example the rotation of the ground state is called often the yrast band[2] or ground state band, while a rotational band built on a single particle state in an odd neutron nucleus would be commonly called a $\nu J^{\pi}[Nn_z\Lambda]$ band. In such a rotational band (at least to a first order approximation), each state in the band has the same properties as the band-head; the only difference is that the higher energy states are rotating. Thus, equation 3.1 applies not to the absolute excitation, but to the excitation relative to the band-head of the rotational band.

3.3.2 Vibrational States

Most nuclei can vibrate. Such vibrations will typically follow, approximately, the even energy spacing between states characteristic of a quantum harmonic oscillator, though plenty of nuclei have been observed to exhibit varying levels of anharmonicity. Typically vibrations observed are phonons built upon the ground state of the nucleus, but some nuclei have been observed to exhibit vibrations of an excited single-particle state [38].

There are two kinds of vibrations important in this work; β-vibrations and γ-vibrations of a prolate shape. Both are quadrupole in nature and have already been addressed indirectly in section 2.4.2. These two vibrational modes are most easily understood from equation 3.2, because a β-vibration is essentially an oscillation of the β_2 deformation parameter, while a γ-vibration is the same for the γ deformation parameter.

$$r(\theta.\phi) = R_0\left(1+\beta_2\cos\gamma Y_{20}(\theta,\phi)+\frac{1}{\sqrt{2}}\beta_2\sin\gamma\left[Y_{22}(\theta,\phi)+Y_{2-2}(\theta,\phi)\right]\right) \tag{3.2}$$

To understand what is meant by a quadrupole vibration, one should recall classical electricity an magnetism. Classically, there are two kinds of closely related multipoles;

[2]Technically a yrast state is the lowest energy state of a given spin, especially in even-even nuclei. For all the nuclei studied in this work, the ground state rotational bands are all yrast states, and thus the nomenclature “yrast band” is used interchangeably in this work with “ground state rotational band.”

those defined by charge distributions and those observed as radiation sources. All nuclei have a relatively large monopole moment (Q_0), directly proportional to their charge, $+Ze$. The simplicity of the nuclear monopole moment causes it to be trivial and rarely discussed. An electric dipole requires opposing positive and negative charge in close proximity. Thus an atom may have a dipole moment (Q_1), but the nucleus, on its own, does not. Thus the leading order for an electric moment of significance in nuclear physics is the quadrupole moment, Q_2. In fact, a nucleus's deformation β_2 can be related to its quadrupole moment by

$$\beta_2 = \frac{Q_2\sqrt{5\pi}}{3ZR_0A^{1/3}} \tag{3.3}$$

where $R_0 \approx 1.2$ fm. Thus β_2 is called the quadrupole deformation parameter. Thus it is not surprising that the two most important kinds of vibrations for nuclei are quadrupole in nature, since the leading electric multipole order of any significance for nuclei is quadrupole.

Classically any accelerating charge will radiate.[3] Specifically, a harmonic vibration of a multipole distribution, as described above, will produce radiation of that same multipole order. These multipole radiations have unique angular distributions which can be used to identify them. Both of these facts remain true in the quantum world. Thus one would expect both γ and β vibrational states to emit quadrupole radiation when decaying to non-vibrational states, and that one could identify this radiation by its angular distribution. For a complete discussion of classical multipole distributions and radiations see Jackson [39]. For further detail on the nuclear applications of the quantized multipole radiations see Frauenfelder and Steffen [40] or Bohr and Mottelson [41].

[3] The loss of energy due to this radiation is one of the main reasons the Rutherford model of the atom was later replaced by the Bohr (and even later the Schrödinger-Heisenberg) quantum mechanical model.

Chapter 4

Experimental Techniques

In 1995, an experiment was performed Lawrence Berkeley National Laboratory (LBNL) by using 72 Ge detectors of Gammasphere with a 28 μCi ^{252}Cf source sandwiched between two 11.3 mg/cm^2 Ni foils. In addition, 13.7 mg/cm^2 Al foils were added on both sides. The data were sorted into 9.8×10^9 $\gamma-\gamma-\gamma$ and higher fold events and analyzed by RADWARE software [42]. The data were also sorted into different discrete time windows (from 4 ns to 500 ns). These data can be used to measure the life-time of nuclear energy state at the order of several ns to several hundred ns.

In 2000, another experiment with ^{252}Cf was carried out at the LBNL. A 62 μCi ^{252}Cf source was sandwiched between two Fe foils of thickness 10mg/cm^2 and encased in a 7.62 cm polyethylene ball. By using Ge detectors of Gammasphere, the raw data were sorted into 5.7×10^{11} $\gamma-\gamma-\gamma$ and higher fold γ events into 1.9×10^{11} $\gamma-\gamma-\gamma-\gamma$ and higher fold γ coincident events. The basic unit in the raw data is event. Each event contains the information of γ multiplicity and every coincidence γ's detector id, energy (in ADC channel number) and coincidence time. These γ coincident data were analyzed by the RADWARE software package[1].

The 2000 experiment consists of four weeks run in total, including two weeks in August and two weeks in November. For the August run, the unused detector id's are: 0, 38, 40, 45, 52, 53, 55, 58, 59, 73, 81, 88, 89, and 96, this left a total of 96 detectors. Detector 72 has a very large energy drift during the August run, but was still included in the triple coincidence data. The calibration sources are: ^{152}Eu and ^{207}Bi. For the November run, the unused detector id's are: 0, 1, 2, 4, 6, 45, 52, 53, 59, and 73. This yields 101 detectors used. The calibration sources are ^{56}Co, ^{133}Ba and ^{152}Eu. There is no significant change for the energy and efficiency calibrations between the August and November runs.

[1] For more details on the compilation of the data, see chapter 3 in [43]

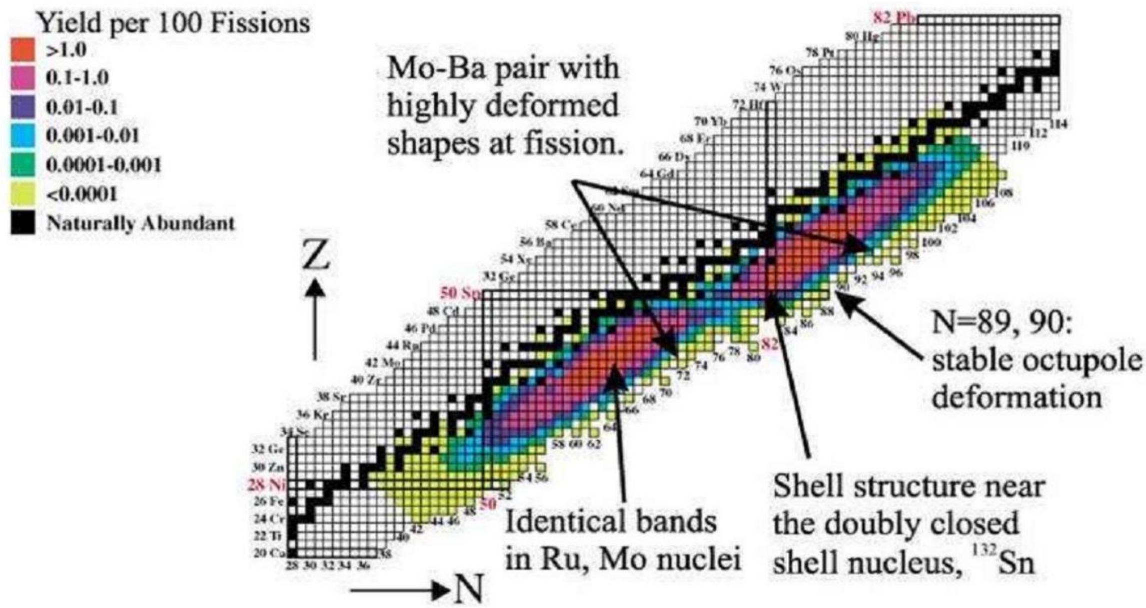

Figure 4.1: Fragment Yields of ^{252}Cf from Spontaneous Fission [44]

The ^{252}Cf is a radioactive source with 2.645 y half life where 96.91% of its decay branching is the α decay mode. The other 3.09% decay is spontaneous fission. The major part of ^{252}Cf SF is binary fission. Ternary fission contributes about less than 1%. In ^{252}Cf binary SF process, the parent nucleus splits into two daughter nuclei with roughly a 1.4:1 mass ratio between the heavy and light fragments. The distribution of the fission fragments is shown in Fig. 4.1. As mentioned in Section 2.2, afterwards, the primary fission fragments evaporate some neutrons with a total neutron distribution maximized at 3 or 4 (see chapter 6). The secondary fragments are usually populated to excited states. These excited secondary fission fragments can decay to lower states by promptly emitting γ-rays. The first and second stages of the binary fission occur very quickly in 10^{-18} to 10^{-15} seconds as seen in Fig. 4.2. In the present experiment, fission fragments and α particles were stopped by foils and neutrons as well as β-rays were partially moderated and absorbed by the foils and plastic. The γ-ray were detected in Gammasphere.

Gammasphere is a powerful spectrometer and especially good at collecting γ-rays data due to its high energy resolution, high granularity and high detection efficiency. It consists

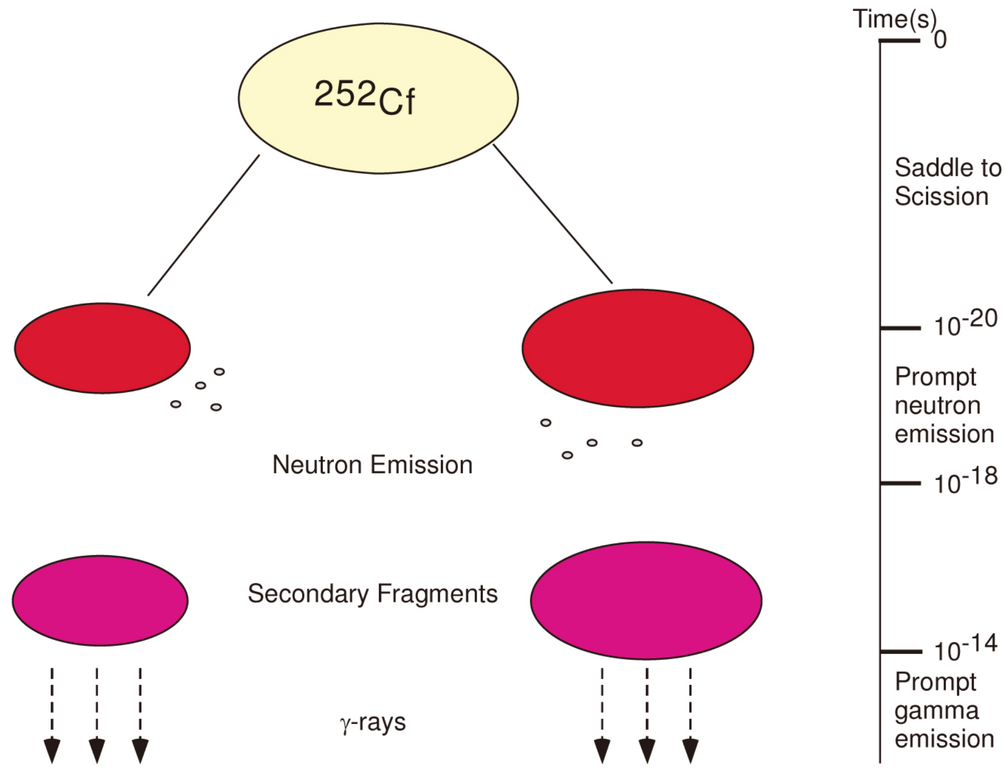

Figure 4.2: Schematics of ^{252}Cf SF processes [43]

of 110 high purity germanium (HPGe) detectors in a spherical arrangement with about 47% angular coverage. The HPGe crystals are maintained at liquid nitrogen temperature in order to reduce the signal noise.

In general, the interaction of photons with detector material atoms involves several processes: 1) Rayleigh scattering, a photon is deflected by the atom with no energy transfer, which is probable for very low energy photons and not in the γ-ray region; 2) Compton scattering, a photon is elastic scattered by an atom electron and transfers a portion of its energy to the electron to cause an ejection of the electron from the atom orbital, which is predominant for medium energy of magnitude from 0.1 to 1 MeV; 3) photoelectric effect, a photon knocks out an electron from the atom and transfer all of its energy to the electron so its own existence terminates, which is the dominant energy loss mechanism for photons of smaller than 50 keV energy but still important up to several MeV; 4) pair production, a photon with greater than 1.02 MeV energy converts into an electron and a positron. Since Compton scattering is the dominant process in the region where most radiation is emitted, an additional bismuth germanium oxide (BGO) detector is placed between the HPGe in Gammasphere to detect and reject Compton events. See Fig. 4.3.

Figure 4.3: A cross section schematic of Gammasphere [43]

4.1 Gammasphere Efficiency

The efficiency of Gammasphere is about 10% with a peak to total ratio of 0.6% at 1.33 MeV. The energy calibration is fitted to a polynomial below using standard sources during the November run because it covers the all energy region. As mentioned above, the difference between the August and November runs are quite small and neglected.

$$E = a + bN + cN^2 + dN^2 \tag{4.1}$$

where E is energy and N is the Analog-to-Digital Converter (ADC) channel number. The fitted parameters are listed in Table 4.1.

Table 4.1: Parameters of energy calibration. Note that there is a difference between the values reported here and the ones reported in [43] and [44].

a	-0.49114
b	0.33367
c	-8.3173×10^{-8}
d	5.1986×10^{-12}

The standard deviation for the energy calibration is 0.06 keV. The influence of the drifted detector 72 is quite small. In all, the error bar for the measured γ-ray energies can be treated as 0.1 keV. A simplified calibration can use 0, 0.33333 as calibration parameters and increase the error bar to 0.5 keV.

The relative efficiency for the 2000 experiment is fitted to the equation below using the relative γ-ray intensities obtained from ^{252}Cf fission fragments.

$$eff = exp[(A + Bx + Cx^2)^{-H} + (D + Fy + Gy^2)^{-H}]^{-1/H} \tag{4.2}$$

where x = Ln(E/100) with E as energy in keV, and y = Ln(E/1000) and A to H are parameters. The old fitted parameters are listed in Table. 4.2 and the new fitted parameters are listed in Table. 4.3. For the new efficiency calibration, the x-ray intensity is included which caused the difference at low energy. The new efficiency calibration is only valid from 0 to 400 keV. Figure 4.4 shows the comparison of between the old and the new efficiency parameter fits. The summation of the single coincidence (from the acquisition mode) γ-rays

Table 4.2: Old parameters of efficiency calibration [43] and [44]

A	14.1597
B	9.18559
C	-2.7907
D	6.36297
F	-0.65056
G	0.0
H	2.09765

Table 4.3: New parameters of efficiency calibration for low energy region (below 150 keV).

A	13.47327
B	3.37105
C	-3.25405
D	6.66301
F	-0.28723
G	0.0
H	3.56961

from the standard sources was used to do the efficiency calibration. This procedure is not quite accurate in principle because the efficiency of each detector varies (quite differently at low energy).

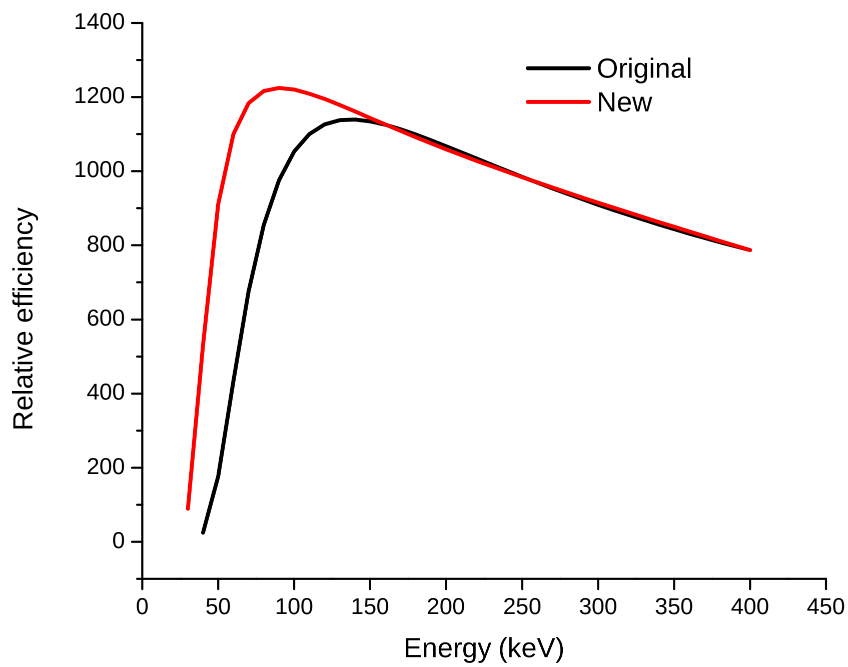

Figure 4.4: Comparison of original and new efficiency curves. The new efficiency curve is higher at low energy.

Chapter 5

Chiral vibrations and Collective Bands in ^{104,106}Mo

5.1 Introduction To Chirality

A basic property of atomic nuclei is its shape, which governs its various static as well as dynamic properties, and depends on the interaction among its constituents (protons and neutrons). Shapes ranging from spherical to tetrahedral are predicted across the nuclear landscape. The evolution of nuclear shapes as a function of angular momentum and isospin is of prime importance in nuclear structure studies [45]. There is a predominance of prolate over oblate shapes for the ground state of even-even axially deformed nuclei [46, 47]. They also display an axially symmetry at low spins. Most deformed nuclei are axially symmetric at low spins. The collective rotation is then possible only about the axis perpendicular to the symmetry axis. However, some nuclei are found to have triaxial shapes. For a triaxial nucleus, there is a possibility of rotation around any of the principal axes. There has been much of interest in understanding the role of triaxiality on the interesting phenomena like wobbling and chirality. In the present work, the focus will be on chirality.

Deviations from axial symmetry and the existence of triaxial "rigidly deformed" nuclei, first predicted in the late 50's, were assumed to be commonly possible [48, 49]. There have been a sustained experimental and theoretical efforts to establish the signature of triaxial shapes of nuclei of various mass regions. Most of these nuclei were found to exhibit vibrational modes or "softness" with respect to the triaxiality parameter γ [50, 51, 52]. The rotation of triaxial nuclei has been suggested to be manifested as chiral partner bands [53], which initiated several experimental investigations [11, 54, 55] in recent years. Various phenomena related to triaxial shapes of nuclei, like γ-vibrations [56], chiral symmetry [57], and wobbling modes [58], have been successfully described using the triaxial projected shell mode (TPSM) (see section 5.2.4).

As mentioned above, among the various phenomena exhibited by triaxial shaped nuclei is charality, and this will be discussed at great length in the present work. The word "chiral" is a word of Greek origin, "chair", which means "hand". Chirality is the study of handedness, right-handed and left-handed symmetry. Systems that can form right- and left-handed systems on reflection are chiral. For a long time, chiral structures have been of interest in complex molecules and elementary particles. However, the nucleus had long been thought to be achiral until Frauendorf and collaborators predicted the chiral symmetry breaking in rotating atomic nuclei with well-deformed triaxial shapes [7, 59]. The simplest case for chirality is an odd-odd triaxial nucleus where the total angular momentum vector is out of the three principal planes spanned by the three axes, and consequently there are significant components of angular momentum along each of the three axes. In such an odd-odd triaxial nucleus, when a high j particle aligns along the short axis (with Fermi level lying in the lower part of a valence particle high j subshell), a high j hole along the long axis z (with Fermi level lying in the upper part of a valence particle high j subshell), and the rotational angular momentum along the intermediate axis, the three angular momentum vectors may couple to each other in a right- or left-handed way generating a chiral, right-or left-handed, system in the intrinsic frame.

Well deformed triaxial deformations and configuration criteria are thus the characteristic conditions for generating chiral symmetry breaking in rotating nuclei. The spontaneous formation of the right- and left-handed system in a nucleus would give rise to nearly degenerate $\Delta I = 1$ doublet bands in the laboratory frame. These chiral doublet bands exhibit a series of fingerprints [60, 9]: (a) Near energy degeneracy observed for partner levels, levels of the same spin/parity; (b) Similar structure, consequently similar electromagnetic properties such as B(E2)/B(M1) ratios for partner levels; (c) Constant with spin and equal values of the energy staggering parameter $S(I) = [E(I)-E(I-1)]/2I$ for the two doublet bands, being due to the reduction of Coriolis interaction in the chiral doubling. In contrast to the ideal case generating chiral rotation, the still noticeable energy differences between the partner levels of the chiral doublet bands point to a dynamical character of chirality.

In contrast to the case of odd-odd nuclei, for the even-even nuclei, the observation of chiral symmetry breaking seems to further exemplify the general geometric character of chiral symmetry breaking [59], because the non-planar geometry of rotation cannot be directly related to the alignment of high j particles and high j holes with different principal axes [13].

Chiral nuclei have been suggested experimentally in $A \sim 80$ [61, 62], $A \sim 100$ [9, 10, 11, 13, 15, 63, 64, 65, 66, 67, 68, 69, 70], $A \sim 130$ [54, 71, 72, 73], $A \sim 190$ [74, 75] mass regions. In recent years, the soft triaxial ^{106}Mo was suggested to have chiral doublet bands [2], where chirality is generated by neutron $h_{11/2}$ particle and mixed $d_{5/2}$, $g_{7/2}$ hole coupled to the short and long axis, respectively. The same chiral configurations were identified in ^{108,110,112}Ru [15].

Because of these discoveries, we were prompted to investigate the presence of chiral bands in ^{104}Mo given its similarity in band structure with ^{106}Mo. For instance, both nuclei have one-and two-phonon gamma vibrational bands which indicate the softness with respect to triaxial deformations [76, 77]. In these soft nuclei, nuclear shapes may be driven to stable triaxiality due to the excitation of quasi-particles [59, 78]. In the present work, we find the candidates for chiral doublet bands in ^{104}Mo with more degenerate energies for states of the same spin ($\sim$60 keV) than in ^{106}Mo ($\sim$100 to 140 keV) [2]. Close agreement of the levels of the same spin states in the two bands are a fingerprint for chiral bands.

5.2 Discussion and Results

5.2.1 ^{104}Mo Spectra

In ^{104}Mo, the ground state band (1) and γ-vibrational band (2) have been confirmed. The two phonon γ vibrational band (3) levels have been extended and reassigned. In Ref. [79], the 8^+ to 6^+ transition of the two phonon γ vibrational band was reported as

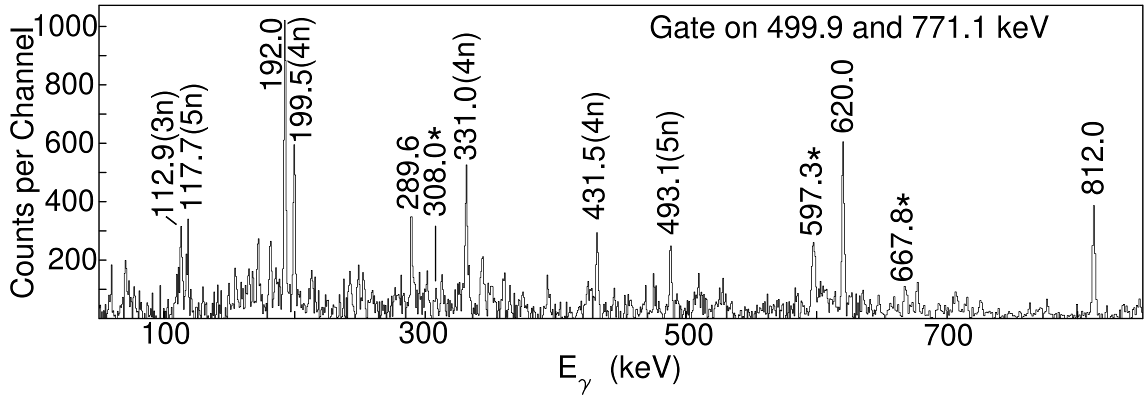

Figure 5.1: Partial γ-ray coincidence spectra by gating on 499.9 and 771.1 keV transitions in ^{104}Mo. New transitions are labeled with an asterisk. Fission partner transitions are labeled with neutron evaporation numbers. Here 3n, 4n, 5n denote ^{145}Ba, ^{144}Ba and ^{143}Ba, respectively.

601.6 keV. This transition is replaced by a 597.3 keV transition in the current work. Fig. 5.1 shows γ-ray coincidence spectrum by gating on the 499.9 and 771.1 keV transitions. In this spectrum, the 597.3 and 667.8 keV are E2 new transitions and the 308.0 keV M1 is new transition in band (3) and can be seen. The previous reported 601.6 keV in Ref. [79] lies on the 600 keV neutron platform on the right of the 597.3 keV peak in Fig. 5.1.

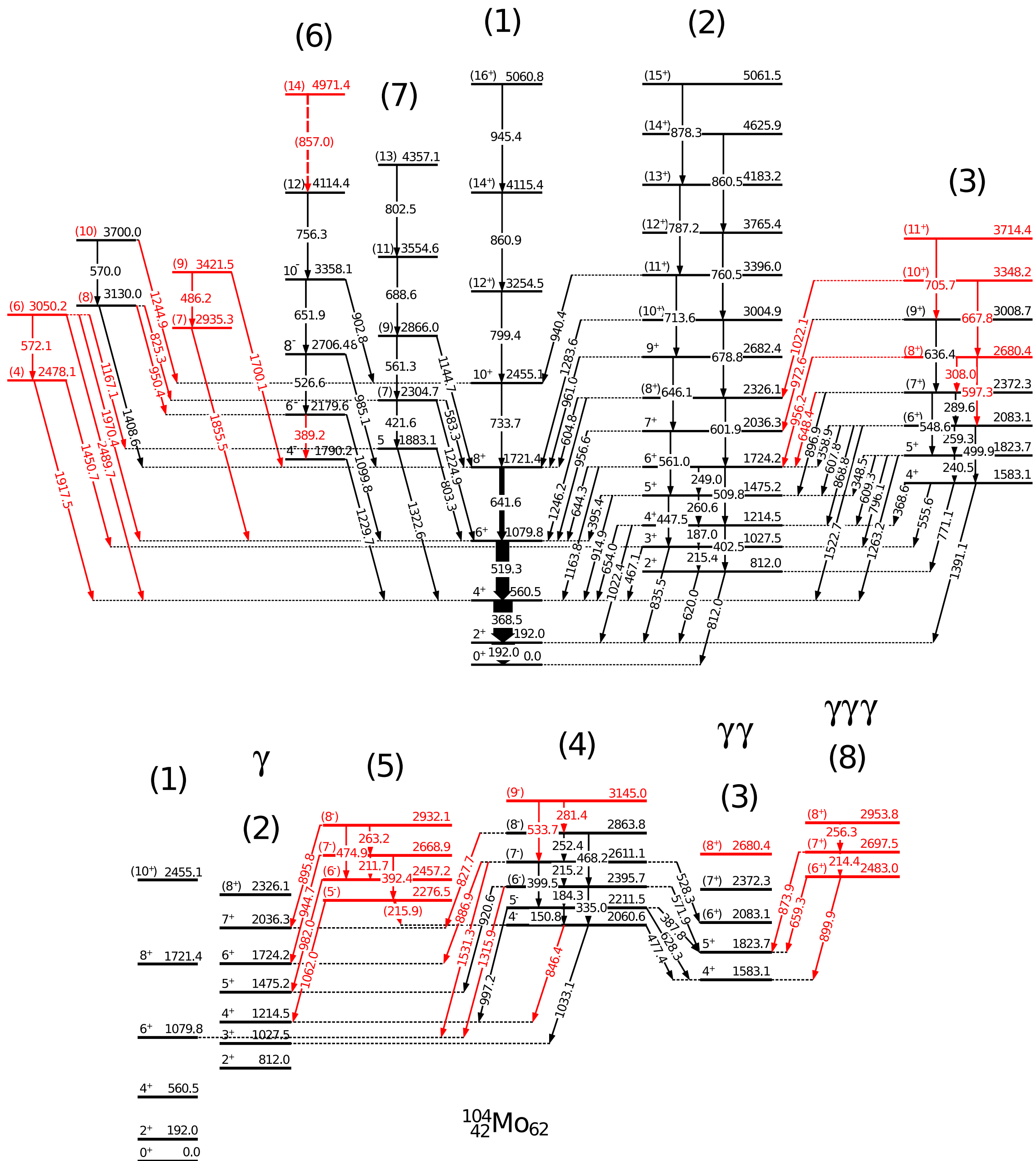

Figure 5.2: Partial level scheme of ^{104}Mo obtained in the current work. New energies and transitions are labeled in red.

Table 5.1: Level energies and γ-ray energies of ^{104}Mo obtained in the current work. Here E_i, E_f, E_γ, I_γ and B correspond to initial level energy, final level energy, γ-ray energy, γ-ray intensity and band number, respectively. The γ-ray intensities are normalized to the 192.0 keV one. New levels and transitions are labeled with an asterisk.

Initial Level					Final Level		
E_i(keV)	J^π	B	E_γ(keV)	I_γ	E_f(keV)	J^π	B
0.0	0+	1					
192.0	2+	1	192.0	100(5)	0.0	0+	1
560.5	4+	1	368.5	83(4)	192.0	2+	1
812.0	2+	2	620.0	6.2(3)	192.0	2+	1
			812.0	5.1(3)	0.0	0+	1
1027.5	3+	2	215.4	<0.4	812.0	2+	2
			467.1	1.0(1)	560.5	4+	1
			835.5	9.8(5)	192.0	2+	1
1079.8	6+	1	519.3	53(3)	560.5	4+	1
1214.5	4+	2	402.5	1.0(1)	812.0	2+	2
			187.0	<0.18	1027.5	3+	2
			654.0	6.2(3)	560.5	4+	1
			1022.4	3.8(2)	192.0	2+	1
1475.2	5+	2	260.6	0.27(6)	1214.5	4+	2
			395.4	0.18(6)	1079.8	6+	1
			447.5	2.7(1)	1027.5	3+	2
			914.9	6.4(3)	560.5	4+	1
1583.1	4+	3	368.6	2.0(2)	1214.5	4+	2
			555.6	2.7(2)	1027.5	3+	2
			771.1	6.1(3)	821.0	2+	2
			1391.0	0.24(3)	192.0	2+	1

Table 5.1 – continued.

Initial Level					Final Level		
E_i(keV)	J^{π}	B	E_{γ}(keV)	I_{γ}	E_f(keV)	J^{π}	B
1721.4	8+	1	641.6	2.2(1)	1079.8	6+	1
1724.2	6+	2	249.0	0.4(1)	1475.2	5+	2
			509.8	2.9(2)	1214.5	4+	2
			644.3	1.8(1)	1079.8	6+	1
			1163.8	2.2(1)	560.5	4+	1
1790.2	4-	6	1229.7	0.77(5)	560.5	4+	1
1823.7	5+	3	240.5	3.9(4)	1583.1	4+	3
			348.5	0.58(6)	1475.2	5+	2
			609.3	1.4(1)	1214.5	4+	2
			796.1	2.9(2)	1027.5	3+	2
			1263.2	0.40(3)	560.5	4+	1
1883.1	5	7	803.3	1.2(1)	1079.8	6+	1
			1322.6	1.7(1)	560.5	4+	1
2036.3	7+	2	561.0	4.0(3)	1475.2	5+	2
			956.6	2.1(1)	1079.8	6+	1
2060.6	4-	4	477.4	2.2(2)	1583.1	4+	3
			846.4*	0.52(8)	1214.5	4+	2
			1033.1	0.05(1)	1027.5	3+	2
2083.1	(6+)	3	259.3	1.1(1)	1823.7	5+	3
			358.9	0.6(1)	1724.2	6+	2
			499.9	1.5(1)	1583.1	4+	3
			607.8	0.63(4)	1475.2	5+	2
			868.8	0.81(6)	1214.5	4+	2
			1522.7	0.38(2)	560.5	4+	1

Table 5.1 – continued.

Initial Level					Final Level		
E_i(keV)	J^π	B	E_γ(keV)	I_γ	E_f(keV)	J^π	B
2179.6	6-	6	389.2*	0.021(2)	1790.2	4-	6
			1099.8	1.6(1)	1079.8	6+	1
2211.5	5-	4	150.8	1.6(2)	2060.6	4-	4
			387.8	1.7(2)	1823.7	5+	3
			628.3	1.3(1)	1583.1	4+	3
			997.2	0.34(3)	1214.5	4+	2
2276.5*	(5-)	5	(215.9)*		2060.6	4-	4
			1062.0*	0.11(2)	1214.5	4+	2
2304.7	(7)	7	421.6	1.4(1)	1883.1	5	7
			583.3	2.2(1)	1721.4	8+	1
			1224.9	2.8(1)	1079.8	6+	1
2326.1	(8+)	2	601.9	3.3(3)	1724.2	6+	2
			604.8	0.7(1)	1721.4	8+	1
			1246.2	0.93(5)	1079.8	6+	1
2372.3	(7+)	3	289.6	1.3(3)	2083.1	(6+)	3
			548.6	1.4(2)	1823.7	5+	3
			648.4*	0.41(9)	1724.2	6+	2
			896.9	0.20(4)	1475.2	5+	2
2395.7	(6-)	4	184.3	0.75(4)	2211.5	5-	4
			335.0	0.30(2)	2060.6	4-	4
			571.9	0.8(2)	1823.7	5+	3
			920.6	0.25(2)	1475.2	5+	2
			1315.9*	0.24(1)	1079.8	6+	1
2455.1	10+	1	733.7	7.8(4)	1721.4	8+	1

Table 5.1 – continued.

Initial Level					Final Level		
E_i(keV)	J^π	B	E_γ(keV)	I_γ	E_f(keV)	J^π	B
2457.2*	(6-)	5	982.0*	0.22(2)	1475.2	5+	2
2478.1*	(4)		1450.7*	0.22(1)	1027.5	3+	2
			1917.5*	0.29(2)	560.5	4+	1
2483.0*	(6+)	8	659.3*	0.29(4)	1823.7	5+	3
			899.9*	0.71(7)	1583.1	4+	3
2611.1	(7-)	4	215.2	0.38(2)	2395.7	(6-)	4
			399.5	0.18(1)	2211.5	5-	4
			528.3	0.35(9)	2083.1	(6+)	3
			886.9*	0.29(4)	1724.2	6+	2
			1531.3*	0.17(1)	1079.8	6+	1
2668.9*	(7-)	5	211.7*	0.026(2)	2457.2	(6-)	5
			392.4*	0.05(1)	2276.5	(5-)	5
			944.7*	0.10(2)	1724.2	6+	2
2680.4*	(8+)	3	308.0*	0.4(1)	2372.3	(7+)	3
			597.3*	1.4(3)	2083.1	(6+)	3
			956.2*	0.27(4)	1724.2	6+	2
2682.4	(9+)	2	646.1	2.6(2)	2036.3	7+	2
			961.0	0.71(4)	1721.4	8+	1
2697.5*	(7+)	8	214.4*	0.8(1)	2483.0	(6+)	8
			873.9*	0.5(1)	1823.7	5+	3
2706.4	8-	6	526.6	0.32(3)	2179.6	6-	6
			985.1	1.1(1)	1721.4	8+	1
2863.8	(8-)	4	252.4	0.15(2)	2611.1	(7-)	4
			468.2	0.18(1)	2395.7	(6-)	4

Table 5.1 – continued.

Initial Level					Final Level		
E_i(keV)	J^π	B	E_γ(keV)	I_γ	E_f(keV)	J^π	B
			827.7	0.06(1)	2036.3	7+	2
2866.0	(9)	7	561.3	3.7(2)	2304.7	(7)	7
			1144.7	0.61(3)	1721.4	8+	1
2932.1*	(8-)	5	263.2*	0.014(2)	2668.9	(7-)	5
			474.9*	0.028(2)	2457.2	(6-)	5
			895.8*	0.11(1)	2036.3	7+	2
2935.3*	(7)		1855.5*	0.39(3)	1079.8	6+	1
2953.8*	(8+)	8	256.3*	0.3(1)	2697.5	(7+)	8
3004.9	(10+)	2	678.8	1.8(2)	2326.1	(8+)	2
			1283.6	0.26(2)	1721.4	8+	1
3008.7	(9+)	3	636.4	0.7(3)	2372.3	(7+)	3
			972.6*	0.15(2)	2036.3	7+	2
3050.2*	(6)		572.1*	0.18(2)	2478.1	(4)	
			1167.1*	0.40(3)	1883.1	5	7
			1970.4*	0.07(2)	1079.8	6+	1
			2489.7*	0.6(1)	560.5	4+	1
3130.0	(8)		825.3*	0.22(2)	2304.7	(7)	7
			950.4*	0.04(1)	2179.6	6-	6
			1408.6	0.44(2)	1721.4	8+	1
3145.0*	(9-)	4	281.4*	0.10(1)	2863.8	(8-)	4
			533.7*	0.09(1)	2611.1	(7-)	4
3254.5	(12+)	1	799.4	2.2(1)	2455.1	10+	1
3348.2*	(10+)	3	667.8*	0.6(3)	2680.4	(8+)	3
			1022.1*	0.11(2)	2326.1	(8+)	2

Table 5.1 – continued.

Initial Level					Final Level		
E_i(keV)	J^π	B	E_γ(keV)	I_γ	E_f(keV)	J^π	B
3358.1	10-	6	651.9	0.32(5)	2706.4	8-	6
			902.8	0.39(2)	2455.1	10+	1
3396.0	(11+)	2	713.6	1.4(1)	2682.4	(9+)	2
			940.4	0.20(2)	2455.1	10+	1
3421.5*	(9)		486.2*	0.07(1)	2935.3	(7)	
			1700.1*	0.09(1)	1721.4	8+	1
3554.6	(11)	7	688.6	1.3(1)	2866.0	(9)	7
3700.0	(10)		570.0	0.25(6)	3130.0	(8)	
			1244.9*	0.05(1)	2455.1	10+	1
3714.4*	(11+)	3	705.7*	0.3(1)	3008.7	(9+)	3
3765.4	(12+)	2	760.5	0.75(9)	3004.9	(10+)	2
4114.4	(12)	6	756.3	0.14(3)	3358.1	10-	6
4115.4	(14+)	1	860.9	0.58(6)	3254.5	(12+)	1
4183.2	(13+)	2	787.2	0.28(3)	3396.0	(11+)	2
4357.1	(13)	7	802.5	0.16(4)	3554.6	(11)	7
4625.9	(14+)	2	860.5	0.15(3)	3765.4	(12+)	2
4971.4*	(14)	6	(857.0)*		4114.4	(12)	6
5060.8	(16+)	1	945.4	0.08(1)	4115.4	(14+)	1
5061.5	(16+)	2	878.3	0.04(1)	4183.2	(13+)	2

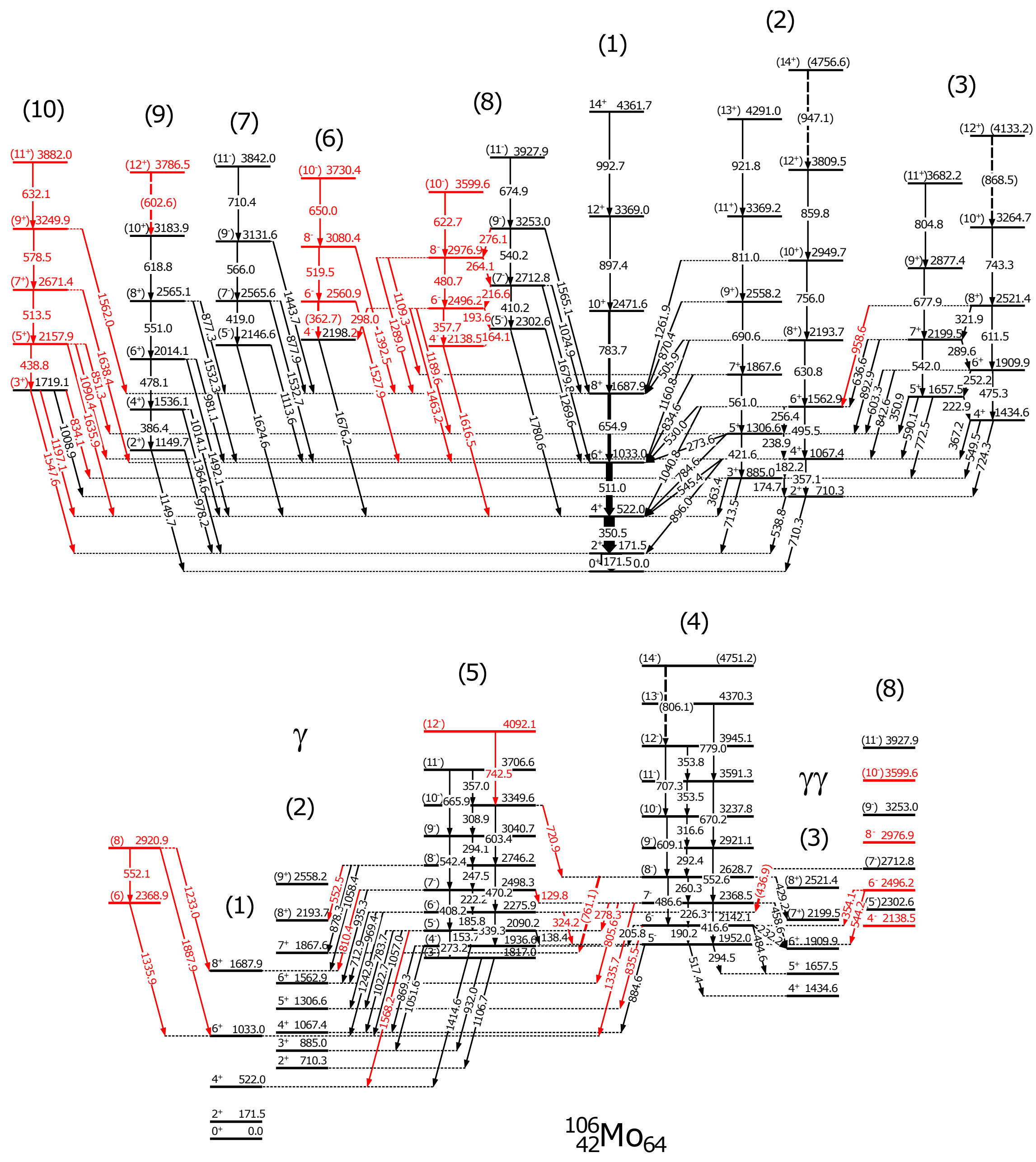

Figure 5.3: Partial level scheme of ^{106}Mo obtained in the current work. New energies levels and transitions are labeled in red. Note the 1936.6 keV level is placed in band (5) but assigned to band (4) from the current calculation.

Table 5.2: Level energies and γ-ray energies of ^{106}Mo obtained in the current work. Here E_i, E_f, E_γ, I_γ and B correspond to initial level energy, final level energy, γ-ray energy, γ-ray intensity and band number, respectively. The γ-ray intensities are normalized to the 171.5 keV one. New levels and transitions are labeled with an asterisk.

Initial Level					Final Level		
E_i(keV)	J^π	B	E_γ(keV)	I_γ	E_f(keV)	J^π	B
0.0	0+	1					
171.5	2+	1	171.5	100(5)	0.0	0+	1
522.0	4+	1	350.5	73(4)	171.5	2+	1
710.3	2+	2	538.8	8.8(4)	171.5	2+	1
			710.3	10.3(5)	0.0	0+	1
885.0	3+	2	174.7	0.24(5)	710.3	2+	2
			363.4	0.88(9)	522.0	4+	1
			713.5	21(1)	710.3	2+	2
1033.0	6+	1	511.0	46(2)	522.0	4+	1
1067.4	4+	2	182.2	0.29(6)	885.0	3+	2
			357.1	3.4(2)	710.3	2+	2
			545.4	6.5(4)	522.0	4+	1
			896.0	7.4(4)	171.5	2+	1
1149.7	(2+)	9	978.2	1.3(1)	171.5	2+	1
			1149.7	0.84(6)	0.0	0+	1
1306.6	5+	2	238.9	0.50(6)	1067.4	4+	2
			273.6	0.18(1)	1033.0	6+	1
			421.6	7.5(4)	885.0	3+	2
			784.6	9.3(5)	522.0	4+	1
1434.6	4+	3	367.2	0.44(9)	1067.4	4+	2
			549.5	3.8(2)	885.0	3+	2

Table 5.2 – continued.

Initial Level					Final Level		
E_i(keV)	J^π	B	E_γ(keV)	I_γ	E_f(keV)	J^π	B
			724.3	9.8(5)	710.3	2+	2
1536.1	(4+)	9	386.4	0.90(5)	1149.7	(2+)	9
			1014.1	1.8(1)	522.0	4+	1
			1364.6	1.8(1)	171.5	2+	1
1562.9	6+	2	256.4	0.61(6)	1306.6	5+	2
			495.5	7.5(4)	1067.4	4+	2
			530.0	3.0(2)	1033.0	6+	1
			1040.8	2.5(2)	522.0	4+	1
1657.5	5+	3	222.9	2.0(1)	1434.6	4+	3
			350.9	1.6(2)	1306.6	5+	2
			590.1	3.4(2)	1067.4	4+	2
			772.5	6.7(3)	885.0	3+	2
1687.9	8+	1	654.9	17(1)	1033.0	6+	1
1719.1	(3+)	10	834.1*	0.08(3)	885.0	3+	2
			1008.9	0.49(6)	710.3	2+	2
			1197.1*	0.11(2)	522.0	4+	1
			1547.6*	0.26(2)	171.5	2+	1
1817.0	(3-)	5	932.0	0.53(3)	885	3+	2
			1106.7	1.7(1)	710.3	2+	2
1867.6	7+	2	561.0	5.4(3)	1306.6	5+	2
			834.6	3.1(3)	1033.0	6+	1
1909.9	6+	3	252.2	1.3(1)	1657.5	5+	3
			475.3	2.4(2)	1434.6	4+	3
			603.3	2.3(3)	1306.6	5+	2

Table 5.2 – continued.

Initial Level					Final Level		
E_i(keV)	J^π	B	E_γ(keV)	I_γ	E_f(keV)	J^π	B
			842.6	2.6(2)	1067.4	4+	2
1936.6	(4-)	5	869.3	0.72(5)	1067.4	4+	2
			1051.6	1.1(1)	885.0	3+	2
			1414.6	0.12(3)	522.0	4+	1
1952.0	5-	4	294.5	0.19(3)	1657.5	5+	3
			517.4	5.7(3)	1434.6	4+	3
			884.6	<0.28	1067.4	4+	2
2014.1	(6+)	9	478.1	3.0(2)	1536.1	(4+)	9
			981.1	0.70(5)	1033.0	6+	1
			1492.1	1.3(1)	522.0	4+	1
2090.2	(5-)	5	138.4	0.10(1)	1952.0	5-	4
			153.7	0.26(3)	1936.6	(4-)	5
			273.2	0.38(4)	1817.0	(3-)	5
			783.7	1.5(1)	1306.6	5+	2
			1022.7	2.2(1)	1067.4	4+	2
			1057.0	0.22(2)	1033.0	6+	1
			1568.2*	0.13(2)	522.0	4+	1
2138.5*	4-	8	1616.5*	1.6(1)	522.0	4+	1
2142.1	6-	4	190.2	2.3(1)	1952.0	5-	4
			205.8	0.22(1)	1936.6	(4-)	5
			232.2	0.91(7)	1909.9	6+	3
			484.6	5.3(3)	1657.5	5+	3
			835.5*	0.6(1)	1306.6	5+	2
2146.6	(5-)	7	1113.6	0.87(7)	1033.0	6+	1

Table 5.2 – continued.

Initial Level					Final Level		
E_i(keV)	J^π	B	E_γ(keV)	I_γ	E_f(keV)	J^π	B
			1624.6	0.88(6)	522.0	4+	1
2157.9*	(5+)	10	438.8*	0.27(5)	1719.1	(3+)	10
			851.3*	0.13(3)	1306.6	5+	2
			1090.4*	0.61(6)	1067.4	4+	2
			1635.9*	0.12(2)	522.0	4+	1
2193.7	(8+)	2	505.9	1.1(1)	1687.9	8+	1
			630.8	5.9(3)	1562.9	6+	2
			1160.8	0.81(6)	1033.0	6+	1
2198.2	4-	6	1676.2	0.8(2)	522.0	4+	1
2199.5	7+	3	289.6	1.3(1)	1909.9	6+	3
			542.0	1.8(1)	1657.5	5+	3
			636.6	0.81(6)	1562.9	6+	2
			892.9	0.79(7)	1306.6	5+	2
2275.9	(6-)	5	185.8	0.29(2)	2090.2	(5-)	5
			324.2*	0.10(2)	1952.0	5-	4
			339.3	0.76(5)	1936.6	(4-)	5
			712.9	2.0(2)	1562.9	6+	2
			969.4	1.4(1)	1306.6	5+	2
			1242.9	0.50(4)	1033.0	6+	1
2302.6	(5-)	8	164.1*	0.05(1)	2138.5	4-	8
			1269.6	0.30(2)	1033.0	6+	1
			1780.6	1.9(1)	522.0	4+	1
2368.5	7-	4	226.3	2.2(1)	2142.1	6-	4
			278.3*	0.13(1)	2090.2	(5-)	5

Table 5.2 – continued.

Initial Level					Final Level		
E_i(keV)	J^π	B	E_γ(keV)	I_γ	E_f(keV)	J^π	B
			416.6	2.9(2)	1952.0	5-	4
			458.6	2.3(2)	1909.9	6+	3
			805.6*	0.67(6)	1562.9	6+	2
			1335.7*	0.32(4)	1033.0	6+	1
2368.9	(6)		1335.9*	0.29(5)	1033.0	6+	1
2471.6	10+	1	783.7	3.0(2)	1687.9	8+	1
2496.2*	6-	8	193.6*	0.36(2)	2302.6	(5-)	8
			298.0*	0.13(1)	2198.2	4-	6
			354.1*	0.12(2)	2142.1	6-	4
			357.7*	0.61(4)	2138.5	4-	8
			544.2*	0.08(1)	1952.0	5-	4
			1189.6*	0.24(2)	1306.6	5+	2
			1463.2*	0.08(1)	1033.0	6+	1
2498.3	(7-)	5	129.8*	0.15(2)	2368.5	7-	4
			222.2	0.67(5)	2275.9	(6-)	5
			408.2	2.1(1)	2090.2	(5-)	5
			810.4*	0.11(2)	1687.9	8+	1
			935.3	0.84(7)	1562.9	6+	2
2521.4	(8+)	3	321.9	1.2(1)	2199.5	7+	3
			611.5	2.3(2)	1909.9	6+	3
			958.6*	0.31(4)	1562.9	6+	2
2558.2	(9+)	2	690.6	2.4(3)	1867.6	7+	2
			870.4	0.29(3)	1687.9	8+	1
2560.9*	6-	6	(362.7)*		2198.2	4-	6

Table 5.2 – continued.

Initial Level					Final Level		
E_i(keV)	J^π	B	E_γ(keV)	I_γ	E_f(keV)	J^π	B
			1527.9*	0.93(6)	1033.0	6+	1
2565.1	(8+)	9	551.0	2.7(2)	2014.1	(6+)	9
			877.3	0.36(3)	1687.9	8+	1
			1532.3	0.64(8)	1033.0	6+	1
2565.6	(7-)	7	419.0	0.43(4)	2146.6	(5-)	7
			877.9	0.25(2)	1687.9	8+	1
			1532.7	0.75(7)	1033.0	6+	1
2628.7	(8-)	4	260.3	1.5(1)	2368.5	7-	4
			429.2	0.66(6)	2199.5	7+	3
			486.6	4.2(2)	2142.1	6-	4
			(761.1)*		1867.6	7+	2
2671.4*	(7+)	10	513.5*	0.7(1)	2157.9	(5+)	10
			1638.4*	0.26(5)	1033.0	6+	1
2712.8	(7-)	8	216.6*	0.017(2)	2496.2	6-	8
			410.2	0.66(4)	2302.6	(5-)	8
			(436.9)*		2275.9	(6-)	5
			1024.9	<0.17	1687.9	8+	1
			1679.8	1.3(1)	1033.0	6+	1
2746.2	(8-)	5	247.5	0.36(4)	2498.3	(7-)	5
			470.2	2.3(2)	2275.9	(6-)	5
			552.5*	0.12(6)	2193.7	(8+)	2
			878.3	0.16(3)	1867.6	7+	2
			1058.4	0.27(2)	1687.9	8+	1
2877.4	(9+)	3	677.9	2.2(1)	2199.5	7+	3

Table 5.2 – continued.

Initial Level					Final Level		
E_i(keV)	J^π	B	E_γ(keV)	I_γ	E_f(keV)	J^π	B
2920.9*	(8)		552.1*	0.12(5)	2368.9	(6)	
			1233.0*	0.29(2)	1687.9	8+	1
			1887.9*	0.18(2)	1033.0	6+	1
2921.1	(9-)	4	292.4	0.55(3)	2628.7	(8-)	4
			552.6	3.2(2)	2368.5	7-	4
2949.7	(10+)	2	756.0	2.7(3)	2193.7	(8+)	2
			1261.9	<0.08	1687.9	8+	1
2976.9*	8-	8	264.1*	0.17(1)	2712.8	(7-)	8
			480.7*	0.87(5)	2496.2	6-	8
			1109.3*	0.07(1)	1867.6	7+	2
			1289.0*	0.05(1)	1687.9	8+	1
3040.7	(9-)	5	294.1	0.22(3)	2746.2	(8-)	5
			542.4	1.9(1)	2498.3	(7-)	5
3080.4*	8-	6	519.5*	0.47(3)	2560.9	6-	6
			1392.5*	0.18(4)	1687.9	8+	1
3131.6	(9-)	7	566.0	0.77(8)	2565.6	(7-)	7
			1443.7	0.80(6)	1687.9	8+	1
3183.9	(10+)	9	618.8	1.8(2)	2565.1	(8+)	9
3237.8	(10-)	4	316.6	0.17(1)	2921.1	(9-)	4
			609.1	1.5(2)	2628.7	(8-)	4
3249.9*	(9+)	10	578.5*	0.6(1)	2671.4	(7+)	10
			1562*	<0.03	1687.9	8+	1
3253.0	(9-)	8	276.1*	0.08(1)	2976.9	8-	8
			540.2	0.73(4)	2712.8	(7-)	8

Table 5.2 – continued.

Initial Level					Final Level		
E_i(keV)	J^π	B	E_γ(keV)	I_γ	E_f(keV)	J^π	B
			1565.1	0.22(5)	1687.9	8+	1
3264.7	(10+)	3	743.3	1.0(2)	2521.4	(8+)	3
3349.6	(10-)	5	308.9	0.23(2)	3040.7	(9-)	5
			603.4	1.5(1)	2746.2	(8-)	5
			720.9*	0.15(2)	2628.7	(8-)	4
3369.0	12+	1	897.4	0.6(1)	2471.6	10+	1
3369.2	(11+)	2	811.0	0.38(6)	2558.2	(9+)	2
3591.3	(11-)	4	353.5	0.10(2)	3237.8	(10-)	4
			670.2	0.79(6)	2921.1	(9-)	4
3599.6*	(10-)	8	622.7*	0.34(9)	2976.9	(10-)	8
3682.2	(11+)	3	804.8	0.20(3)	2877.4	(9+)	3
3706.6	(11-)	5	357.0	0.17(2)	3349.6	(10-)	5
			665.9	0.79(7)	3040.7	(9-)	5
3730.4*	(10-)	6	650.0*	<0.1	3080.4	8-	6
(3786.5)*	(12+)	9	(602.6)*		3183.9	(10+)	9
3809.5	(12+)	2	859.8	0.35(5)	2949.7	(10+)	2
3842.0	(11-)	7	710.4	<0.7	3131.6	(9-)	7
3882.0*	(11+)	10	632.1*	0.09(3)	3249.9	(9+)	10
3927.9	(11-)	8	674.9	0.28(4)	3253.0	(9-)	8
3945.1	(12-)	4	353.8	0.027(6)	3591.3	(11-)	4
			707.3	0.65(8)	3237.8	(10-)	4
4092.1*	(12-)	5	742.5*	0.29(4)	3349.6	(10-)	5
(4133.2)	(12+)	3	(868.5)		3264.7	(10+)	3
4291.0	(13+)	2	921.8	0.03(1)	3369.2	(11+)	2

Table 5.2 – continued.

Initial Level					Final Level		
E_i(keV)	J^π	B	E_γ(keV)	I_γ	E_f(keV)	J^π	B
4361.7	14+	1	992.7	0.10(2)	3369.0	12+	1
4370.3	(13-)	4	779.0	0.12(2)	3591.3	(11-)	4
(4751.2)	(14-)	4	(806.1)		3945.1	(12-)	4
(4756.6)	(14+)	2	(947.1)		3809.5	(12+)	2

Fig. 5.4 depicts the high energy part of spectra by gating on: (a) 192.0 keV ground state band transition and 914.9 keV depopulating the 1475 keV 5^+ level of band (2), and (b) 835.5 keV transition depopulating the 3^+ level of band (2) and 447.5 keV transition in band (2). Transitions populating the 1475 keV 5^+ level of band (2) should be observed in both of these two parts. In those two spectra, the 827.7 and 920.6 keV transitions decaying from band (4) to band (2), the 895.8 and 982.0 keV transitions decaying from band (5) to band (2), and 896.9 and 972.6 keV transitions decaying from band (3) to band (2) can be seen. In our data, there are global 896, 1014, 1039 keV contamination transitions in almost any coincidence spectra. The 895.8 and 896.9 keV transitions overlap in the spectra in Fig. 5.4. However, those two transitions are populating different states – 7+ and 5+ in band 2, respectively. The 895.8 keV transition can be identified from the 561-447 keV gate (not shown in the paper) with such 1 keV energy difference. The 1195.4 keV peak is a transition depopulating the 2671 keV level, as reported in previous β-decay work [80]. The 1180.7 keV transition is a new one decaying from the 2656 keV level to the 1475.2 keV level. The 2656 keV level was reported previously in Ref. [79, 80]. Note the 1180,1195 keV transitions and 2656, 2671 keV levels are not placed in the ^{104}Mo level scheme in Fig. 5.2. This is because these levels do not belong to any band structure in the current work. The 808 keV contamination peak in part (a) comes from the coincidence of the 808 and 915 keV ground state band transitions in ^{140}Ba, as reported in Ref. [81, 82, 83].

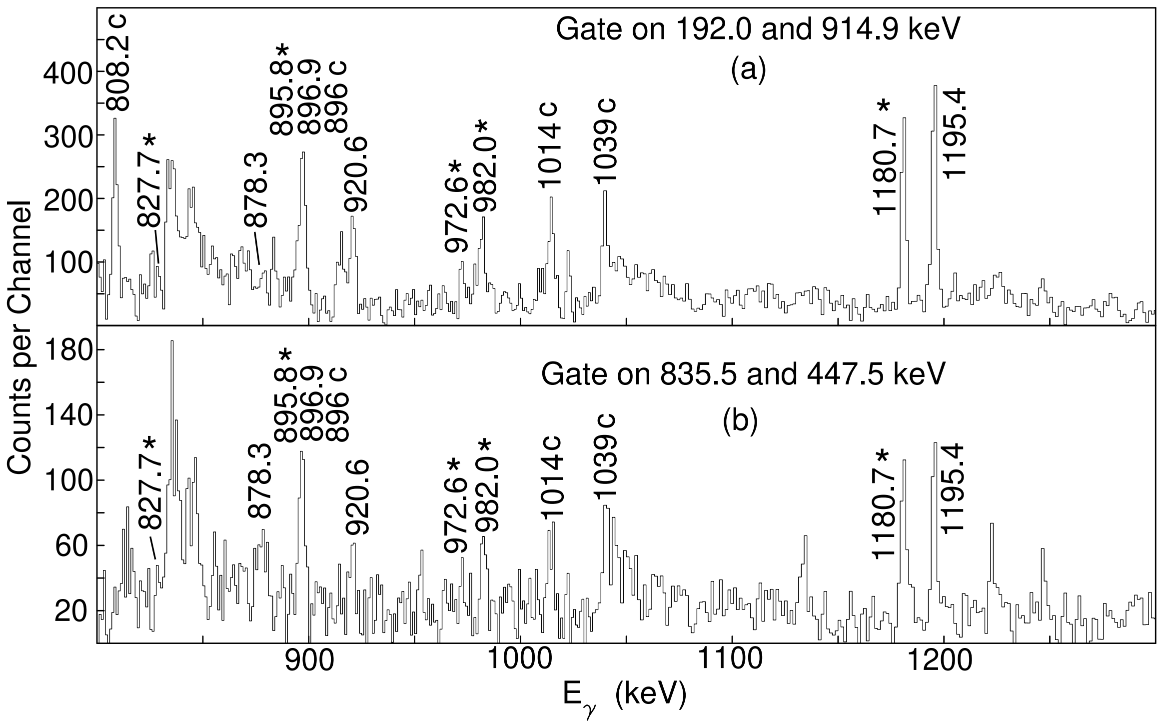

Figure 5.4: Partial γ-ray coincidence spectra by gating on (a) 192.0 and 914.9 keV transitions and (b) 835.5 and 447.5 keV transitions in ^{104}Mo. New transitions are labeled with an asterisk. Contamination transitions are labeled with a "c". Note that the 1180 and 1195 keV transitions are not placed in the level scheme.

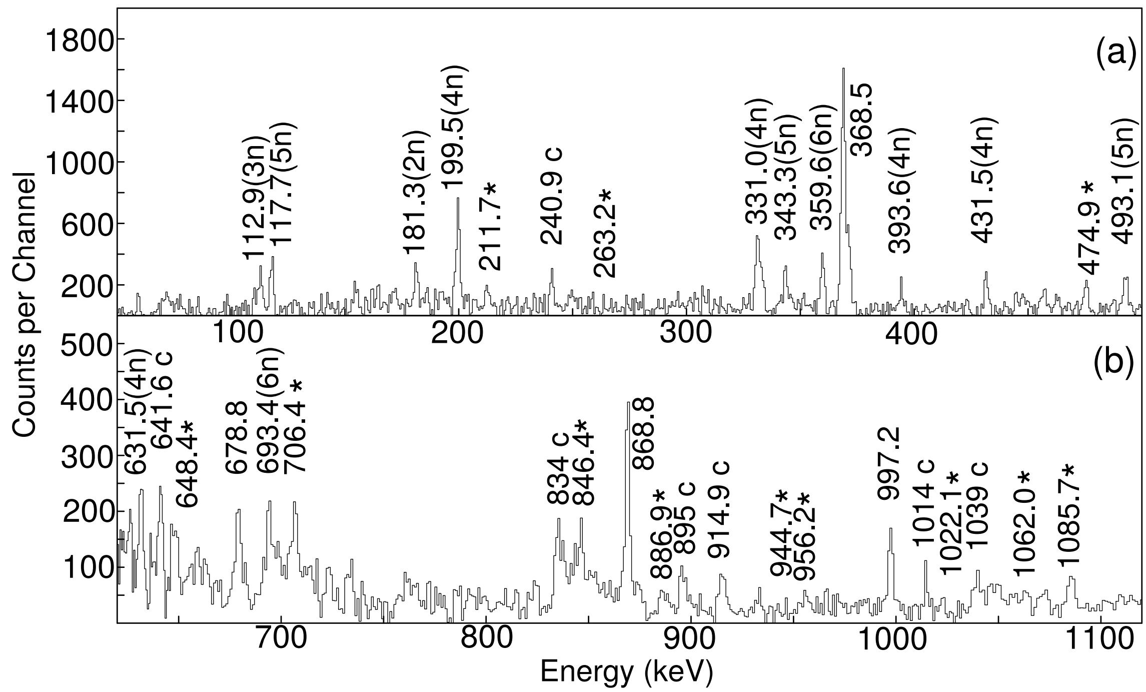

Figure 5.5: Partial γ-ray coincidence spectra by gating on (a) 192.0 and 982.0 keV transitions and (b) 192.0 and 1022.4 keV transitions in ^{104}Mo. New transitions are labeled with an asterisk. Contamination transitions are labeled with a "c". Note that the 706.4 and 1085.7 keV transitions in part (b) are not placed in the level scheme. Here 2n, 3n, 4n, 5n and 6n denote ^{146}Ba to ^{142}Ba, respectively.

Fig. 5.5 provides more evidence for band (5) in ^{104}Mo. The spectrum in part (a) shows a gate on 192.0 and 982.0 keV. One can see the new 211.7, 263.2 and 474.9 keV transitions populating the (6^-) level in band (5). Part (b) is a spectrum gated on 192.0 and 1022.4 keV transitions at high energy region. In this spectrum, one can see the new 648.4, 706.4, 846.4, 886.9, 944.7, 956.2, 1022.1, 1062.0 and 1085.7 keV transitions. The 846.4, 868.8, 997.2 and 1062.0 keV transitions are directly populating the 4^+ state in band (2). The 648.4, 886.9, 944.7 and 956.2 keV transitions are directly populating the 6^+ state in band (2). The 1022.1 keV transition populates the (8^+) state in band (2). The 706.4 and 1085.7 keV transitions depopulate from non-band levels. Thus, they are not included in Fig. 5.2.

Band (6) in ^{104}Mo was reported in Ref. [79]. Band (7) in ^{104}Mo was reported in Ref. [79, 84, 85]. This band (6) is reassigned as possible negative parity. In our data, we do not see the J to J-2 transitions in Ref. [79]. In detail, the even spin levels in band (6) only decay to the same spin ground state band levels, e.g the transition from 2179.6 keV 6^- level to the 560 4^+ keV transition is not seen in the data.

The new band (8) in ^{104}Mo is tentatively assigned as a three phonon γ-vibrational band. This is because of the proposed tentatively assigned 6^+ band head based on decay pattern and energy spacing. Also, this band only decays to the two phonon γ-vibrational band. However, this band could be another quasiparticle band. More work is needed to understand the structure and configuration of this band.

5.2.2 ^{106}Mo Spectra

In ^{106}Mo, the ground state band (1) and γ-vibrational band (2) and the two phonon γ vibrational band (3) levels have been confirmed. A band with a (5^+) bandhead at 2302.9 keV was reported in Ref. [79]. In the current work, the even spin levels of this band have been identified. The bandhead of the even spin of band 8 is reassigned as the 4^- at 2138.5 keV level based on the absence of the energetically favored decay to the 2^+ state and the 2302.6 keV level as 5^-. Likewise, from the decay pattern, this band (6) is assigned as

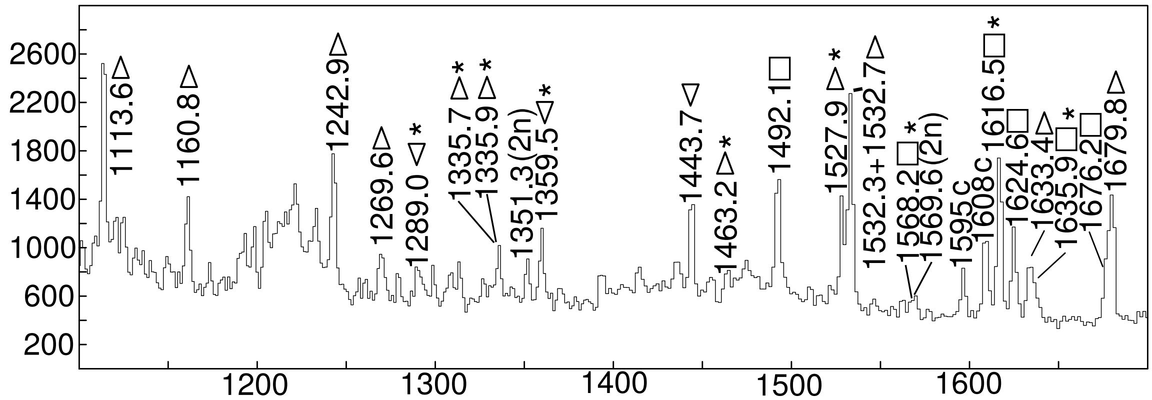

Figure 5.6: Partial γ-ray coincidence spectra by summing three gates on 171.5 and 350.5 keV, 350.5 and 511.0 keV, and 511.0 and 654.9 keV transitions in the ground state band of ^{106}Mo. Here □ represents the transitions populating the 4^+ level of the g.s. band, Δ denotes the transitions populating the 6^+ state of the g.s. band, ∇ represents the transitions populating the 8^+ state of the g.s. band. New transitions are labeled with asterisks. Contamination transitions are labeled with a "c". Here 2n represents transitions in ^{144}Ba. Note that the 1359.5 and 1633.4 keV transitions are not placed in the level scheme.

(4^-). Figs. 5.6 and 5.7 give evidence for this band structure. In Fig. 5.6 from a summation of three gates on the ground state band in ^{106}Mo, one can see the 1269.4 and 1679.8 keV transitions previously reported in Ref. [79] decaying from band (8) to the ground state band. The new 1289.0, 1463.2 and 1616.5 keV transitions decaying from band (8) to the ground state band are also seen in this spectrum. Other 1335.7, 1335.9, 1359.5, 1527.9, 1633.4, 1635.9 keV new transitions are also seen in this gate. The 1359.5 and 1633.4 keV transitions are real but not placed in the level scheme in Fig. 5.3. The 1351 and 1569 keV transitions from ^{144}Ba were identified previously in Ref. [82, 86]. Fig. 5.7 (a) and (b) show evidences for the M1 and E2 transitions in band (8). In Fig. 5.7 (a) with a gate on 1780.6, 350.5 and 171.5 keV transitions, the new 193.6 (6^- to 5^-), 216.6 (7^- to 6^-) and 264.1 keV (8^- to 7^-) M1 transitions in band (8) can be seen. In part (b) by gating on the 1616.5, 350.5 and 171.5 keV transitions, the new 164.1, 193.6 and 216.6 keV M1 transitions, as well as the new 357.7, 480.7 and 622.7 keV E2 transitions in band (8) can be seen.

The evidence for band (6) is shown in Fig. 5.8. By gating on the 1527.9 keV linking transitions from band (6) to g.s. band (1), and the 350.5 and 511.0 keV transitions in

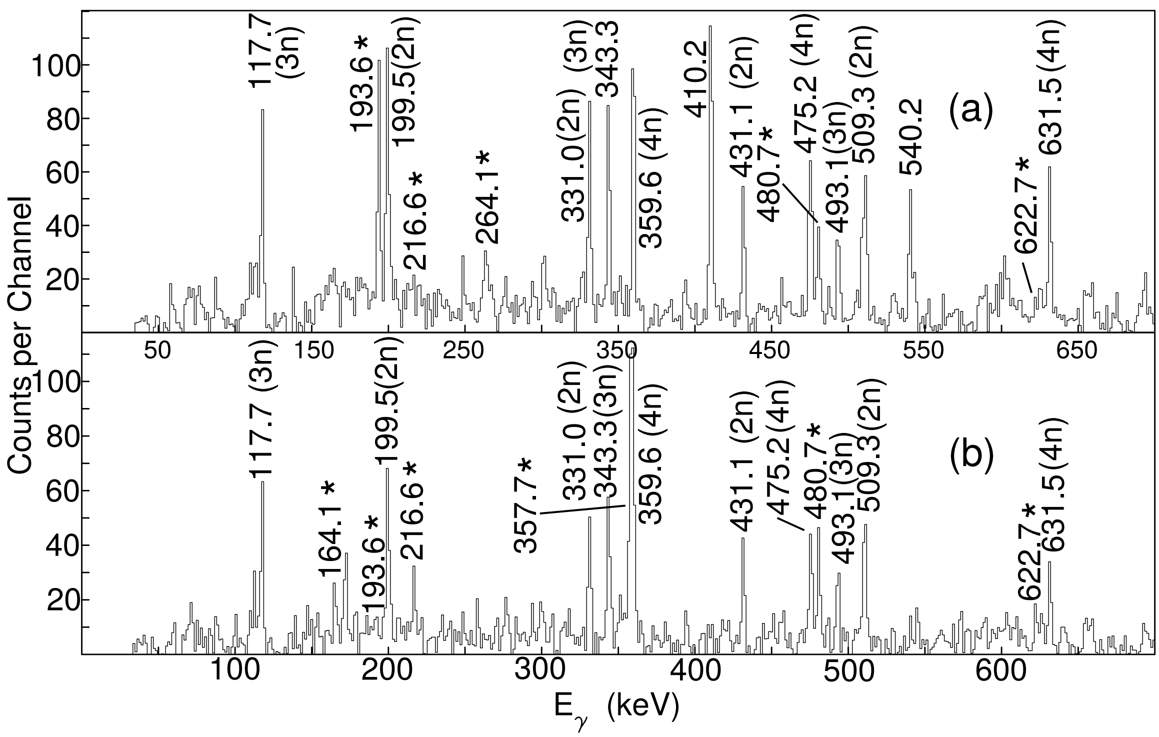

Figure 5.7: Partial γ-ray coincidence spectra in ^{106}Mo (a) by gating on the 1780.6, 350.5 and 171.5 keV transitions, and (b) by gating on the 1616.5, 350.5 and 171.5 keV transitions. New transitions are labeled with an asterisk. Fission partner transitions are labeled with neutron evaporation numbers. Namely, 2n, 3n, 4n denote ^{144}Ba, ^{143}Ba, ^{142}Ba, respectively.

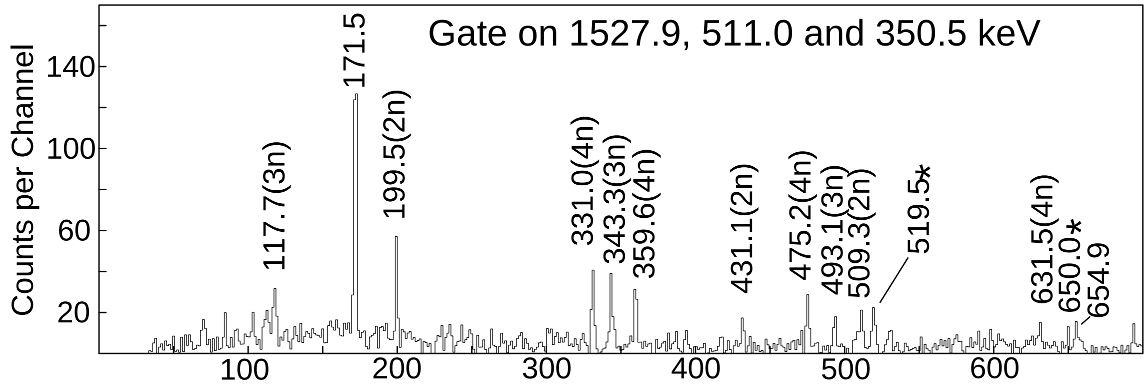

Figure 5.8: Partial γ-ray coincidence spectra by gating on 1527.9, 511.0 and 350.5 keV transitions in ^{106}Mo. New transitions are labeled with an asterisk. Fission partner transitions are labeled with neutron evaporation numbers. Here 2n, 3n, 4n, 5n denote ^{144}Ba, ^{143}Ba, ^{142}Ba and ^{141}Ba, respectively.

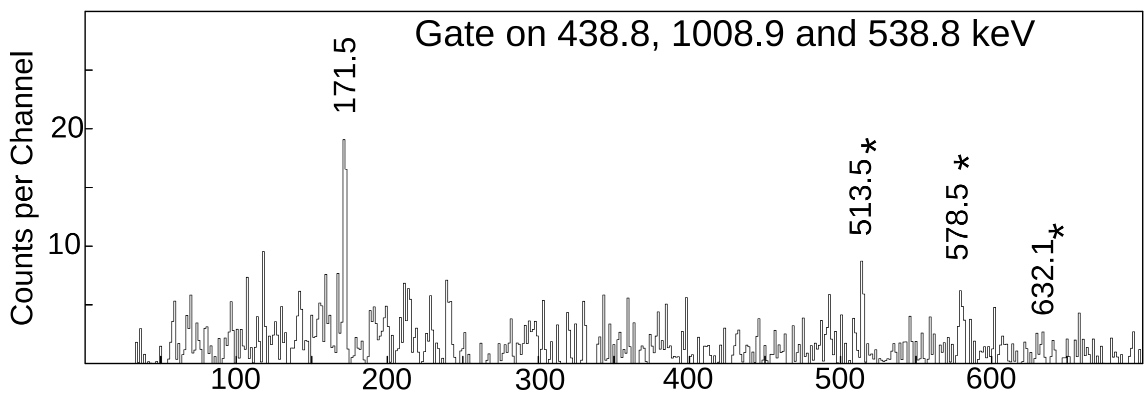

Figure 5.9: Partial γ-ray coincidence spectra by gating on 438.8, 1008.9 and 538.8 keV transitions in ^{106}Mo. New transitions are labeled with an asterisk.

band (1), the new 519.5 and 650.0 keV E2 transitions in band (6) can be observed in the spectrum. The Ba fission partners transitions as well as the 171.5 keV g.s. band transition are also labeled in the figure. The 654.9 keV transition is proposed to be a contamination because the peak is much weaker than the 171.5 keV. It comes from the coincidence of 350.5, 511.0 and the background around the 1527.9 keV region.

Some of the linking transitions from band (10) to band (1) are shown on Fig. 5.6. Figure 5.9 gives evidence for the E2 transitions in band (10). The new 513.5, 578.5 and 632.1 keV can be seen in this figure with the 438.8, 1008.8 and 538.8 keV gate.

5.2.3 Angular Correlations

Angular correlation measurements have been made to determine the spins and parities in ^{104,106}Mo. For ^{104}Mo, as shown in Fig. 5.10, the two results generally agree with theoretical 4(D)4(Q)2 and 5(D)5(Q)3 values, which are A_2=0.196, A_4=0, and A_2=0.186, A_4=0, respectively. These measurements confirm the assignments of the 4^- and 5^- states in band (4). The band-head of band (5) is tentatively argued as 5^- according to the decay pattern and level energy differences. The 5^- - 4^+ transition is seen but not the energetically favored 5^- - 3^+ which should be seen if parity is positive and similarly for the spin 6, 7 and 8 levels. The angular correlation of the 1323-368 keV cascade in ^{104}Mo shows evidence for the 5 spin of the 1883 level. As a comparison, Ref. [79] assigned tentative 5- for this level without any further discussions. However, the A2, A4 values of the 1323-368 keV angular correlation is within 1 sigma error of a theoretical pure dipole. Therefore, because of the large uncertainty, the result does not show clear evidence for the parity assignment. In this paper, we did not assign the parity of this band-head 1883 level. If the band 7 in ^{104}Mo is the signature partner of band 6, the parity of band 7 would be negative.

For ^{106}Mo, the spins/parities of 2^+ to 8^+ levels in γ-band, and the 4^+ to 7^+ levels in the $\gamma\gamma$ band were confirmed by the directional correlations from oriented states (DCO) in Ref. [76]. These assignments of the 2^+ to 7^+ levels in the γ-band were also confirmed by the γ-γ angular correlation measurements [1]. As shown in Table. 5.3, the 1434.6 keV 4^+ bandhead of the γ-γ band is confirmed by the current angular correlation measurements. The spin and parity of the 7^+ state of the $\gamma\gamma$ band is confirmed by the 542.0-772.5 keV cascade. The 517.4-724.3 keV cascade angular correlation agrees with a pure 5^-(D)4^+(Q)2^+ pattern. This measurement confirms the 1952.0 keV 5^- level in band (4) of ^{106}Mo. The measurement of the 190.2-517.4 keV cascade can give the E2/M1 mixing ratio of the 190.2 keV transition (from 2142.0 keV level to 1952.0 keV level) in band (4) by assuming a pure E1 517.4 keV transition. The two values of -0.6 and -1.9 correspond to 26% quadrupole vs. 74% dipole and 78% quadrupole vs. 22% dipole for the 190.2 keV transition, respectively

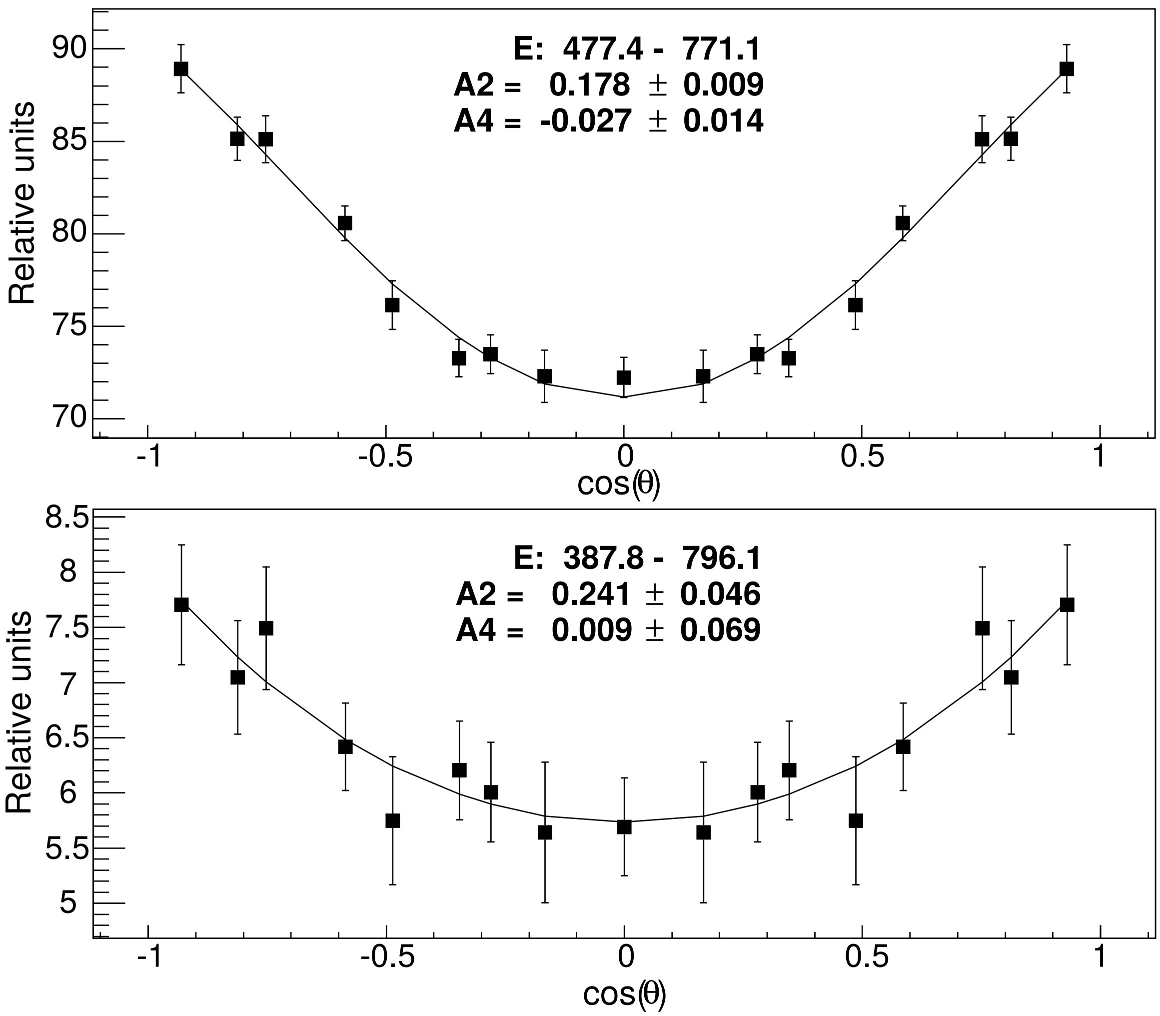

Figure 5.10: The γ-γ angular correlations of 477.4 - 771.3 keV (top), and 387.8 - 796.2 keV (bottom) in ^{104}Mo.

Table 5.3: Angular correlations of the ^{104,106}Mo nuclei. Here D represents a dipole transition and Q represents a quadrupole transition. The δ represents the E2/M1 mixing ratios. Other angular correlations from Ref [1] are indicated by an asterisk.

Cascade	A_2,A_4 exp.	A_2,A_4 theo.	Decay pattern	δ
^{104}Mo				
*620.0 - 192.0	-0.15(3), 0.4(1)		2^+(Q/D)2^+(Q)0^+	9, (0.6)
*835.5 - 192.0	-0.19(2), -0.12(4)		3^+(Q/D)2^+(Q)0^+	50, (-0.15)
*654.0 - 368.5	-0.16(1), 0.16(2)		4^+(Q/D)4^+(Q)2^+	7
*914.9 - 368.5	-0.10(1), -0.6(2)		5^+(Q/D)4^+(Q)2^+	30
*956.6 - 519.3	-0.01(3), 0.07(5)		7^+(Q/D)6^+(Q)4^+	0.1, (7)
*961.0 - 641.6	0.10(6), -0.15(9)		9^+(Q/D)8^+(Q)6^+	3, (0.31)
1322.6 - 368.5	-0.10(3), -0.02(5)	-0.07, 0	5(D)4^+(Q)2^+	
477.4 - 771.1	0.18(1), -0.03(1)	0.20, 0	4^-(D)4^+(Q)2^+	
387.8 - 796.1	0.24(5), 0.01(7)	0.19, 0	5^-(D)5^+(Q)3^+	
^{106}Mo				
*538.8 - 171.5	-0.18(2), 0.27(8)		2^+(Q/D)2^+(Q)0^+	6.2, (0.65)
*713.5 - 171.5	-0.08(1), -0.08(3)		3^+(Q/D)2^+(Q)0^+	6.1, (-0.01)
*545.4 - 350.5	-0.19(1), 0.11(2)		4^+(Q/D)4^+(Q)2^+	(2.1)
*784.6 - 350.5	0.023(7), -0.05(1)		5^+(Q/D)4^+(Q)2^+	4.4
*530.0 - 511.0	-0.07(2), 0.04(3)		6^+(Q/D)6^+(Q)4^+	1.1, (5)
*834.6 - 511.0	0.08(3), -0.08(5)		7^+(Q/D)6^+(Q)5^+	3.2, 0.26
724.3 - 710.3	0.11(1), 0.02(2)	0.10, 0	4^+(Q)2^+(Q)0^+	
542.0 - 772.5	0.11(5), -0.04(7)	0.10, 0	7^+(Q)5^+(Q)3^+	
517.4 - 724.3	-0.08(1), -0.01(2)	-0.07, 0	5^-(D)4^+(Q)2^+	
190.2 - 517.4	0.26(2), -0.03(3)		6^-(Q/D)5^-(D)4^+	-0.6, -1.9
226.3 - 484.6	0.29(3), 0.05(5)		7^-(Q/D)6^-(D)5^+	-1.0

and B(M1;190.2,$6^- \rightarrow 5^-$)/B(E2;190.2,$6^- \rightarrow 5^-$) values for 0.070 and 0.0070 $(\mu_N/eb)^2$, respectively. For the 226.3-485.0 keV cascade, the measured A_2 is a little larger than the maximum value for the 7^-(Q/D)6^-(D)5^+. Therefore, only one value of the E2/M1 mixing ratio is obtained. The -1.0 value corresponds to 50% quadrupole vs. 50% dipole, and 0.036 $(\mu_N/eb)^2$ for B(M1;226.3,$7^- \rightarrow 6^-$)/B(E2;226.3,$7^- \rightarrow 6^-$) in band (4).

5.2.4 TPSM Calculations

The quantum mechanical triaxial projected shell model (TPSM) is used to understand the band structure and signature splitting of the neutron-rich nuclei. Various phenomena related to triaxial shapes of nuclei, like γ-vibrations [56], chiral symmetry [57, 58] , and wobbling modes [87], have been successfully described using the TPSM. In general, the TPSM calculations proceed in several stages.

The basic strategy of the TPSM approach is similar to the spherical shell model with the only difference that deformed basis are employed for diagonalizing the shell model Hamiltonian rather than the spherical one. The deformed basis are constructed by solving the triaxial Nilsson potential with optimum quadrupole deformation parameters of ε and ε'. In principle, the deformed basis can be constructed with arbitrary deformation parameters, however, the basis are constructed with expected or known deformation parameters (so called optimum) for a given system under consideration. These deformation values lead to an accurate Fermi surface and it is possible to choose a minimal subset of the basis states around the Fermi surface for a realistic description of a given system. The Nilsson basis states are then transformed to the quasiparticle space using the simple Bardeen–Cooper–Schriefer ansatz for treating the pairing interaction.

As the deformed basis are defined in the intrinsic frame of reference and do not have well defined angular momentum, in the second stage these basis are projected onto states with well defined angular momentum using the angular momentum projection technique [88, 89, 90]. The three-dimensional angular mommentum projection operator is given by

$$\hat{P}^{I}_{MK} = \frac{2I+1}{8\pi^2}\int d\Omega D^{I}_{MK}(\Omega)\hat{R}(\Omega) \tag{5.1}$$

with the rotation operator

$$\widehat{R}(\Omega) = e^{-i\alpha\hat{J}_z}e^{-i\beta\hat{J}_y}e^{-i\gamma\hat{J}_z} \tag{5.2}$$

Here, 'Ω' represents a set of Euler angles (α, γ = [0, 2π], β = [0, π]) and the $\hat{J}$'s are angular momentum operators.

In majority of the nuclei, near-yrast spectroscopy up to I = 20 is well described using basis space of two-neutron, two-proton and two-neutron plus two-proton configurations as one expects two-protons to align after two-neutrons rather than four-neutrons considering the blocking argument. However, this may not be the case for all the nuclei and there are indications that four neutron states may become important in the description of high-spin states in some rare-Earth region nuclei [91]. For odd-proton (neutron) systems, the basis space is composed of one-quasiproton (quasineutron) and two-quasineutrons (quasiprotons). In the case of odd–odd nuclei, the basis space is simply one-quasiproton coupled to one-quasineutron. This basis space for odd and odd–odd nuclei is also quite limited and needs to be extended for describing the higher spin states more accurately.

The advantage of the TPSM approach is that not only the yrast band, but also the rich excited band structures can be investigated. The Nilsson triaxial quasiparticle states do not have well defined projection along the symmetry axis, Ω and are a superposition of these states. For instance, the triaxial self-conjugate vacuum state is a superposition of K = 0, 2, 4,....states–only even-states are possible due to symmetry requirement [92]. For the symmetry operator, $\hat{S}$ = $e^{-i\pi\hat{J}_z}$, this gives the following projections operator:

$$\hat{P}^{I}_{MK} = \hat{P}^{I}_{MK}\hat{S}^{\dagger}|\Phi\rangle = e^{i\pi(K-\kappa)}\hat{P}^{I}_{MK}|\Phi\rangle \tag{5.3}$$

where, $\hat{S}|\Phi\rangle = e^{i\pi(K-\kappa)}|\Phi\rangle$, and κ characterizes the intrinsic states. For the self-conjugate vacuum state κ = 0 and, therefore, it follows from the above equation that only K = even, values are permitted for this state. For 2-qp states, the possible values for K-quantum number are both even and odd depending on the structure of the qp state. For the 2-qp state formed from the combination of the normal and the time-reversed states, K = 0 and again only K = even values are permitted. For the combination of the two normal states, K = 1, and only K = odd states are allowed.

The projected states for a given configuration that constitute a rotational band are obtained by specifying the corresponding K-value in the angular-momentum projection operator. The projected states from K = 0, 2 and 4 correspond to ground-, γ- and $\gamma\gamma$-bands, respectively. As stated earlier, for two-quasiparticle states, both even- and odd-K values are permitted, depending on the signature of the two quasiparticle states. In this description, the aligning states that cross the ground-state band and lead to upbend or backbend phenomenon have low-K configurations. These states are close to the rotational axis as compared to the deformation axis and can be easily aligned. The projection from the same quasiparticle intrinsic state with K' = K + 2 is the γ-band built on these quasiparticle state.

In the third and the final stage of the TPSM analysis, the projected basis are employed to diagonalize the shell model Hamiltonian. The model Hamiltonian consists of pairing and quadrupole–quadrupole interaction terms, i.e.

$$\hat{H} = \hat{H}_0 - \frac{1}{2}\chi\Sigma_\mu \hat{Q}^\dagger_\mu \hat{Q}_\mu - G_M \hat{P}^\dagger \hat{P} - G_Q \Sigma_\mu \hat{P}^\dagger_\mu \hat{P}_\mu \tag{5.4}$$

In the above equation, $\hat{H}_0$ is the spherical single-particle Nilsson Hamiltonian [93]. The parameters of the Nilsson potential are fitted to a broad range of nuclear properties and is quite appropriate to employ it as a mean-field potential.

We have performed theoretical calculations for the chiral doublet bands in ^{104,106}Mo. Bands (4) and (5) in ^{104,106}Mo are proposed to be the chiral partners. As seen in Figs. 5.12

and 5.13, the chiral bands in ^{104,106}Mo exhibit small signature splitting, and the same rotational response $I(\omega)$. The energy differences of the doublet bands are quite small and almost constant with increasing spin, being about half of that differences in ^{104}Mo compared to ^{106}Mo, as shown in Fig. 5.14. These are the characteristics of very soft chiral vibrations.

In recent years the triaxial projected shell model (TPSM) approach has been shown to reproduce the high-spin properties of deformed nuclei quite well [94, 95, 96, 97]. In this approach, the model space is composed of three major oscillator shells for neutrons and protons with pairing plus quadrupole-quadrupole as the model Hamiltonian. In the original version of the model, quasiparticle excitations were restricted to the last major oscillator shell and due to this limitation, it was possible to study only positive parity bands in even-even systems. In order to investigate the negative parity band structures, populated in the present experimental work, the TPSM approach has been generalized by considering two-quasiparticle excitations from two major oscillator shells with one neutron (proton) in one oscillator shell and the second neutron (proton) in the other oscillator shell having opposite parity. More details on this extension shall be provided in separate publications [94].

By using the extended approach, numerical calculations have been performed for the negative parity bands observed in ^{104,106}Mo with the following parameter set: $\varepsilon = 0.24$, $\gamma = 20^{\circ}(104),\ 36^{\circ}(106)$. The other parameters are quoted in our earlier study of the positive parity bands in [98].

The calculated levels in band 4 and band 5 in ^{104,106}Mo, respectively, are shown in Fig. 5.11. The energies are normalized to the band 4 bandhead of these two nuclei, respectively. Experimental data are also included for comparison. In ^{104}Mo, the calculations of band 4 and band 5 have regular energy spacing of rotational bands and can reproduce the experimental data. In ^{106}Mo, the calculated 5^- level of band 4 is just 2 keV above the 4^- bandhead. Thus, the 1936 keV 4^- level in experiment is assigned to the bandhead of band 4, and all the previously assigned 5^- (1952 keV) band levels are now assigned to the new

4^- band 4. All the previously assigned 4^- (1936 keV) band levels at spin 5 and higher are now assigned to the new 5^- band 5. The 1817 keV 3^- level is considered to be a non-band one.

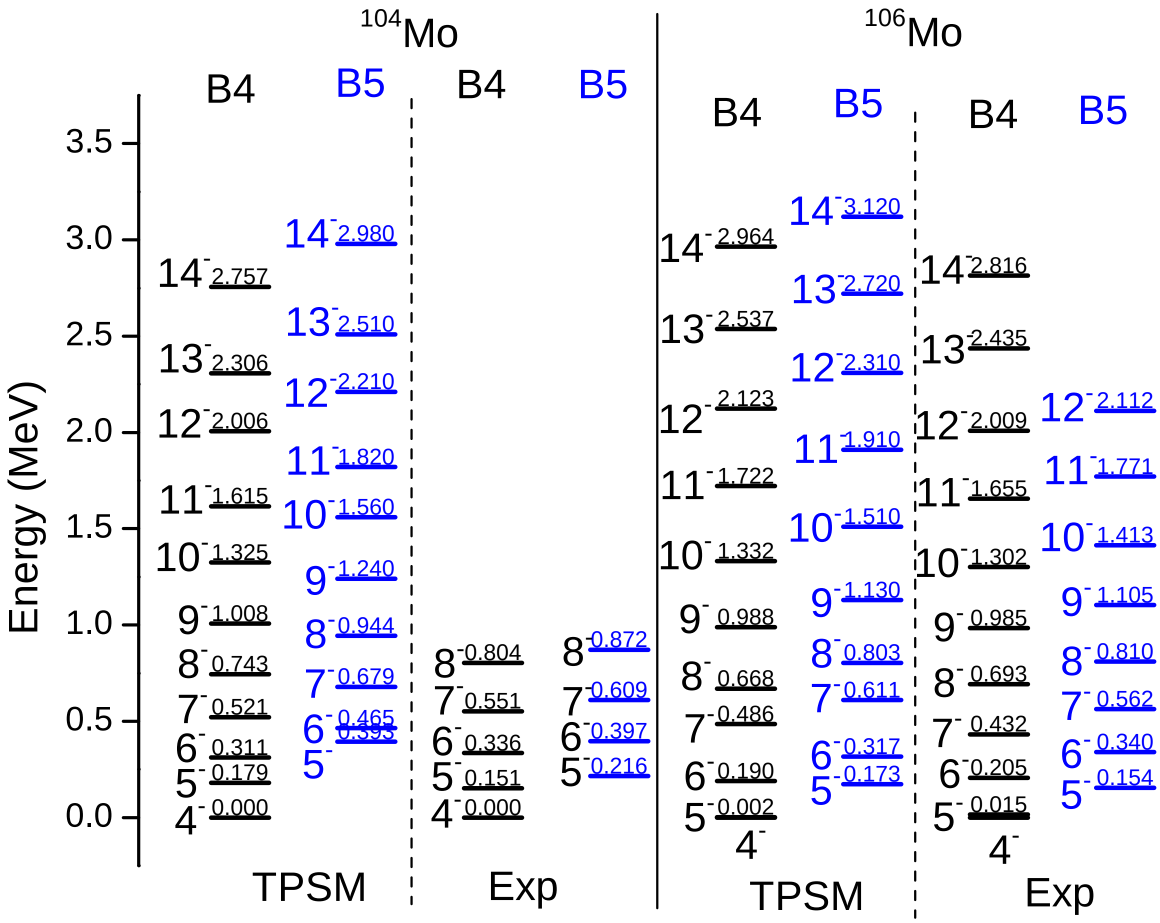

Figure 5.11: Comparison of the TPSM calculated energy level to the experimental data. Energies are normalized to the 4^- band head energies of ^{104,106}Mo, respectively.

The calculated TPSM energies for two nuclei are included in Fig. 5.12 along with the observed energies. Note that, the 12^- state in band 5 of ^{106}Mo is different from the previous work in Ref. [2, 13]. The TPSM approach reproduces the observed energies well (note the expanded energy scale). At large angular momentum the TPSM overestimates the energies, which is seen in the angular momentum vs. frequency plots Fig. 5.13, as a too small slope for ^{106}Mo.

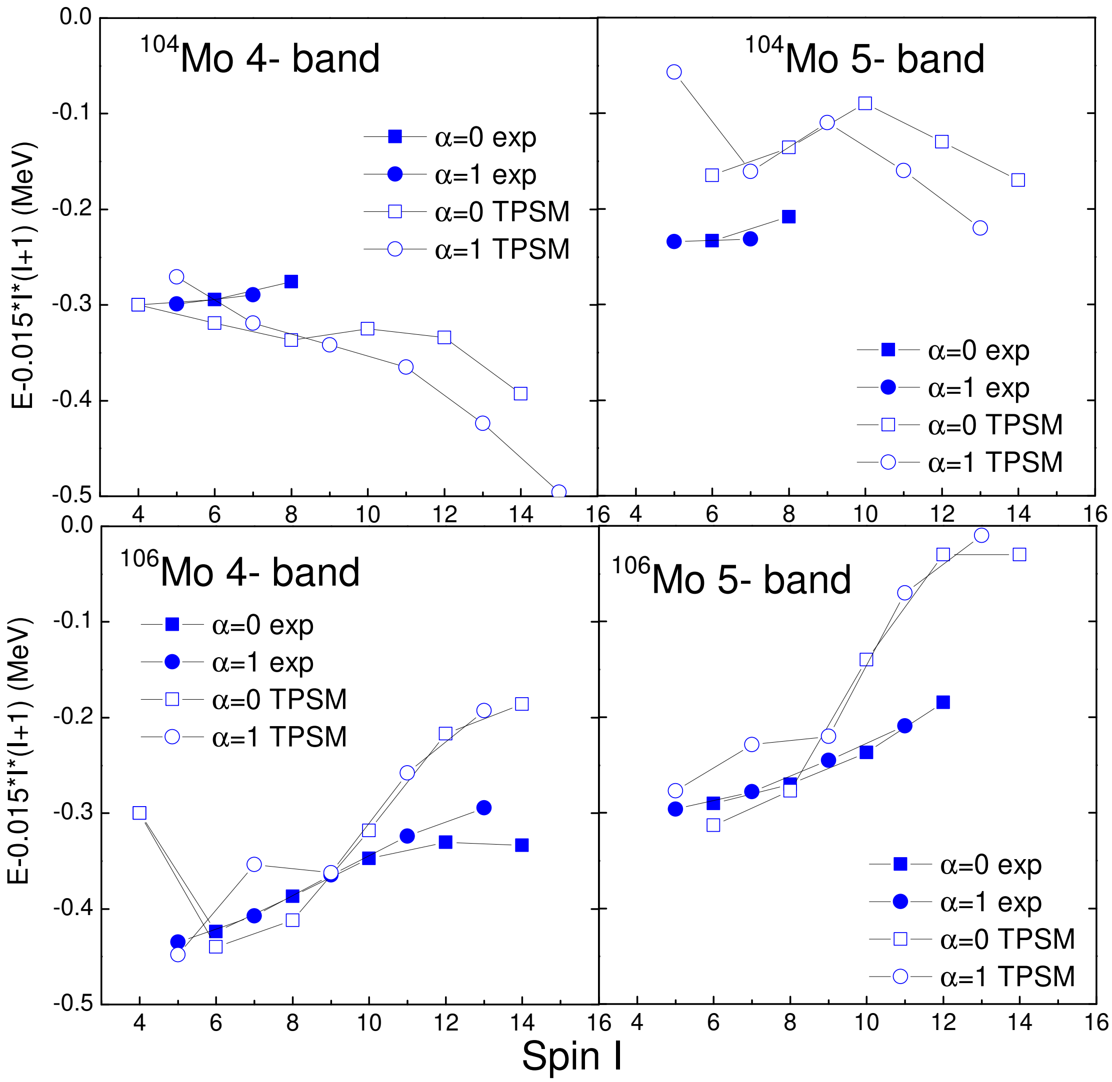

Figure 5.12: Comparison of the measured energy levels E-0.015*I*(I+1) vs Spin (I) for ^{104,106}Mo with TPSM Calculated values. Data for ^{106}Mo has been taken from Ref. [2] and the current work. Here E is normalized to the 4^- band head energy in band 4 in ^{104,106}Mo, respectively.

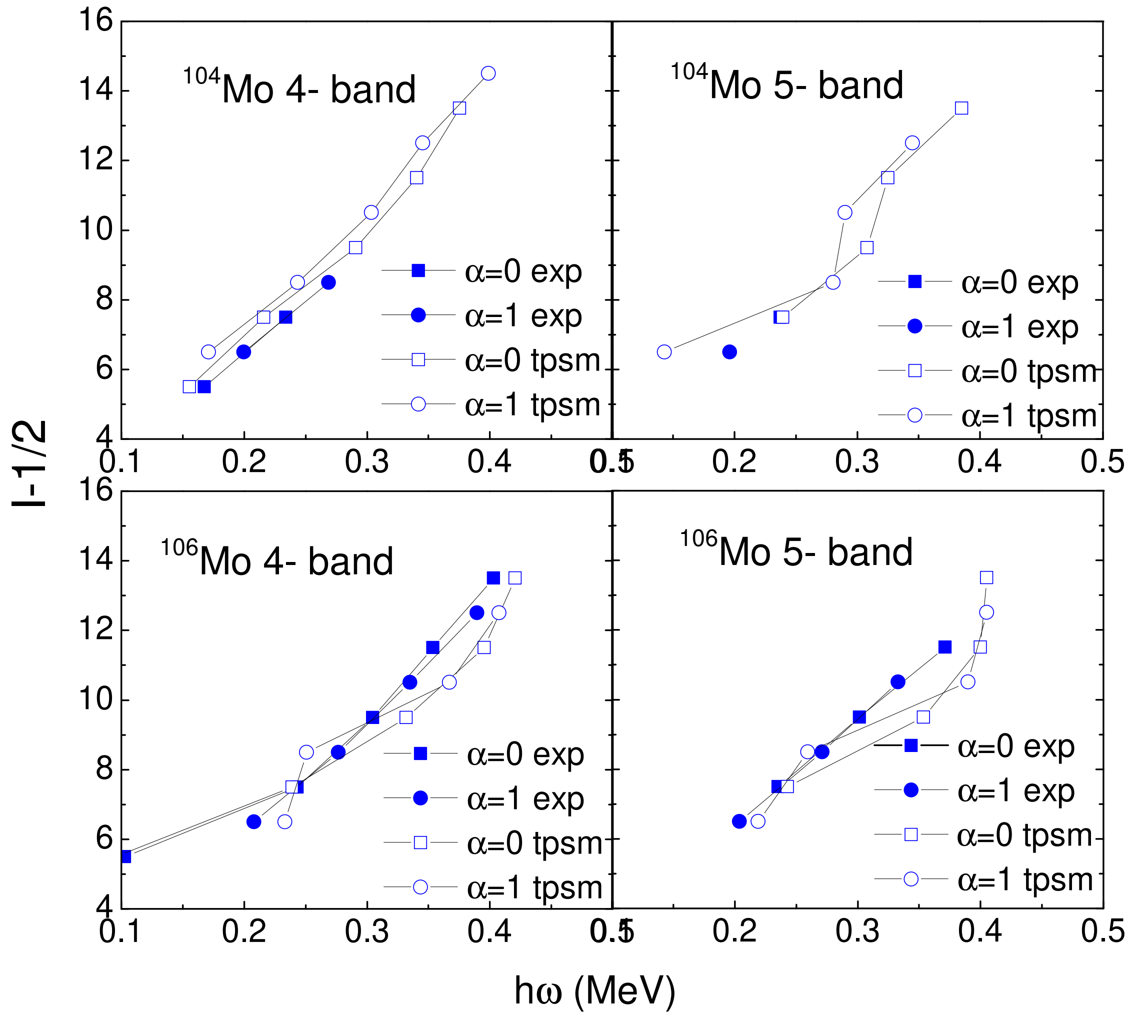

Figure 5.13: Plots of $I - 0.5$ vs rotational frequency $\hbar\omega = (E(I) - E(I-2))/2$ for ^{104,106}Mo from the experiment and TPSM calculations.

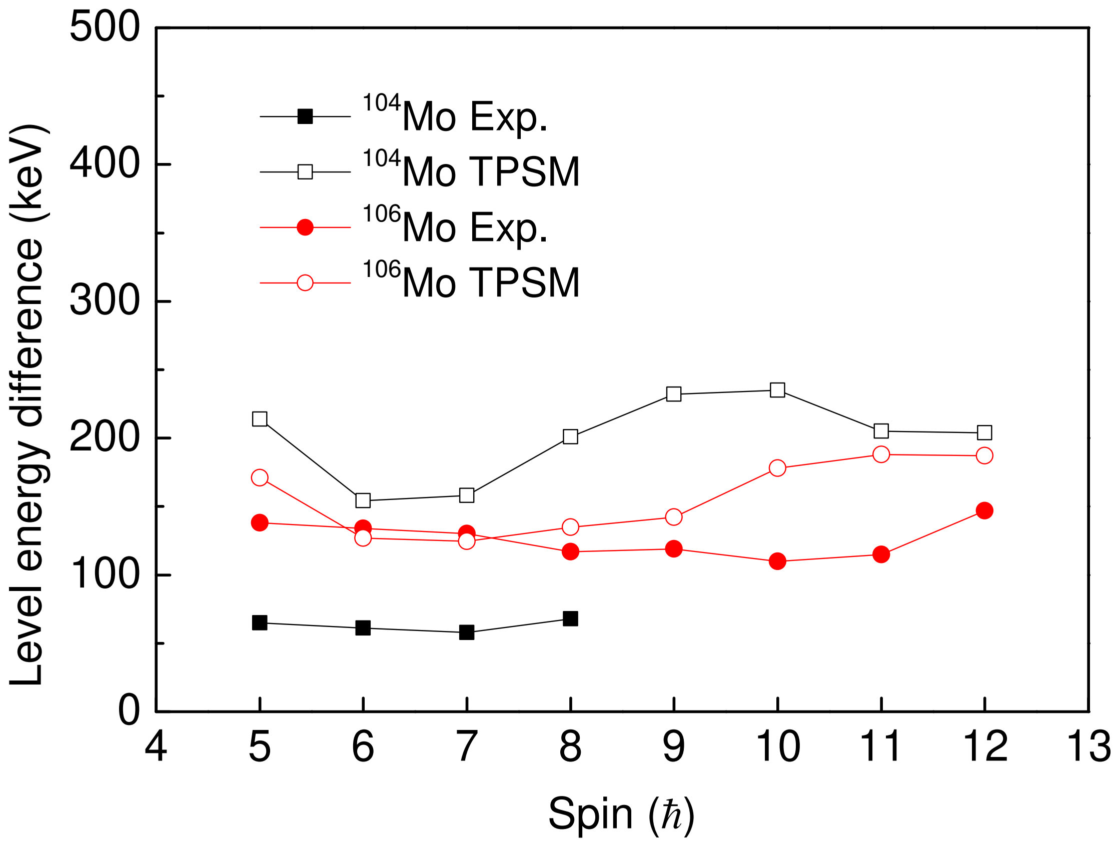

Figure 5.14: Level energy differences $E_5(I) - E_4(I)$ between chiral doublet bands in ^{104,106}Mo from the experiment and TPSM calculations.

For ^{104}Mo, the calculations trend towards underestimation for band (4) and they overestimate band (5) at low spins but may also be trending towards underestimation at higher spins. (Of course, neither sequence in ^{104}Mo is observed above I=8, so one can only extrapolate.) We attribute the discrepancy to the assumption of a fixed deformation in the TPSM. Fig. 5.14 displays that the key feature of chiral partner bands -the small distance between states of the same I- is reasonably in agreement with the TPSM calculations.

The calculated $J^{(1)}$ moments of inertia are also compared with the experimental data from the current work. As shown in Fig. 5.15, the calculations show staggering at low spin which differs from the experimental data. However, the staggering of $J^{(1)}$ can be generally reproduced for they are centered around the experimental data. At medium spin

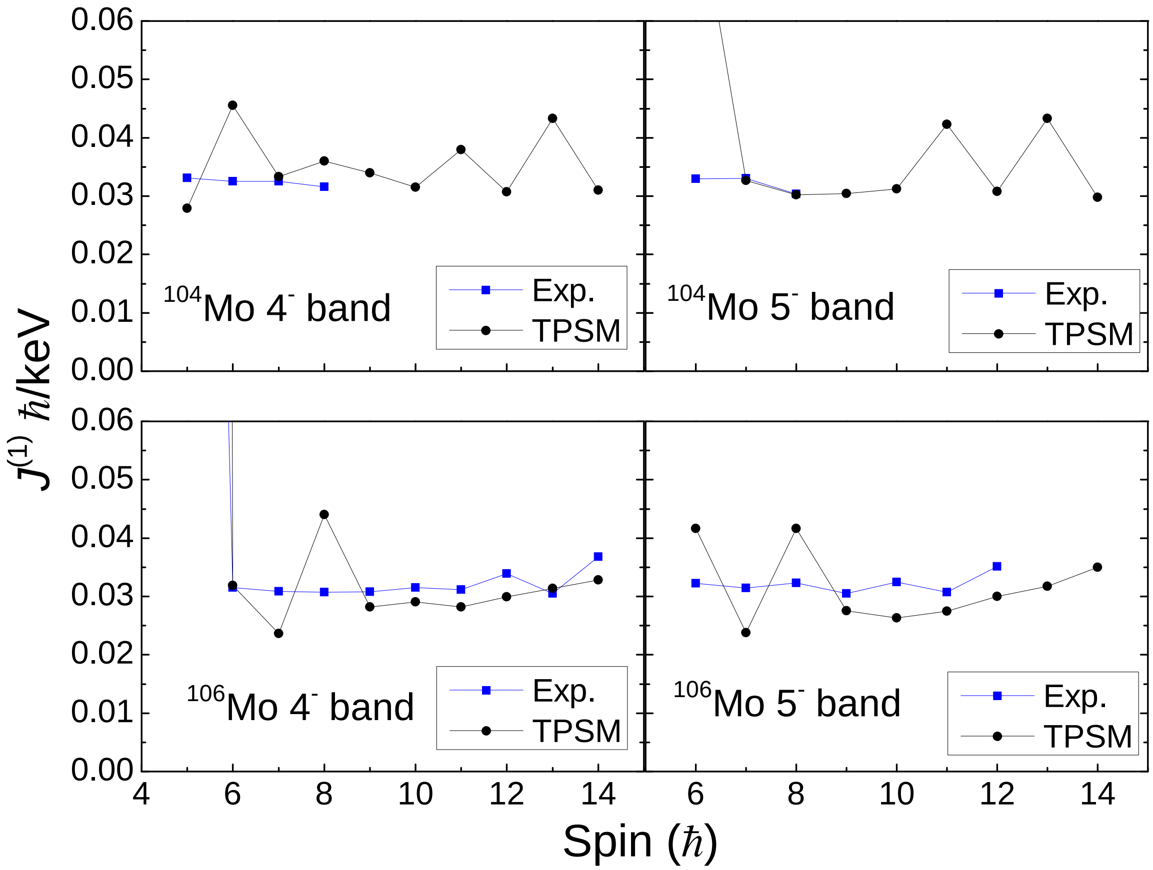

Figure 5.15: Comparison of the $J^{(1)}$ moments of inertia in band 4 and 5 between TPSM calculations and experimental data.

both experimental data and calculated results are flat. The calculations also predict large staggering at high spin for ^{104}Mo without experimental data for comparison.

The transition probabilities were also evaluated using the TPSM wavefunctions. These have been calculated using free values for g_l and for g_s with an attenuation factor of 0.85, i.e., $g_l^\pi = 1$, $g_l^\nu = 0$, $g_s^\pi = 5.59 \times 0.85$ and $g_s^\nu = -3.83 \times 0.85$. Comparison of the experimental and the calculated ratios of $B(M1)/B(E2)$ transition probabilities for ^{104,106}Mo are depicted in Fig. 5.16. It is observed from this figure that the numerical results obtained from TPSM with the present parameter set are generally in agreement with all the features of the observed data. The calculation also present the sudden drop of the $B(M1)/B(E2)$ ratios in band 4 of ^{104}Mo at $I = 6-8$ due to band crossing (which is also seen in Fig. 5.12 as the irregularity at low I.)

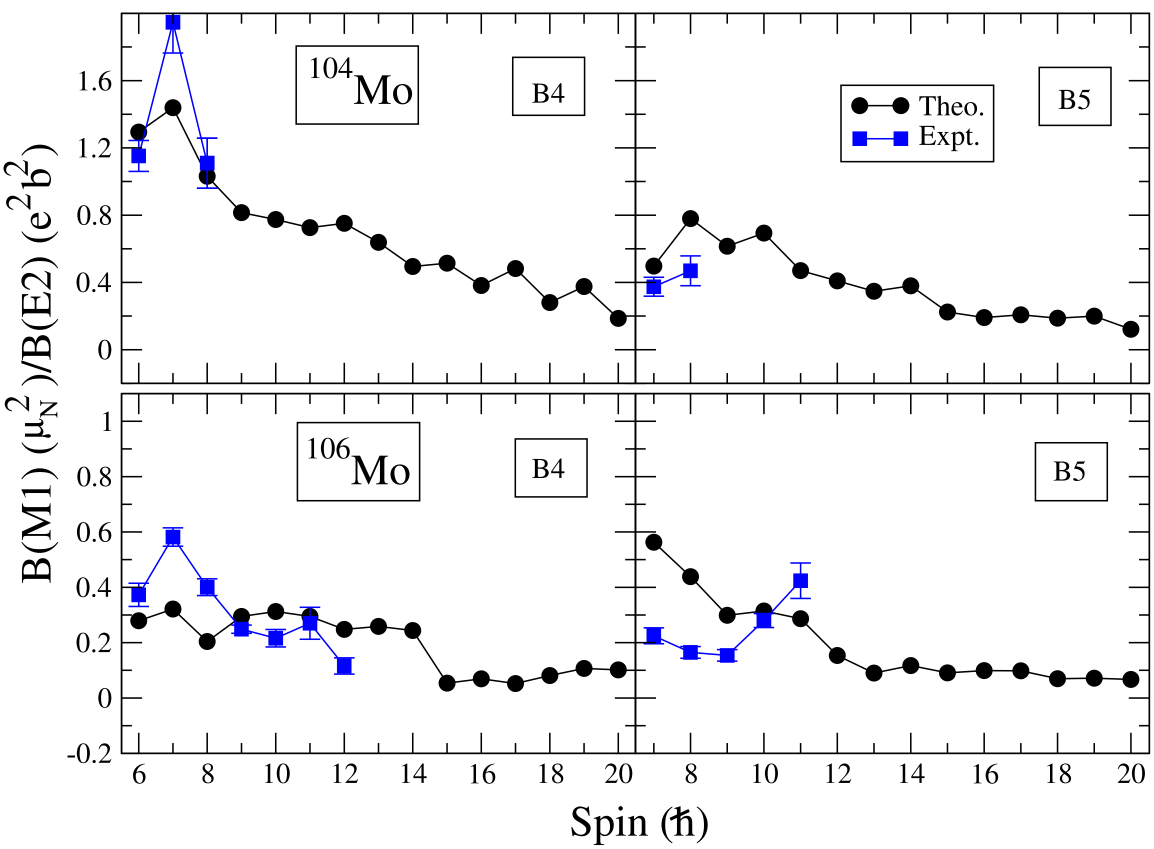

Figure 5.16: Comparison of the measured $B(M1)(\mu_N^2)/B(E2)(e^2b^2)$ shown as square with TPSM Calculated values shown as circle for ^{104,106}Mo nuclei.

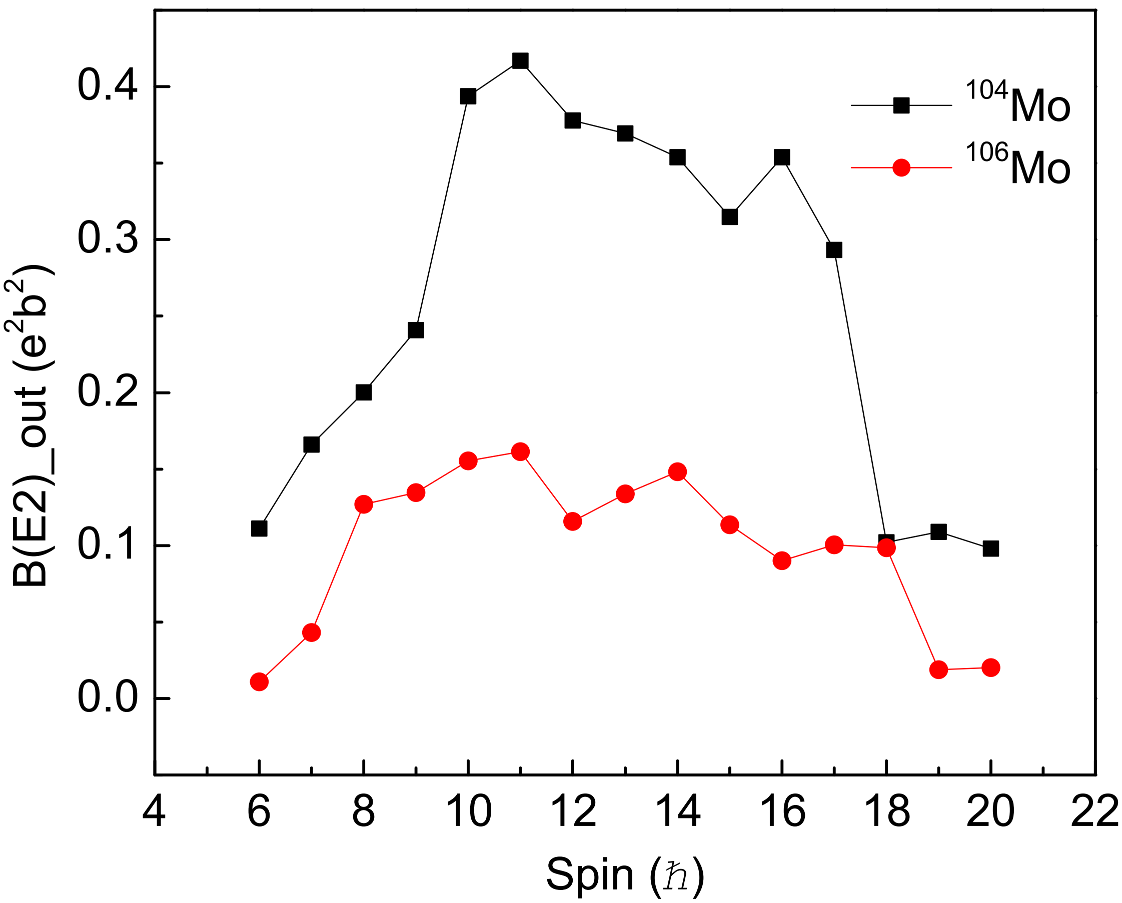

Figure 5.17: $B(E2, I \to I-1)_{out}$ values for the transitions connecting bands 5 and 4 from TPSM calculation.

Fig. 5.17 shows the $B(E2, I \to I-1)_{out}$ values for the transitions connecting bands 5 and 4. They are highly collective, about 40-90% of the stretched intraband values $B(E2, I \to I-2)_{in}$ at most of the spins. The high collectivity indicates that the two bands are related by reorientation of the triaxial charge density with respect to the total angular momentum vector. This is in contrast to the possibility that the two bands represent just two different quasineutron configurations, in case which the $B(E2, I \to I-1)_{out}$ would be only of the single particle value. The enhancement strongly supports the interpretation of the bands as chiral partners.

From the TPSM calculated B(E2)$_{out}$ and B(E2)$_{in}$ ratios, combined with the E2$_{in}$ transition intensities measured from the experimental data, one can calculate the expected

E2$(I \rightarrow I-1)_{out}$ intensities. The results are shown in Table 5.4. Although those connecting transitions can not be clearly identified, some upper limits are given for some of the cases with very weak evidence. Generally speaking, the calculated intensities are too weak to be seen (at least a magnitude smaller than the other strong transitions populating the same state). However, those deduced intensities are within the experimental limits.

Table 5.4: Comparison of the intensities of the expected $I \rightarrow I-1$ transitions connecting bands 5 and 4 between TPSM calculations and experimental limit. Here B(E2)$_{out}$ corresponds to the calculated values for the $I \rightarrow I-1$ transitions connecting bands 5 and 4, B(E2)$_{in}$ corresponds to the calculated values for the $I \rightarrow I-2$ transitions in band 5.

spin	B(E2)$_{out}$/B(E2)$_{in}$	E$_\gamma$ (keV)	I$_{\gamma-theo}$	I$_{\gamma-exp}$
^{104}Mo				
7	0.725	273.2	0.0059	
8	0.677	321.0	0.0027	
^{106}Mo				
7	0.294	356.2	0.16	<0.2
8	0.766	377.7	0.13	<0.15
9	0.745	412.0	0.087	<0.1
10	0.801	428.5	0.053	
11	0.813	468.8	0.027	
12	0.634	500.8	0.0074	<0.02

The analysis of the wave functions provides further support. As in the TAC calculations of Ref. [2], it is found, that the main components come from two configurations that contain one $h_{11/2}$ quasineutron and one from a pseudo spin pair of $(d_{5/2}g_{7/2})$ quasineutrons. The partner bands differ by the weights of the components with different angular momentum K that are projected from these two two-quasineutron configurations. This indicates that the partner bands are related by a reorientation of the total angular momentum.

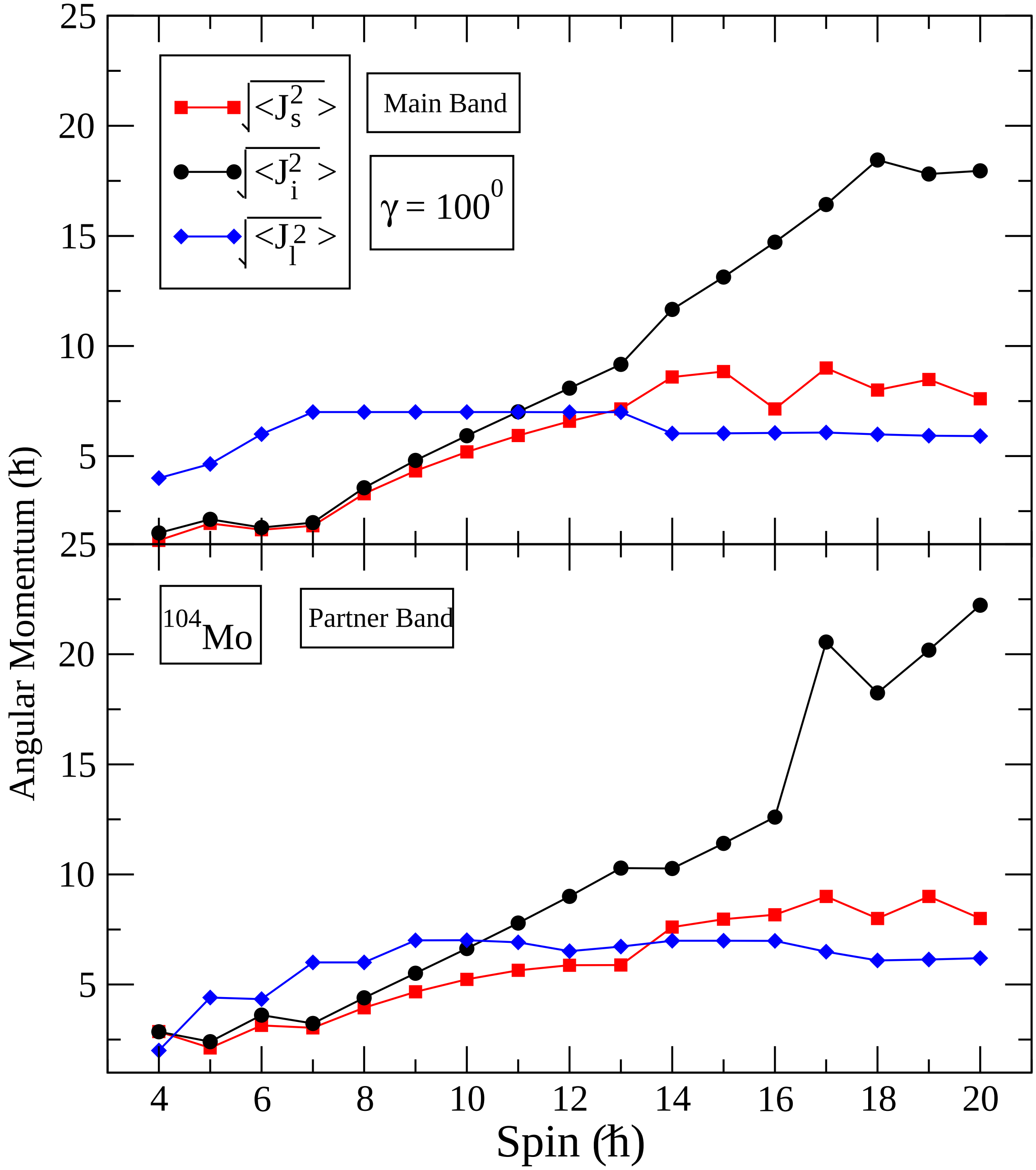

Figure 5.18: The expectation values of the squared angular momentum components for the main band (B4) and partner band (B5) for the total nucleus in ^{104}Mo. The value $\gamma = 100^{\circ}$ was used in order to mitigate small errors caused by the truncation of the configuration space in the TSPM code. The change $\gamma = 20^{\circ} \rightarrow 100^{\circ}$ only inter changes the intrinsic order of the axes in the code.

To specify this observation, the expectation values of the square of the components of total angular momentum have been calculated, which are obtained as follows

$$\begin{aligned}&\left\langle IM|J_i^2|IM\right\rangle \\ &= \sum_{KkKk'K''} f_{Kk'} f_{Kk'} \left\langle IK''|J_i^2|IK\right\rangle N_{K''kK'k'}.\end{aligned} \tag{5.5}$$

The sum runs over K, the projections of the total angular momentum and k, the label of the quasiparticle configurations. The coefficients f_{Kk} are the weights of the projected quasiparticle configurations, which form the non-orthogonal basis of the TPSM, $N_{K''kK'k'}$ are the norm-overlaps between the basis states, and $\left\langle IK''|J_i^2|IK\right\rangle$ are the standard matrix elements between states of good angular momentum [99].

In Fig. 5.18, the three components of the angular momentum are different from zero, which indicates a chiral geometry. The three components are about the same for both the main (band 4) and the partner band (band 5), which indicates that they, respectively, represent the even or odd linear combinations of the left- and right-handed versions of the structure illustrated in Fig. 5.18. For both chiral doublet bands, the collective core angular momentum mainly aligns along the intermediate axis (i-axis), because it has the largest moment of inertia.

5.2.5 PES Calculations

The configuration-constrained potential-energy surface (PES) method [100] is employed with a nonaxial deformed Woods-Saxon potential [101] with universal parameters to generate single-particle levels. The Lipkin-Nogami method [102] is employed to avoid the spurious transition encountered in the BCS approach. The total energy of a nucleus can be decomposed into a macroscopic part obtained from the standard liquid-drop model and a microscopic part computed with the shell-correction approach including blocking effects.

The deformation, excitation energy, and pairing property of a given state are determined by minimizing the obtained PES.

The calculated contours of different configurations in ^{104,106}Mo are shown in figures: 5.19, 5.20, 5.21, 5.22, 5.23 and 5.24. Table 5.5, shows the detailed deformations of each configuration. These calculations can help identify the configurations of the side bands in ^{104,106}Mo.

From the calculations, the best guess for the configuration of band 6 in ^{104}Mo is ν 3/2$^+$[411] $\otimes$ 5/2$^-$[532]. The calculated bandhead level is 1812 keV without triaxial deformation compared to the 1790 keV experimental level. Band 7 in ^{104}Mo could be the odd-spin branch of the same configuration. However, the calculation also has a 5$^-$ ν 5/2$^+$[413] $\otimes$ 5/2$^-$[532] configuration at 2326 keV, but it is less likely to be band 7 because the calculated energy is about 500 keV above the experimental one. The calculation does not have any 6$^+$ configurations, thus, band 8 is proposed to be a $\gamma\gamma\gamma$ band.

In ^{106}Mo, the calculation does not have 2$^+$ configuration below 2 MeV, thus, band 9 could be the β band where the 0$^+$ state is not clearly observed. The calculated 2$^+$ ν 3/2$^+$[411] $\otimes$ 1/2$^+$[411] configuration is located at 2299 keV. For band 10, there are no calculated levels very close to the experimental bandhead. The possible configurations for band 10 are 3$^-$ ν 1/2$^+$[411] $\otimes$ 5/2$^-$[532] (2140 keV in calculation) and 3$^+$ ν 1/2$^+$[411] $\otimes$ 5/2$^+$[413] (2305 keV in calculation). Band 6 and band 8 both have a 4$^-$ bandhead. One of them could be the ν 3/2$^+$[411] $\otimes$ 5/2$^-$[532] configuration according to the calculations. Band 7 could be the odd spin branch of band 6 or 5$^-$ ν 5/2$^+$[413] $\otimes$ 5/2$^-$[532], 5$^-$ π 5/2$^+$[422] $\otimes$ 5/2$^-$[303], 5$^+$ ν 5/2$^+$[402] $\otimes$ 5/2$^+$[413] or 5$^-$ ν 5/2$^+$[402] $\otimes$ 5/2$^-$[532] configuration. More theoretical work is needed to understand the band 6 to 10 structures and configurations.

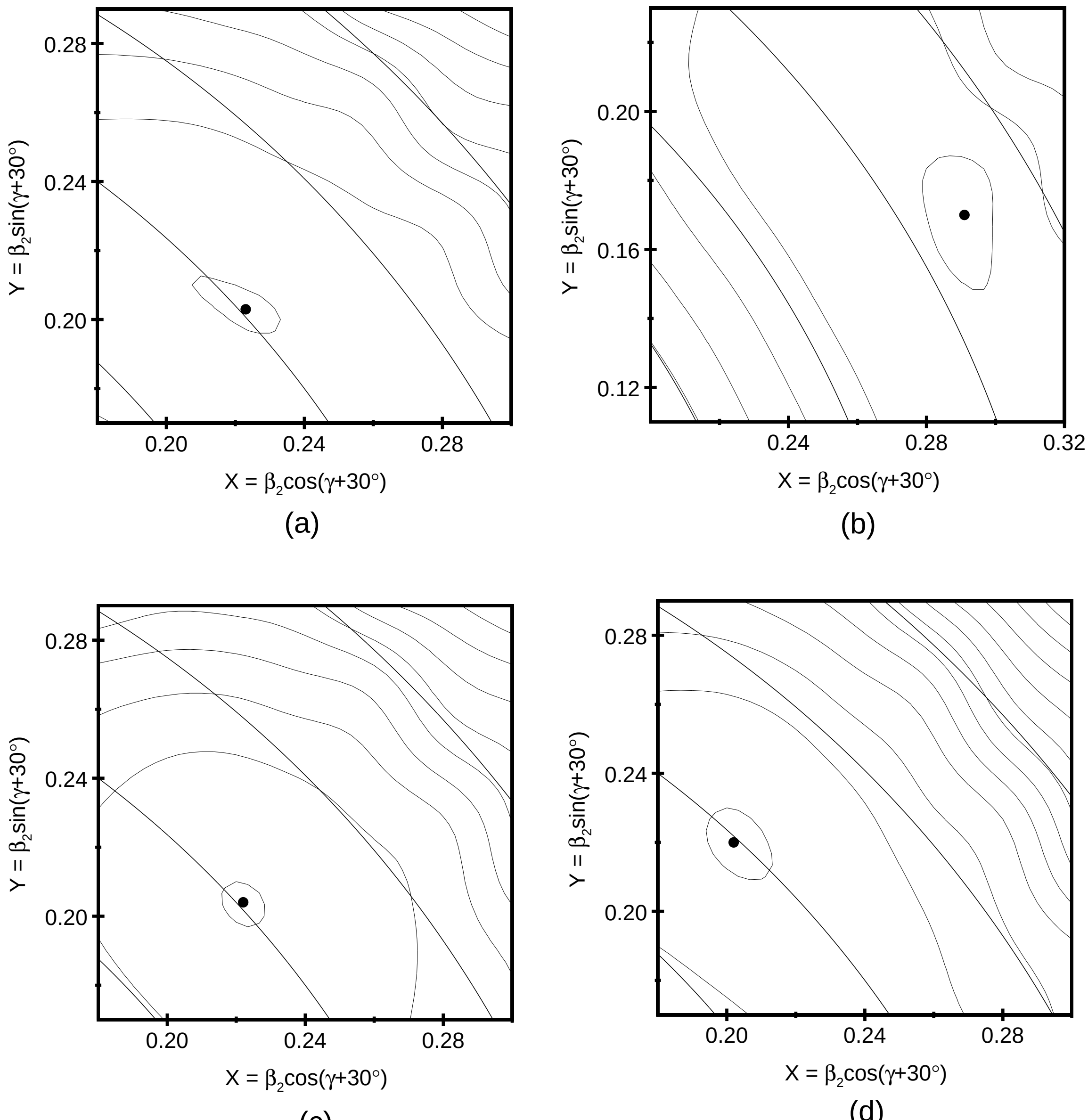

Figure 5.19: PES calculations for the (a) ground state, (b) ν 3/2$^+$[411] $\otimes$ 5/2$^-$[532], (c) ν 3/2$^+$[411] $\otimes$ 5/2$^+$[413] and (d) ν 3/2$^-$[541] $\otimes$ 5/2$^-$[532] configurations in ^{104}Mo.

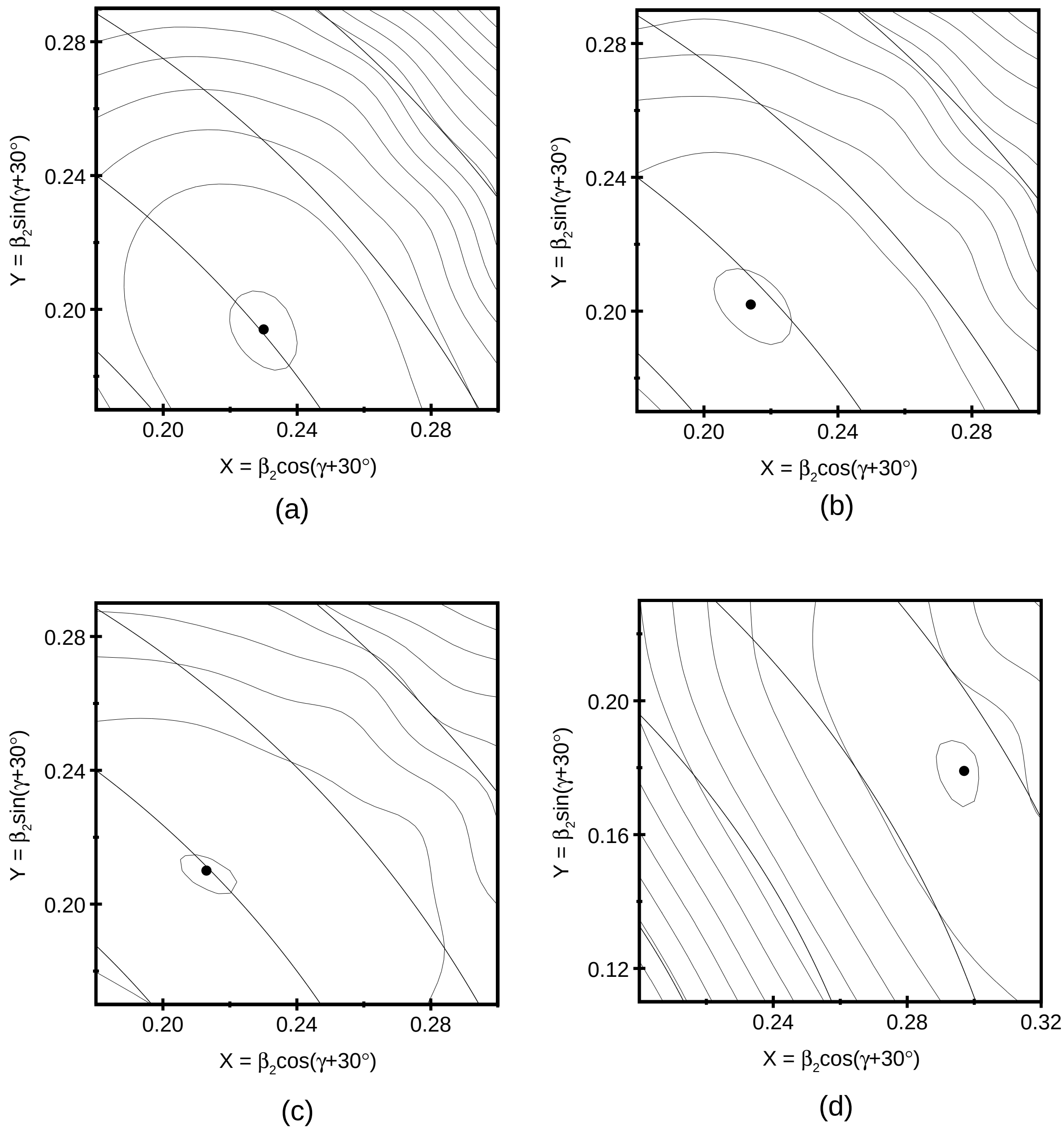

Figure 5.20: PES calculations for the (a) π $3/2^{+}[301] \otimes 5/2^{-}[303]$, (b) ν $3/2^{+}[411] \otimes 3/2^{-}[541]$, (c) ν $5/2^{+}[413] \otimes 5/2^{-}[532]$ and (d) π $1/2^{+}[431] \otimes 3/2^{-}[301]$ configurations in ^{104}Mo.

Table 5.5: Variously lowly excited quasiparticle states in ^{104}Mo and ^{106}Mo from the PES calculations.

Nuclei	Label	Configuration	β_2	$\gamma(^\circ)$	β_4	E_{exc} (keV)
^{104}Mo	Fig.5.19(a)	g.s.	0.302	12	0.012	0
	Fig.5.19(b)	ν $3/2^+[411] \otimes 5/2^-[532]$	0.337	0	0.021	1812
	Fig.5.19(c)	ν $3/2^+[411] \otimes 5/2^+[413]$	0.301	12	0.012	2133
	Fig.5.19(d)	ν $3/2^-[541] \otimes 5/2^-[532]$	0.299	17	0.007	2142
	Fig.5.20(a)	π $3/2^+[301] \otimes 5/2^-[303]$	0.301	10	0.012	2261
	Fig.5.20(b)	ν $3/2^+[411] \otimes 3/2^-[541]$	0.295	13	0.008	2322
	Fig.5.20(c)	ν $5/2^+[413] \otimes 5/2^-[532]$	0.299	14	0.007	2326
	Fig.5.20(d)	π $1/2^+[431] \otimes 3/2^-[301]$	0.347	1	0.019	2413
^{106}Mo	Fig.5.21(a)	g.s.	0.309	16	0.004	0
	Fig.5.21(b)	ν $5/2^+[413] \otimes 5/2^-[532]$	0.316	16	0.005	1815
	Fig.5.21(c)	ν $1/2^+[411] \otimes 5/2^-[532]$	0.318	0	0.002	2140
	Fig.5.21(d)	ν $3/2^+[411] \otimes 5/2^+[413]$	0.337	7	0.008	2152
	Fig.5.22(a)	π $3/2^-[301] \otimes 5/2^-[303]$	0.306	12	0.003	2281
	Fig.5.22(b)	ν $5/2^-[532] \otimes 3/2^-[541]$	0.287	23	-0.006	2294
	Fig.5.22(c)	ν $3/2^+[411] \otimes 1/2^+[411]$	0.334	0	0.006	2299
	Fig.5.22(d)	ν $1/2^+[411] \otimes 5/2^+[413]$	0.303	0	-0.003	2305
	Fig.5.23(a)	ν $3/2^+[411] \otimes 5/2^-[532]$	0.319	7	0.006	2308
	Fig.5.23(b)	π $5/2^+[422] \otimes 5/2^-[303]$	0.283	22	0.003	2343
	Fig.5.23(c)	ν $3/2^-[541] \otimes 5/2^+[413]$	0.294	24	-0.002	2356
	Fig.5.23(d)	ν $5/2^+[402] \otimes 5/2^+[413]$	0.282	28	0.003	2358
	Fig.5.24(a)	ν $5/2^+[402] \otimes 5/2^-[532]$	0.294	27	0.007	2423
	Fig.5.24(b)	π $1/2^+[431] \otimes 3/2^-[301]$	0.355	9	0.007	2482

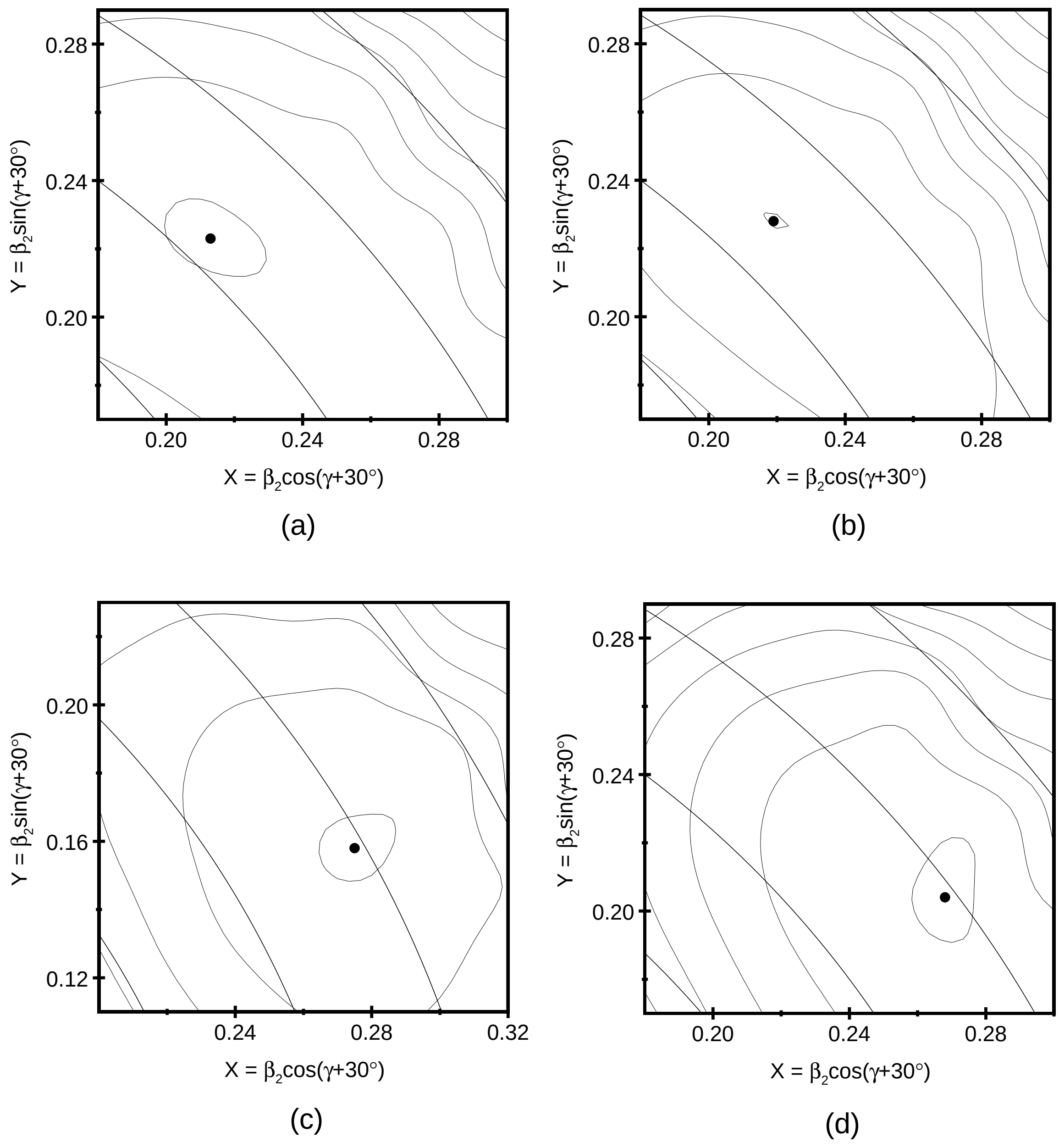

Figure 5.21: PES calculations for the (a) ground state, (b) ν 5/2$^+$[413] $\otimes$ 5/2$^-$[532], (c) ν 1/2$^+$[411] $\otimes$ 5/2$^-$[532] and (d) ν 3/2$^+$[411] $\otimes$ 5/2$^+$[413] configurations in ^{106}Mo.

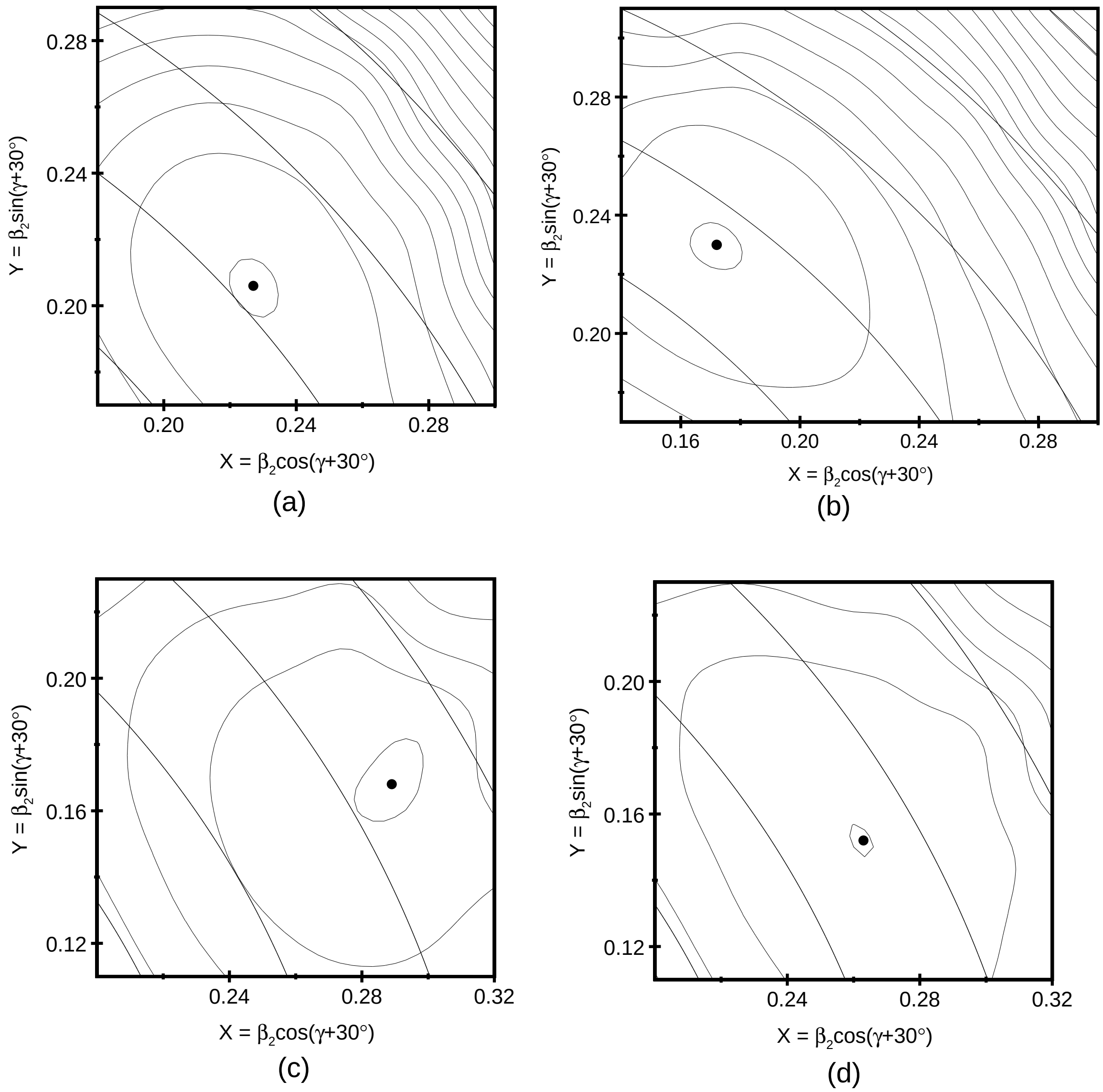

Figure 5.22: PES calculations for the (a) π $3/2^{-}[301] \otimes 5/2^{-}[303]$, (b) ν $5/2^{-}[532] \otimes 3/2^{-}[541]$, (c) ν $3/2^{+}[411] \otimes 1/2^{+}[411]$ and (d) ν $1/2^{+}[411] \otimes 5/2^{+}[413]$ configurations in ^{106}Mo.

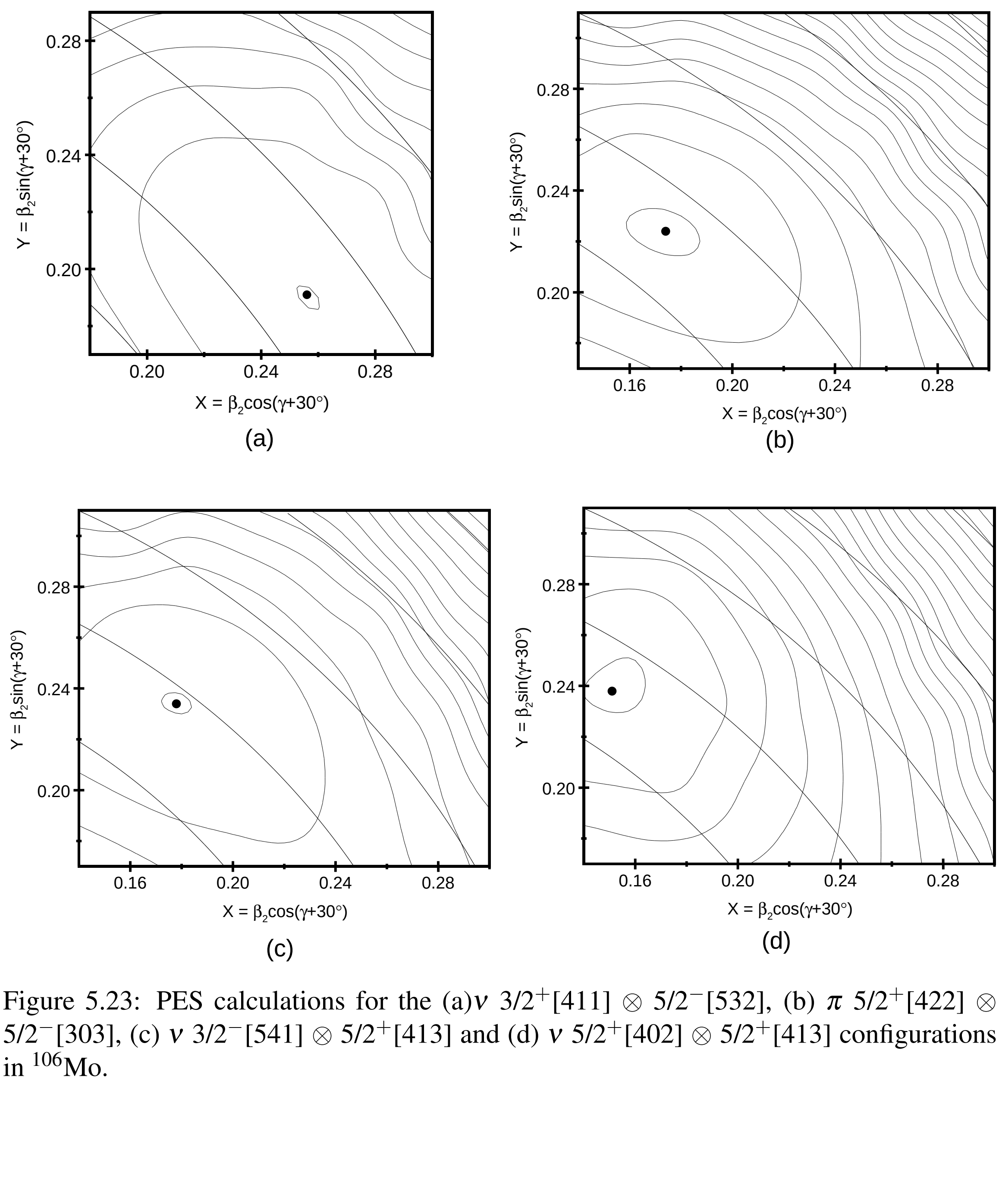

Figure 5.23: PES calculations for the (a)ν 3/2$^+$[411] $\otimes$ 5/2$^-$[532], (b) π 5/2$^+$[422] $\otimes$ 5/2$^-$[303], (c) ν 3/2$^-$[541] $\otimes$ 5/2$^+$[413] and (d) ν 5/2$^+$[402] $\otimes$ 5/2$^+$[413] configurations in ^{106}Mo.

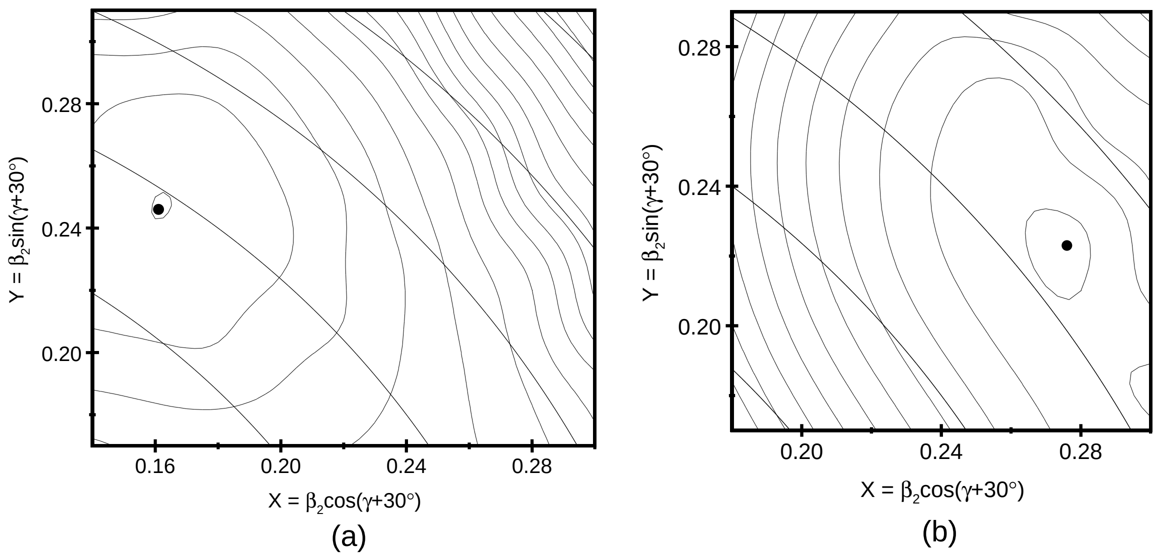

Figure 5.24: PES calculations for the (a)ν 5/2$^+$[402] $\otimes$ 5/2$^-$[532] and (b) π 1/2$^+$[431] $\otimes$ 3/2$^-$[301] configurations in ^{106}Mo.

5.3 Conclusion

In summary, high spin states of neutron-rich ^{104,106}Mo have been reinvestigated by analyzing the γ-rays in spontaneous fission of ^{252}Cf with Gammasphere. Both $\gamma-\gamma-\gamma$ and $\gamma-\gamma-\gamma-\gamma$ coincidence data were analyzed. New levels and transitions have been identified in both isotopes. A new ΔI=1 band has been discovered in ^{104}Mo with a tentative 5^- bandhead, and is proposed to form a class of chiral vibrational doublets with another 4^- band previously found. Angualar correlation measurements have been performed to determine the spins and parities in both isotopes. Bands (4) and (5) in these nuclei are proposed as soft chiral vibrational doublet bands. These doublet rotational bands in ^{104}Mo show similar behavior to those in ^{106}Mo but exhibit smaller separation energies. The levels of the 4^- and 5^- chiral doublets in ^{106}Mo have bee reassigned The theoretical calculations support the assignments of these newly observed bands as soft chiral doublet bands built on the $h_{11/2}$ quasineutron and a pseudo spin pair of $(d_{5/2}g_{7/2})$ quasineutrons. TPSM calculations have been performed for the chiral doublet bands in ^{104,106}Mo. The results show reasonably good agreement with the experiement data. PES calculations have been performed, however, more theoretical work is needed to understand the band 6 to 10 structures and configurations in ^{106}Mo.

Chapter 6

Anomalous Neutron Yields Confirmed for Ba-Mo and Newly Observed for Ce-Zr from Spontaneous Fission of ^{252}Cf

This chapter is adapted from "Anomalous Neutron Yields Confirmed for Ba-Mo and Newly Observed for Ce-Zr from Spontaneous Fission of ^{252}Cf" published in Physics Review C and has been reproduced with the permission of the publisher and my co-authors "Thibeault, A. H. and Richards, T. H. and Wang, E. H. and Hamilton, J. H. and Zachary, C. J. and Eldridge, J. M. and Ramayya, A. V. and Luo, Y. X. and Rasmussen, J. O. and Ter-Akopian, G. M. and Oganessian, Yu. Ts. and Zhu, S. J." *Published in Physics Review C*

6.1 Introduction

As discussed in section 2.2, the process of spontaneous fission involves the formation of primary fission fragments in an unstable state. These fragments evaporate neutrons to become excited secondary fission fragments that can be identified by studying their emitted γ-rays. The number of neutrons emitted is often referred to as the "neutron channel" number (N_c) and is given in equation 6.1. The distribution of the final products is directly connected to the number of neutrons evaporated. The number of prompt neutrons emitted in a binary fission event can be determined by finding the mass number of the fragments produced in an event. For example, if the fission fragments of ^{252}Cf are determined by some method to be ^{144}Ba and ^{103}Mo, then five neutrons must have been emitted. This can be computed from the nuclear masses of ^{252}Cf and the daughter isotopes produced by:

$$N_c = 252 - (A_1 + A_2). \tag{6.1}$$

Where A_1 and A_2 are the mass numbers of the two daughter isotopes.

The number of neutrons evaporated depends on the excitation energy of the nucleus. Early studies measured the distribution of neutrons emitted in the SF of ^{252}Cf for different charge splits and found a Gaussian shape centered between 3-4 neutrons in Ref. [103] and averaging ≈ 3.7 according to Ref. [3]. More recent studies have extended this work to measure yields of specific fission pairs, related to the advance in resolving power of detector arrays and coincidence gating techniques. The species of fission fragment is identified by detecting its characteristic γ-ray transitions.

With this technique, yields of individual correlated pairs in barium (Z = 56) and molybdenum (Z = 42) binary fission were observed to undergo fission splits via an extra "hot fission mode" (also called second mode) [3]. In this mode, it has been observed that the Ba-Mo fragment pair emits high neutron multiplicities of 7 to 10 neutrons in spontaneous fission of ^{252}Cf [3, 16, 17]. With our high statistical data, we further re-investigated the existence of the second hot fission mode.

6.2 Previous ^{252}Cf Neutron Studies

Before 1994, the only measurements of neutron multiplicities came from neutron detector experiments. These were able to measure total yields and unfolded the data with some assumptions about the expected shape of the distribution. The broad result was that the neutron multiplicity curve follows a Gaussian distribution for 1-8 neutrons, centered at 3.7 neutrons (see Ref. [103]). Some more detailed measurements of the distribution for different mass regions were also performed, but there was no way to identify the exact species of the fragments involved in the fission.

The first study to isolate individual fission fragment pairs was done in 1994 by Ter-Akopian et al. [3]. By using the γ-γ-γ coincident data, the fission fragments created in the SF could be directly identified. With the atomic mass of each daughter nucleus, the missing number of neutrons can be inferred using Eqn. 6.1. It was found that the distributions of neutron multiplicities follow a Gaussian shape for several different individual charge-split fission partners as well as the overall ^{252}Cf yield. This is show in Fig. 6.1.

However, in one fission pairing, the distribution was observed not to follow a single Gaussian shape. In the splitting of ^{252}Cf into Ba and Mo isotopes, additional yields were measured associated with more neutrons being evaporated. Yields were found with up to 10 neutrons evaporated, where the other pairs extend only to 8 neutrons evaporated. This can be described with a two Gaussian fit, one centered between 3-4 neutrons and the second around 8 neutrons, as seen in Fig. 6.2.

This result was a very surprising finding, as this Ba-Mo split was the only fission pair exhibiting this dual distribution. Other theorists raised skepticism, since the hot fission mode had only been observed in Ba-Mo fragment pairs of ^{252}Cf and not in spontaneous fission of ^{248}Cm [21]. However, this private communication [21] has never been published.

Furthermore, some earlier analysis in spontaneous fission of ^{252}Cf did not confirm the second hot mode [5] without reporting the 9 and 10 channel yields (see later discussion), while others did show some irregularity around the eight-neutron channel [4, 22, 104, 24]. The neutron multiplicity curve from Ref. [4] is shown in Fig. 6.3, where the second Gaussian contribution is much reduced. Because of the importance of understanding this extra hot fission mode, pairs of Ba-Mo, Ce-Zr, Te-Pd, Xe-Ru and Nd-Sr have been studied with improved precision using γ-γ-γ-γ as well as γ-γ-γ coincidence data and the latest level structures of these nuclei. Also, relative intensities of transitions in these nuclei made available through our work likewise improved the accuracy of the analysis. In all cases, careful attention was given to transitions of the same energies in multiple isotopes.

6.3 Hot Fission Mode

The theoretical interpretation of the two-Gaussian distribution is that a second mode of fission is involved in the Ba-Mo split. Multiple fission modes for a single nucleus have been theorized based on asymmetric deformation calculations in Ref. [105]. In heavy nuclei

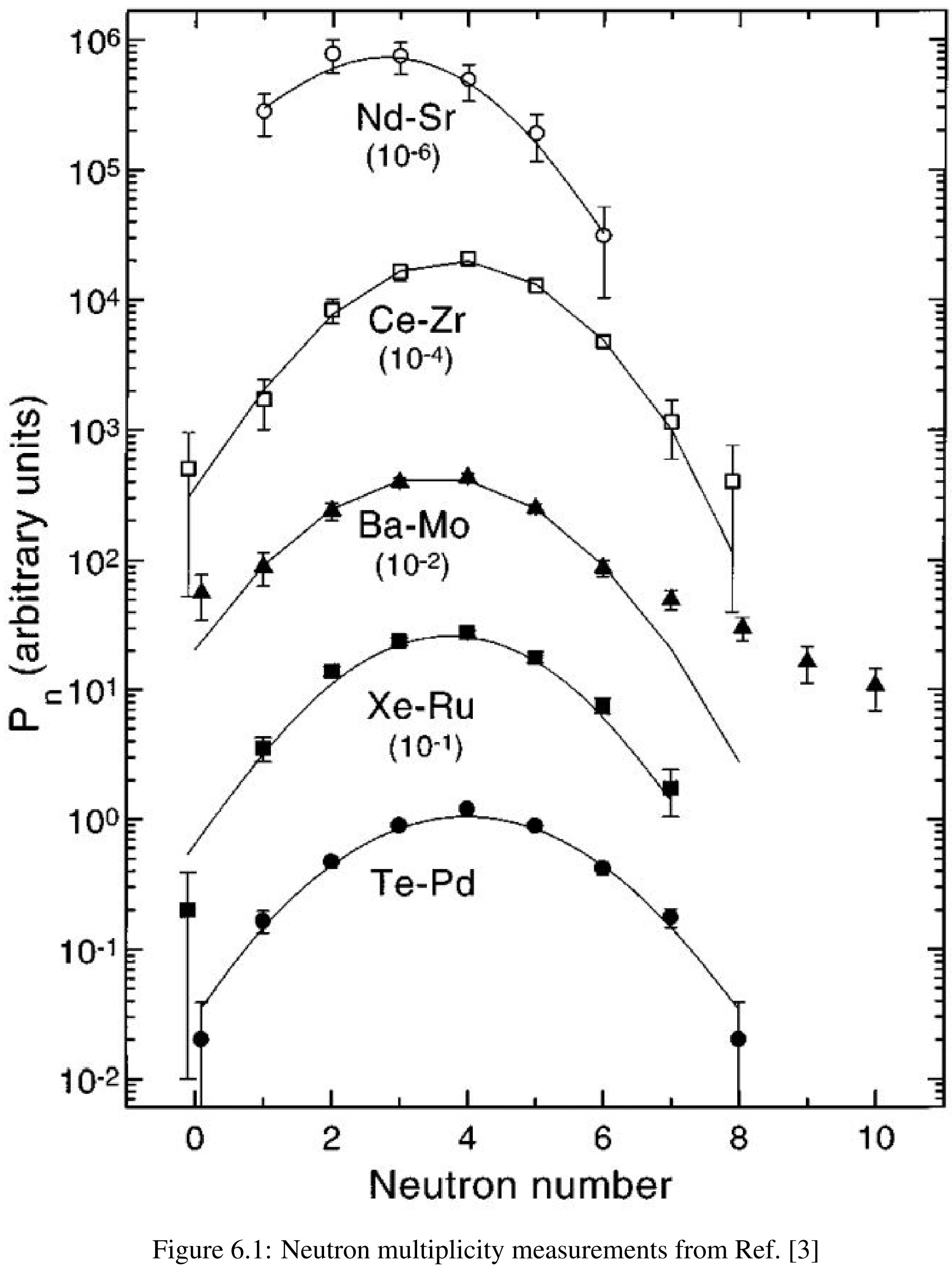

Figure 6.1: Neutron multiplicity measurements from Ref. [3]

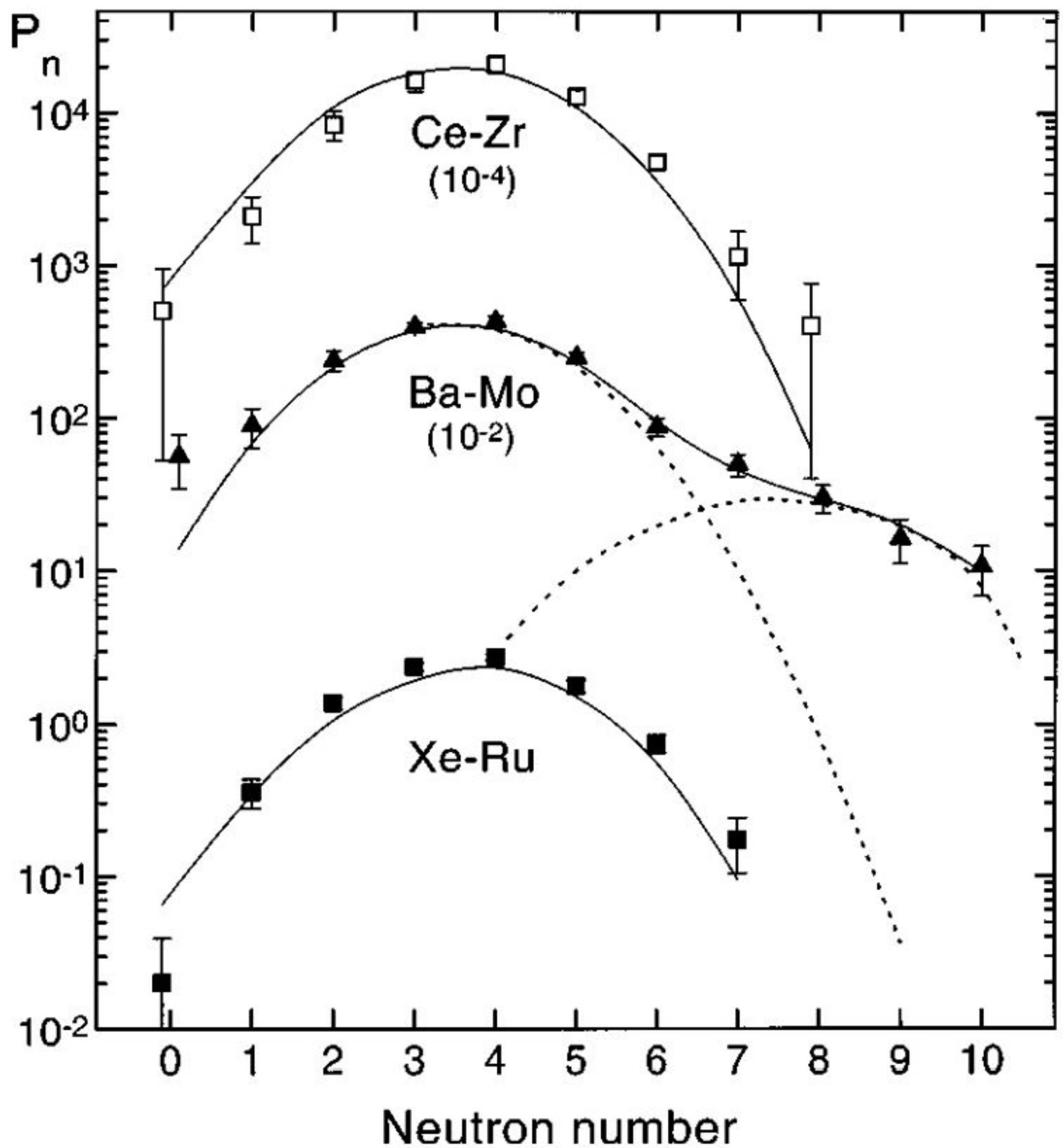

Figure 6.2: Neutron multiplicity measurements from Ref. [3]

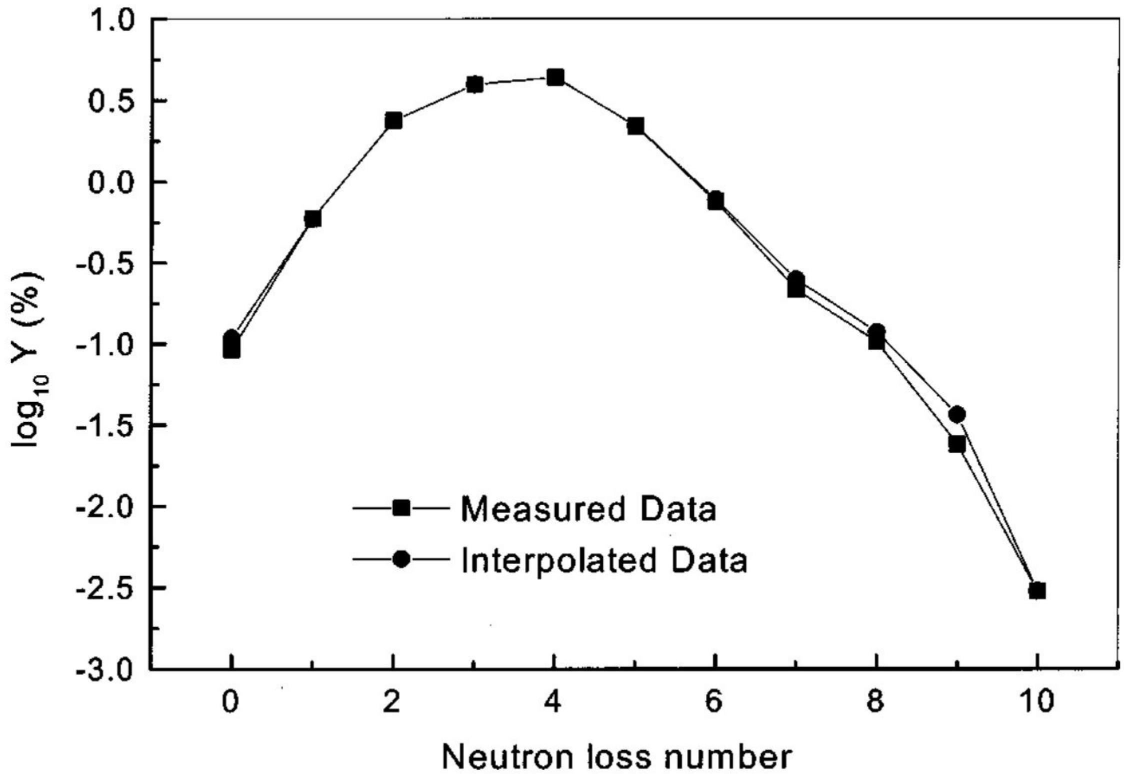

Figure 6.3: Neutron multiplicity measurements from Ref. [4]

such as ^{258}Fm, ^{258}No, and ^{259,260}Md, a bimodal energy distribution has been observed in Ref. [106]. This was characterized by a large difference in the average total kinetic energy $\langle$TKE$\rangle$ between the two distribution groups with the new mode having a higher $\langle$TKE$\rangle$.

Measurements of the fission fragment energies from SF of ^{252}Cf by Ter-Akopian et al. [3] resulted in an excellent fit that yielded two such fission modes. One mode had $\langle$TKE$\rangle$ = 189 MeV while the other mode had $\langle$TKE$\rangle$ = 153 MeV. The first mode corresponds to the familiar fission mode for ^{252}Cf. The second mode corresponds to events with a larger number of neutrons emitted, with an intensity for the second mode $\approx 7\%$ of the first mode [3]. This excess internal energy indicated that one of ^{144,145,146}Ba had a hyperdeformed shape ($\beta_2 \approx 1.0$) at scission. In simple terms, the second mode of fission is theorized to represent a fission pathway that results in a much lower kinetic energy taken up by the fragments. This in turn leads to larger internal excitation energy. The fragments

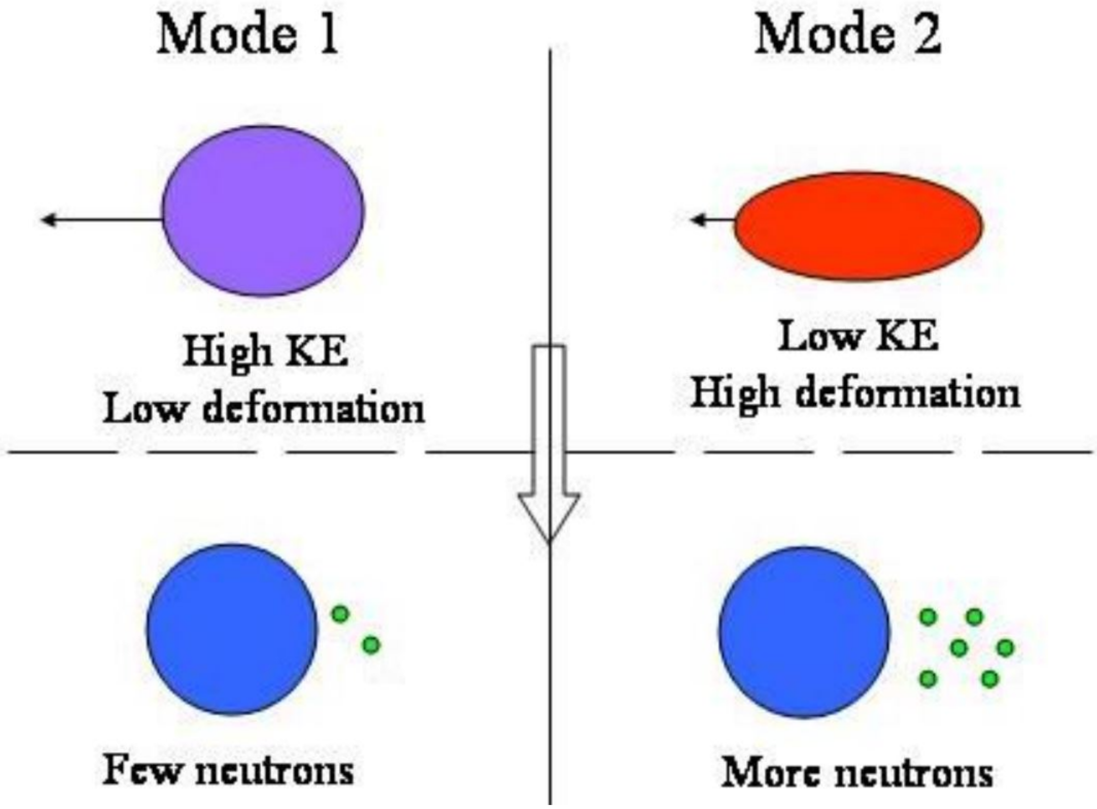

Figure 6.4: Schematics of two coexisting fission modes in ^{252}Cf

that are created with more excitation energy evaporate more neutrons from their deformed shapes. A schematic of this process is shown in Fig. 6.4

6.4 Method of Data Analysis

Quadruple (γ-γ-γ-γ) as well as triple (γ-γ-γ) coincidence data were analyzed to extract the relative yields of correlated fragment pairs in spontaneous fission of ^{252}Cf. Of particular interest in this experiment are the γ-ray transitions to the ground state. Some isotopes have a single ground state γ-ray transition, but others have multiple ones. The ground state γ-ray transition is generally the highest intensity γ-ray emitted by an isotope, and all daughter nuclei will emit this γ-ray, excluding the extremely unlikely case they were produced in the ground state during the fission process. By measuring the intensity of ground state γ-rays,

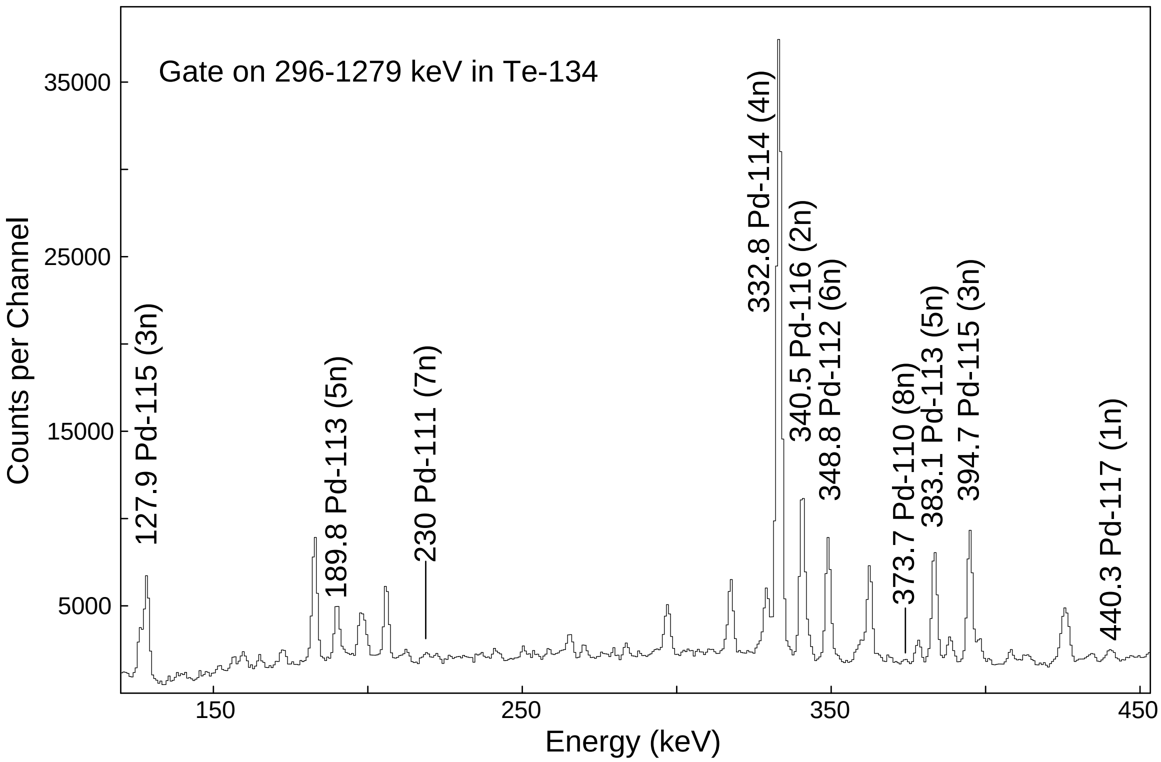

Figure 6.5: Gate on the 296 and 1279 keV transitions in ^{134}Te showing ground state transitions from partner fission fragments of Pd in ^{252}Cf.

it can be deduced how likely specific isotopes of fission partner isotopes are to be produced in the spontaneous fission of ^{252}Cf.

In order to find peaks for the yield computation, a double or triple gate was set on the most intense coincident γ-rays in a given nucleus (usually the $2^+ \rightarrow 0^+$ and $4^+ \rightarrow 2^+$ transitions in case of an even-even product). On the generated coincidence spectrum, the transitions in the partner fragments were clearly identified as shown in Fig. 6.5. The intensities of the γ-ray transitions in the partners (usually the $2^+ \rightarrow 0^+$ in case of even-even nuclei) were corrected for the detector efficiencies and internal conversion coefficients (ICC) of the γ-rays involved in the selection and used along with other transitions feeding into the ground state to extract the relative yields for the considered partitions. In the case of odd nuclei, all the known transitions populating the ground state were summed proportionally according to their intensities.

If the ground state γ-ray is inconvenient to measure, it is also possible to use a higher transition to make this calculation, as long as its intensity relative to the ground state transition is known. The relative intensities of all transitions feeding the ground states of the isotopes analyzed in this study were determined based on new levels schemes with new ground state transitions (especially in odd-even nuclei) [107, 108, 109, 110, 111, 112, 113, 114, 115, 116] to produce a new set of absolute yields. Some of the γ-rays in the newly published level schemes are not clearly observed in our data such as ^{140}Te [117]. Additionally, if there is a presence of an isomeric state in the level scheme structure of a given nucleus, the transitions populating into that isomeric state were considered by adding the contribution of those transitions populating that state according to its time scale. This was done to avoid underestimating the yields. Specific examples will be given in the discussion section.

A two-dimensional matrix was created from the initial data by selecting the γ-ray coincidences occurring within 1 μs time window. The peaks observed in this two-dimensional spectrum arise from the coincidences between the γ-ray emitted promptly by both complementary fission fragments of different fragment pairs. The new results confirm a second hot mode in Ba-Mo pairs with an intensity of $\sim$1.5(4)% and shows evidence for a comparable second hot mode in Ce-Zr pairs with an intensity of $\sim$1.0(3)%. These result are compared with other results [5, 4, 22, 24, 104].

6.5 Experimental Results and Discussion

Fission spectra are very complex and this type of analysis is difficult and prone to errors caused by random coincidences and background. As such, we found some peaks unusable because of contamination or similar transition energies found in other isotopes. Cross-checks by gating on a series of isotopes as well as gating on their fission partners have been done to determine possible contamination and the accuracy of the current result. In addition, to measure yields in these cases, we used peaks found in higher transitions and scaled them appropriately. For example, Table 6.1 contains this information for the Sr-Nd pair. In order to calculate the scaling factor, we set a clean gate with no contamination

Table 6.1: A list of isotopes whose ground state transition energies were difficult to measure (because of similar ground state energies or not clearly observed in our data) and what energy transition we measured instead in Nd-Sr fragment pairs. The scaling factor is the relative intensity of the measured transition to the ground state transition; we divided the yield of the transition by this factor to correct it.

Isotope	Gate	Ground state (keV)	Measured (keV)	Scaling factor
^{92}Sr	^{155}Nd	814.6	859	0.46
^{94}Sr	^{150}Nd	836.7	1089.1	0.23
^{96}Sr	^{155}Nd	814.8	977.5	0.49

on energy transitions of other isotopes and measured the intensities of the ground state transitions and of the higher transitions. By taking the ratio of these intensities, we compute the scaling factor needed. The results for all the relative yield curves are shown in Fig. 6.6. All of the fission partner pairs have an average neutron multiplicity of ≈3-4 and the FWHM is about 3 as seen in Table 6.2.

Table 6.2: A list of the average neutron multiplicities ($\bar{\nu}$) and the full width at half maximum (FWHM) for each pair shown in Fig. 6.6. The average neutron multiplicity distributions are very close to the accepted values of 3.8 for the spontaneous fission of ^{252}Cf.

	Ba-Mo	Ce-Zr	Te-Pd	Nd-Sr	Xe-Ru
Ave ($\bar{\nu}$)	3.57	3.62	3.71	3.84	3.81
FWHM	3.1	3.1	2.9	3.1	3.1

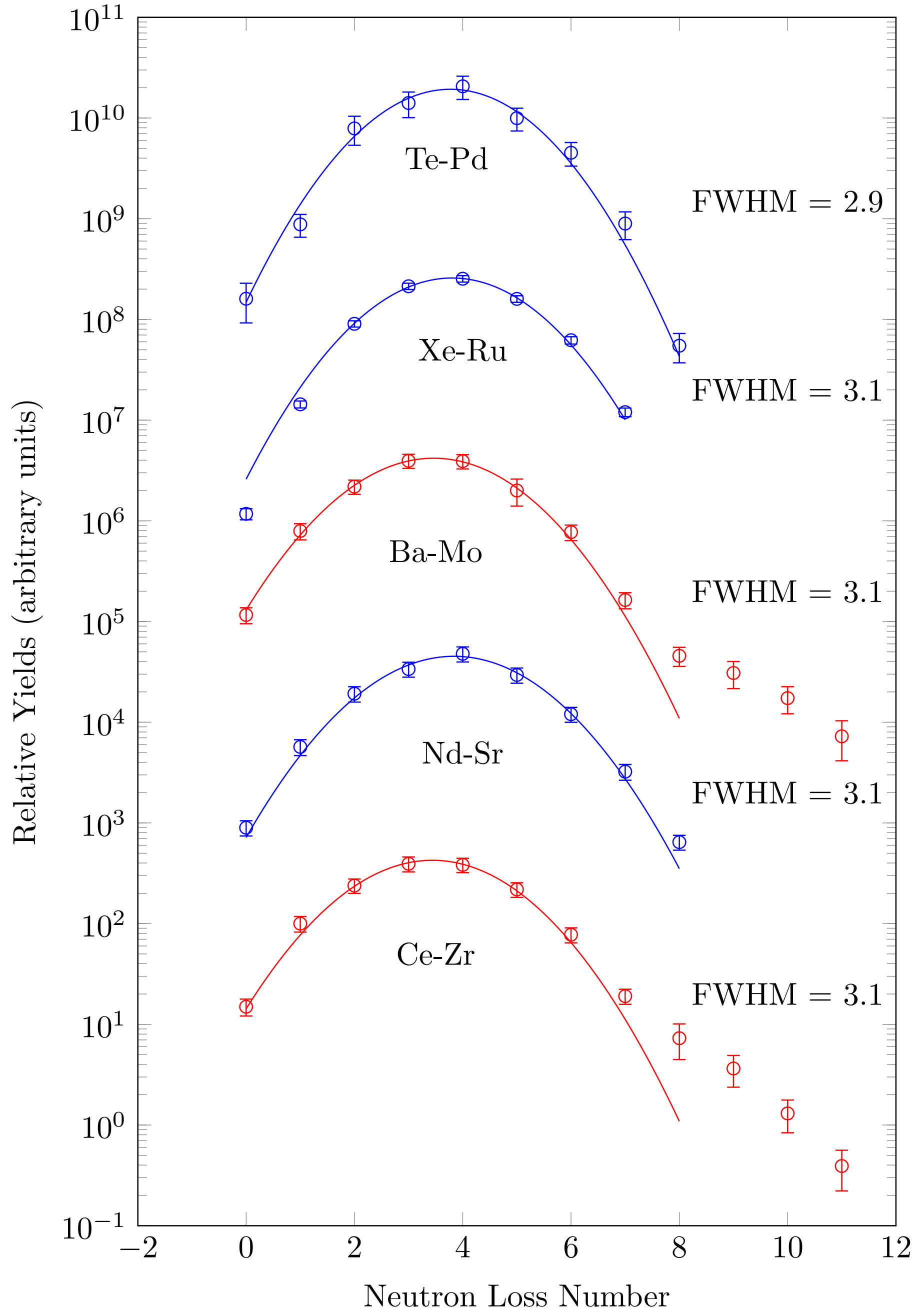

Figure 6.6: The experimental Ba-Mo, Ce-Zr, Te-Pd and Nd-Sr yield curves from the present analysis are shown above. There is no evidence for the 9, 10 and 11 neutron channels in pairs other than Ba-Mo and the newly observed Ce-Zr. A smooth Gaussian fit to the 0-8 neutron channels in Nd-Sr, Xe-Ru, Te-Pd, Ce-Zr and Ba-Mo is shown. The full width at half maximum (FWHM) was also calculated for each of the yields as shown in this figure.

6.5.1 Xe-Ru Yields

In ref. [3], the yield matrix for the $^{106-112}$Ru and $^{134,136-140,142}$Xe pairs were measured. In comparison, this thesis measured the all isotopic chain of the $^{105-114}$Ru and $^{134-144}$Xe pairs as shown in Table 6.3. Since the previous work [3] did not include all the Xe-Ru isotopes, the normalization was not accurate. Technical details are included here. In ^{105}Ru, only the 365 keV transition populating the 209 keV isomer is used to measure the yield. The 3/2^{+} ground state band transitions are not observed in the present work so it is not included. In ^{107}Ru, the 103, 142, 199, 428 keV g.s. transitions are used to measure the yield. Some inconsistency is observed in the intensity ratios of the 199 and 428 keV transitions in different gates. In ^{109}Ru, the 96, 131, 138, 185, 197, 332, 408 keV g.s. transitions and the 69, 122, 128, 187 keV transitions populating the 69 keV isomer are used to measure the yield. The 69 keV g.s. isomeric transition is E2 with large internal conversion thus, most of the 69 keV peak is another 69 keV transition populating this 69 keV 0.5 μs isomer. In ^{111}Ru, the 150, 185, 254, 279, 356 g.s. transitions and 175 keV transition populating the 10 keV level and the 146, 267 keV transitions populating the 39 keV level are used to measure the yield. Note that, the 185 keV transition in ^{111}Ru is weak while another 185 keV transition in ^{109}Ru is strong. Thus, the 185 one in ^{111}Ru can only be deduced from the intensity ratios with the 146 and 175 keV transitions depopulating the same 185 keV level. In ^{113}Ru, the 98 keV g.s. transition and the 113, 260 keV transitions populating the 7/2^{-} isomer are used to measure the yield. The 98 keV one was not reported in fission experiment but it is strong in the partner gate.

In the present work, $^{136-141}$Xe and $^{108-112}$Ru are strongly populated. The ^{108,110}Ru g.s. transitions are very close in energy. The ^{136}Xe has a 3 μs isomer. Therefore, the independent yield of ^{138}Xe is used to normalize to the absolute yields. The independent yields of ^{108,110}Ru obtained in the present work are all higher than those from Ref. [118]. The fitted Gaussian for neutron is centered at 3.8 with a FWHM = 3.1 as shown in Fig. 6.6. This result is constant with the Te-Pd and Nd-Sr yields.

Table 6.3: New yield matrix for xenon and ruthenium from the spontaneous fission of ^{252}Cf.

Yield	^{134}Xe	^{135}Xe	^{136}Xe	^{137}Xe	^{138}Xe	^{139}Xe	^{140}Xe	^{141}Xe	^{142}Xe	^{143}Xe	^{144}Xe
^{105}Ru									<0.002		
^{106}Ru						0.005(1)	0.037(6)	0.055(9)	0.036(6)	0.014(2)	0.004(1)
^{107}Ru					0.012(3)	0.051(13)	0.139(23)	0.126(21)	0.076(13)	0.010(2)	
^{108}Ru				0.046(7)	0.223(37)	0.303(50)	0.456(76)	0.330(55)	0.066(11)	0.010(3)	
^{109}Ru			0.049(8)	0.139(23)	0.566(90)	0.492(82)	0.440(73)	0.200(33)	0.020(3)		
^{110}Ru		0.007(2)	0.157(26)	0.303(49)	0.870(137)	0.532(88)	0.216(36)	0.043(8)	0.004(1)		
^{111}Ru		0.008(2)	0.205(32)	0.357(56)	0.518(82)	0.180(28)	0.040(6)				
^{112}Ru	0.007(1)	0.018(4)	0.178(28)	0.149(24)	0.183(29)	0.021(3)	<0.008				
^{113}Ru	0.009(3)	0.013(2)	0.065(10)	0.025(4)	0.004(1)						
^{114}Ru	0.008(2)	0.012(3)	0.022(5)	0.005(1)							

6.5.2 Te-Pd Yields

In ref. [3], the yield matrix for the ^{108,110,112,114,116}Pd and ^{132,134,136}Te pairs were measured. In comparison, this thesis measured the all isotopic chain of the $^{110-118}$Pd and $^{130-138}$Te pairs. Since the previous work [3] did not include all the Te-Pd isotopes, the normalization was not accurate. Technical details are included here. The present work did not observe transitions in ^{109}Pd. In ^{111}Pd, the 230 and 523 keV g.s. transitions and the 413 keV transition populating the $11/2^{-}$ isomer can be seen and was used to measure the yield of this nucleus. In ^{113}Pd, transitions directly populating the g.s. and the 81 keV (0.3 s) isomer were used to measure the yield. There are two 340 keV transitions in ^{115,116}Pd, respectively. The 340 keV transition in ^{115}Pd is weak and can be subtracted proportionally from the g.s. transitions when measuring the yield to get a clear 340 keV in ^{116}Pd. In ^{117}Pd, the 440 keV transition populating the 266 keV $11/2^{-}$ level was used to measure the yield.

In ^{130}Te, there are isomers at 2145 keV (110 ns) and 2664 keV (1.9 μs). However, transitions populating these isomers are very weak in present data and were not included to measure the yield. In ^{131}Te, the 833 keV transition populating the 182 keV $11/2^{-}$ isomer was used to measure the yield. Note that, a 93 ms isomer was reported at 1941 keV in [119], but no transitions were observed populating this isomer. Thus, we did not consider the contribution from this isomer. In ^{132}Te, there are isomers at 1774 keV (145 ns), 1924 keV (28 μs) and 2722 keV (3.7 μs). Transitions populating these isomers are very weak in the present data and thus, their contributions were not considered in the yield measurements. Contribution from the isomers in $^{133-135}$Te were included. There is a 606 keV g.s. transition in ^{136}Te and a 608 keV g.s. transition in ^{137}Te. These two transitions are close in energy and lie on the neutron scatter platform. Careful cross-checks have been made to separate these two transitions and make an accurate measurement.

The measured yield matrix for tellurium (Z = 52) and palladium (Z = 46) is shown Table 6.4. It displays the expected pattern where the highest yields are concentrated in the center of the matrix, along the 4 neutron channel diagonal, running from the bottom left to

Table 6.4: New yield matrix for tellurium and palladium from the spontaneous fission of ^{252}Cf.

Yield	^{110}Pd	^{111}Pd	^{112}Pd	^{113}Pd	^{114}Pd	^{115}Pd	^{116}Pd	^{117}Pd	^{118}Pd
^{130}Te							0.010(1)	0.0029(4)	0.017(2)
^{131}Te						0.05(1)	0.042(5)	0.006(1)	0.010(1)
^{132}Te				0.036(4)	0.06(1)	0.07(1)	0.19(2)	0.018(2)	0.016(2)
^{133}Te		0.0022(3)	0.016(3)	0.035(4)	0.14(2)	0.09(1)	0.15(2)	0.005(1)	0.008(1)
^{134}Te	0.0021(3)	0.015(2)	0.16(2)	0.33(4)	0.78(9)	0.28(3)	0.24(3)	0.007(1)	0.006(1)
^{135}Te	0.003(1)	0.017(2)	0.11(1)	0.20(2)	0.27(4)	0.05(1)	0.040(5)	0.0013(3)	
^{136}Te	0.021(3)	0.06(1)	0.29(4)	0.24(3)	0.22(4)				
^{137}Te	0.012(2)	0.020(3)	0.12(2)	0.06(1)	0.013(2)				
^{138}Te	0.014(2)	0.023(3)	0.035(4)		0.005(1)				

the top right corners. The yield matrix was normalized by using the normalization constant of ^{114}Pd in Wahl's table [118]. This pair has a lot of isomeric states and many of the level schemes are incomplete. Therefore, the yields are incomplete (see Fig. 6.6). The yields for the other studied element pairs in Fig. 6.6 display a similar pattern as expected. However, as seen in Fig. 6.7 (a), where the spectrum was gated on both the 373.7 and 574.5 keV transitions in ^{110}Pd, there is no evidence for the 9 and 10 neutron channel at 1150.6 keV in ^{133}Te and at 974.4 keV in ^{132}Te, respectively, for the Te-Pd pairs. Whereas, there is clear evidence of the 8 neutron channel at 1279.1 keV in ^{134}Te which fits nicely with the simple curve in Fig. 6.6.

6.5.3 Nd-Sr Yields

In ref. [3], only the ^{96,98}Sr and ^{150,152,154}Nd yield matrix was measured. In the present work, the matrix has been extended to $^{91-100}$Sr and $^{148-156}$Nd as shown in Table 6.5. The previous absolute yields were overestimated because the normalization did not include all the isotopic chains in Sr-Nd from ^{252}Cf SF.

In the Nd-Sr yields matrix in Table 6.5, we left most of the items in the ^{148}Nd and ^{149}Nd columns blank because those isotopes are very weakly populated in the spontaneous fission of ^{252}Cf, making it difficult to measure energy transitions of interest. Some similar energies, such as the ground state transitions of ^{100}Sr and ^{150}Nd (129.8 keV and 129.7 keV, respectively), are not distinguishable. To resolve this, we set a gate on both the $2^+ \rightarrow 0^+$ and $4^+ \rightarrow 2^+$ transitions of ^{100}Sr 129.8/287.9 keV and compared the intensity ratios of its partners' transitions of interest to another double gate on $2^+ \rightarrow 0^+$ and $4^+ \rightarrow 2^+$ transitions of ^{98}Sr 144.3/289.4 keV. The 129.7 keV peak from ^{150}Nd was contaminated as well as some of the other peaks of interest. Therefore, the gate on ^{100}Sr was avoided. Isomeric states had to be considered in the case of ^{153,154}Nd. In ^{154}Nd, the isomeric state at 1298.0 keV is weakly populated therefore, the transitions feeding into it were not added to the total yields.

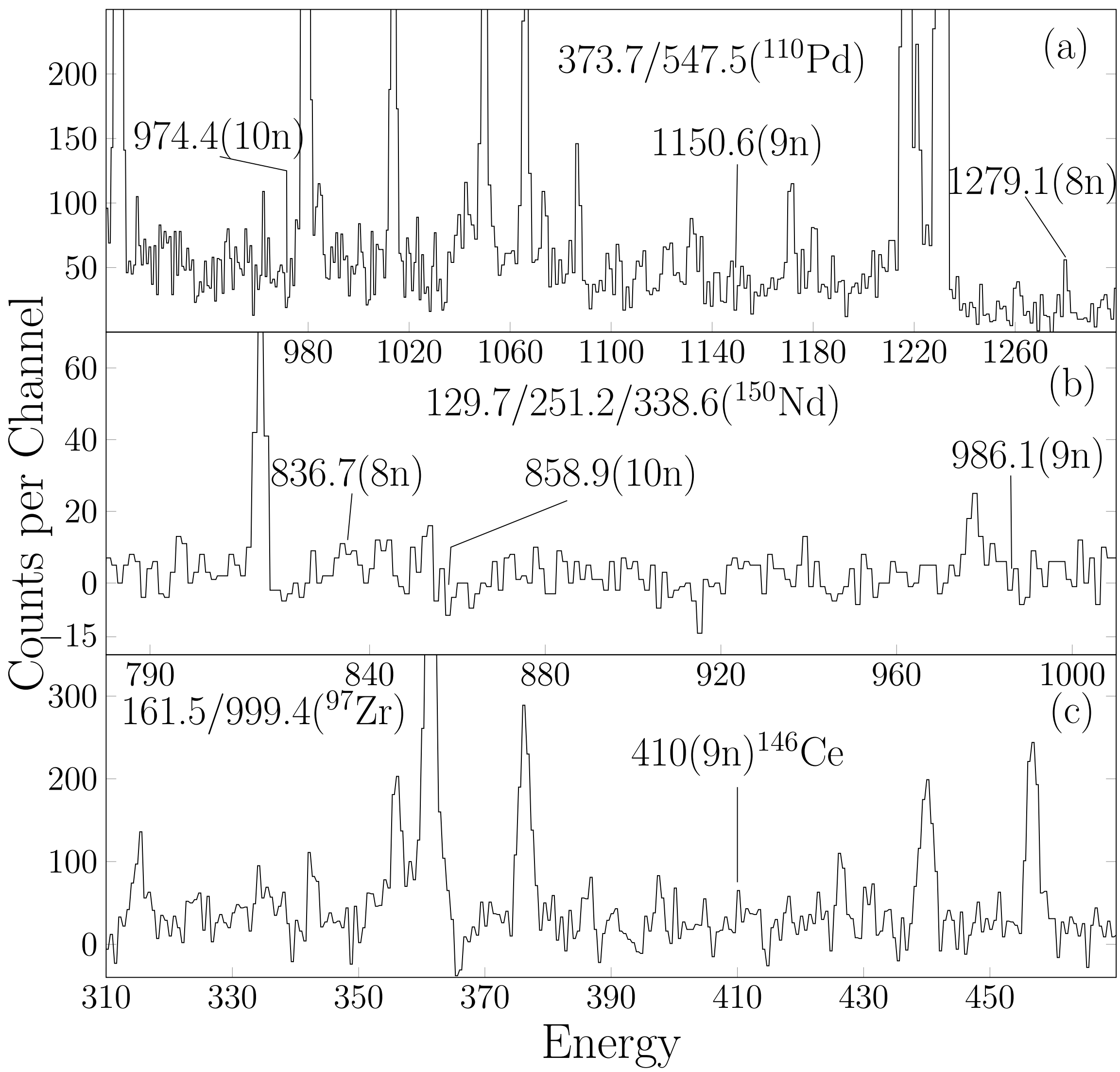

Figure 6.7: Gamma-ray coincidence spectra by gating on (a) 373.7 and 574.5 keV transitions in ^{110}Pd to show that there is no evidence for the 9 and 10 neutron channel at 1150.6 keV in ^{133}Te and at 974.4 keV in ^{132}Te, respectively, whereas there is clear evidence of the 8 neutron channel at 1279.1 keV in ^{134}Te which fits to the curve. In (b) a triple gate on 129.7, 251.2 and 338.6 keV transitions in ^{150}Nd to show that there is no evidence for the 9 and 10 neutron channel at 986.1 keV in ^{93}Sr and at 858.9 keV in ^{93}Sr for the Nd-Sr pair, respectively, whereas there is weak evidence of the 8 neutron channel at 836.7 keV in ^{94}Sr. And in (c) a double gate on 161.5 and 999.4 keV transitions in ^{97}Zr to show evidence for the 9 neutron channel at 410 keV in ^{146}Ce for the Ce-Zr pair.

Table 6.5: New yield matrix for neodymium and strontium from the spontaneous fission of ^{252}Cf.

Yield	^{148}Nd	^{149}Nd	^{150}Nd	^{151}Nd	^{152}Nd	^{153}Nd	^{154}Nd	^{155}Nd	^{156}Nd
^{91}Sr							0.004(1)		0.005(1)
^{92}Sr							0.020(3)	0.019(4)	0.030(5)
^{93}Sr					0.005(1)	<0.05	0.027(5)	0.012(2)	0.022(4)
^{94}Sr			0.010(2)	0.026(4)	0.09(1)	0.18(3)	0.13(2)	0.047(8)	0.043(7)
^{95}Sr			0.017(3)	0.033(6)	0.12(2)	0.30(5)	0.11(2)	0.023(4)	0.012(2)
^{96}Sr			0.040(7)	0.06(1)	0.16(3)	0.23(4)	0.06(1)	0.010(2)	0.005(1)
^{97}Sr			0.030(5)	0.043(7)	0.06(1)	0.07(1)	0.021(4)		
^{98}Sr	0.010(2)	0.031(6)	0.08(2)	0.044(7)	0.06(1)	0.025(5)	0.009(2)		
^{99}Sr			0.020(4)	0.017(3)	0.015(3)				
^{100}Sr			0.026(4)	0.006(1)					

The ^{154}Nd nucleus was reported to have an isomer at 1348 keV in [120], which is not observed in the current data. In that paper, the ground state band transitions were reported as 72, 163, 243, 328 keV... etc, with a 870 keV isomeric transition. In the contrast, both the previous work in [121] and our current data show a 72-163-248 keV cascade for ground state band. In [120], transition energy and levels were also reported in other nuclei ^{156,158}Sm, ^{152,156}Nd. The energy difference between transitions in those nuclei reported in [120] and our current work, as well as other data recorded in nuclear data sheets is generally within 1 keV. Thus, the big 5 keV energy difference in ^{154}Nd between the 243 and 248 keV $6^+ \rightarrow 4^+$ transition may indicate a wrong isotope assignment in [120]. Instead, ^{159}Sm was reported to have an isomer in [122], with 163-243 keV for the first two E2 transitions for the ground state band and 870 keV for the isomeric transition. The 1348 keV isomer reported in [120] may belong to ^{159}Sm, but 5 mass number away from ^{154}Nd. Further details are needed to understand the reason.

According to [108], ^{153}Nd the ground state transitions are 50.0 keV, 120.2 keV and 191.7 keV if our time gate is long enough to cover the isomeric transition. Energies at 50.0 keV, 70.2 keV, 60.7 keV and 78.0 keV reported in [108] are hard to measure accurately to get accurate intensities. Thus, when the ground state transitions are hard to measure we summed up all the next level transitions. In the case of ^{153}Nd, we used 88.3 keV, 197.6 keV and 158.5 keV in the ground state band and 97.9 keV, 175.8 keV and 208.8 keV in the $5/2^+$ band together. These transition are reported in [108]. Figure. 6.6 shows a plot of the extracted yields against the fission's neutron channel number (see Fig. 6.6). Also shown in Fig. 6.7 (b), a triple gate on 129.7, 251.2 and 338.6 keV transitions in ^{150}Nd is used to show that there is no evidence for the 9 and 10 neutron channel at 986.1 keV in ^{93}Sr and at 858.9 keV in ^{93}Sr for the Nd-Sr pair, respectively. Whereas there is clear evidence of the 8 neutron channel at 836.7 keV in ^{94}Sr that fits nicely the single yields curve as shown in Fig. 6.6.

6.5.4 Ce-Zr Yields

In the previous work [3], yield matrix between the $^{98-104}$Zr and $^{144,146-150}$Ce was measured. In the present work, the yields between $^{96-104}$Zr and $^{144-152}$Ce have been measured. In comparison, the previous result [3] on the Ce-Zr pair was slightly overestimated because of the lack of the contribution in ^{96,97}Zr and ^{145,151,152}Ce. It seems that the previous work [3] has normalized to the independent yield of ^{102}Zr. Careful checks have been made to separate the 98 keV g.s. transition in ^{101}Zr and another 98 keV transition populating the 27 keV level in ^{103}Zr.

To determine the cerium (Z = 58) and zirconium (Z = 40) yield matrix, measurements of multiple γ-rays emitted by the Ce-Zr fission fragment pairs formed in spontaneous fission of ^{252}Cf were used to extract the yields. Table 6.6 below displays the absolute yields data that were collected. These are new results and different from the report given in Ref. [123]. In this analysis, most of the transitions of interest were easily identifiable with the exception of the 97.5 keV (9/2$^-$ $\rightarrow$ 5/2$^-$) and 97.4 keV (2$^+$ $\rightarrow$ 0$^+$) from ^{145}Ce and ^{150}Ce, respectively, and ^{101}Zr and ^{103}Zr also have similar transitions of 97.8 keV (5/2$^+$ $\rightarrow$ 3/2$^+$) and 98.4 keV (5/2$^+$ $\rightarrow$ 3/2$^+$), respectively.

To avoid possible contamination, a few gates were set on ^{150}Ce to measure the peaks of interests from its Zr fragment partners. Any contamination of the 98.4 keV transition from ^{103}Zr is avoided since ^{103}Zr and ^{150}Ce are not fission partners in spontaneous fission of ^{252}Cf. However, gating on ^{145}Ce would bring in contamination from both ^{101}Zr and ^{103}Zr. Multiple gates were set on the Zr fragments to measure the ground state transition of ^{145}Ce. By gating on 109.4/146.6 keV of ^{103}Zr, the 97.4 keV transition from ^{150}Ce is once more avoided. Because the channel number between ^{102}Zr and ^{150}Ce is zero, any possible contribution from the 97.4 keV of ^{150}Ce to the 97.5 keV in ^{145}Ce can be neglected given that it is very small. Any gate on ^{101}Zr brings in contribution from both the 97.4 keV of ^{150}Ce to the 97.5 keV in ^{145}Ce. One thing to consider first is to avoid setting any gate using the 97.8 keV in ^{101}Zr. This prevents the contribution from the 98.4 keV in ^{103}Zr. A double

Table 6.6: New yield matrix for cerium and zirconium from the spontaneous fission of ^{252}Cf. The 8-11 neutron channels are labeled with neutron numbers as superscripts.

Yield	^{144}Ce	^{145}Ce	^{146}Ce	^{147}Ce	^{148}Ce	^{149}Ce	^{150}Ce	^{151}Ce	^{152}Ce
^{96}Zr			$0.003(1)^{10}$	0.004^{9}	$0.004(1)^{8}$		0.015(3)	0.025(5)	0.020(4)
^{97}Zr	$0.002(1)^{11}$	$0.005(2)^{10}$	$0.003(1)^{9}$	$<0.009^{8}$	0.028(4)	0.026(5)	0.07(1)	0.08(2)	0.050(9)
^{98}Zr	$0.004(1)^{10}$	$0.005(2)^{9}$	$0.008(3)^{8}$	0.048(8)	0.06(1)	0.14(3)	0.21(4)	0.15(3)	0.06(1)
^{99}Zr	$0.007(3)^{9}$	$0.006(2)^{8}$	0.018(3)	0.056(9)	0.20(3)	0.25(5)	0.30(5)	0.12(2)	0.033(6)
^{100}Zr	$0.011(2)^{8}$	0.032(6)	0.12(2)	0.28(4)	0.55(9)	0.39(7)	0.28(5)	0.11(2)	0.017(3)
^{101}Zr		0.11(2)	0.26(4)	0.33(5)	0.54(9)	0.23(4)	0.17(3)		
^{102}Zr	0.024(4)	0.16(3)	0.43(7)	0.40(6)	0.40(6)	0.10(2)	0.029(5)		
^{103}Zr	0.033(6)	0.14(3)	0.22(4)	0.14(3)	0.12(2)	0.03(1)			
^{104}Zr	0.005(1)	0.07(1)	0.008(1)	0.0013(3)					

gate 216.6/250.9 keV was set on ^{101}Zr and from this gate three peaks were of interest, however, only the 158.7 keV one in ^{150}Ce and a peak around 98 keV, containing both the 97.4 keV peak (^{145}Ce) and 97.5 keV peak (^{150}Ce), were capable of being measured. Since the ratio between 158.7 keV peak (^{145}Ce) and 97.5 keV peak (^{150}Ce) was already known when determining the yields of ^{150}Ce, it was easy to deduce the portion of the contribution of ^{150}Ce from the measured peak. This meant that the remaining portion belonged to the 97.4 keV peak (^{145}Ce). This method was repeated for ^{100}Zr.

In the present study we observed evidence of the 9, 10 and 11 neutron channels in the Ce-Zr fission pairs. A double gate on 397.2 keV and 541.2 keV in ^{144}Ce shows evidence for the 10 neutron channel at 1222.9 keV in ^{98}Zr (see Fig. 6.8). However, in this gate the intensity is not very clear. Therefore, we checked for clean transitions to gate on in ^{144}Ce to avoid contamination and we found that other double and triple gates on 397.2, 541.2, 709.1 and 585.2 keV were good candidates that can be used to verify this observed peak. As shown in Fig. 6.8 (a), (b), (c) and (d) all these gates show evidence of the presence of the 10 neutron channel for the ^{98}Zr-^{144}Ce fission pair. In part (e) of Fig. 6.8 there is another clear evidence of the 10 neutron for the ^{146}Ce and ^{96}Zr pair at 1750.4 keV by gating on 409.9/503.2 keV in ^{146}Ce. To measure the intensity of the 1750.4 keV, we accounted for the presence of 1751 keV in ^{100}Zr (which would make this yield higher than what it should be) by subtracting the portion of 1751 keV from the measured 1750.4 keV in ^{146}Ce and ^{96}Zr pair since we already had the real intensity for that. Part (f) of Fig. 6.8 gives further evidence for the presence of the 1750.4 keV.

There is a clear 1103 keV peak when gating on ^{146}Ce. The intensity of this peak however, is higher than expected. We discovered that this high intensity is due to a strong contamination around this peak from beta decay where a 1103 keV transition in ^{146}Ce feeds a 1810.2 keV level. There is also a clear peak at 258 keV in ^{146}Ce when one gates on ^{97}Zr. However, for any of the possible gates on ^{97}Zr, it is difficult to find a good reference peak that has the expected ratio with the 258 keV peak. Therefore, we measured the 409.9

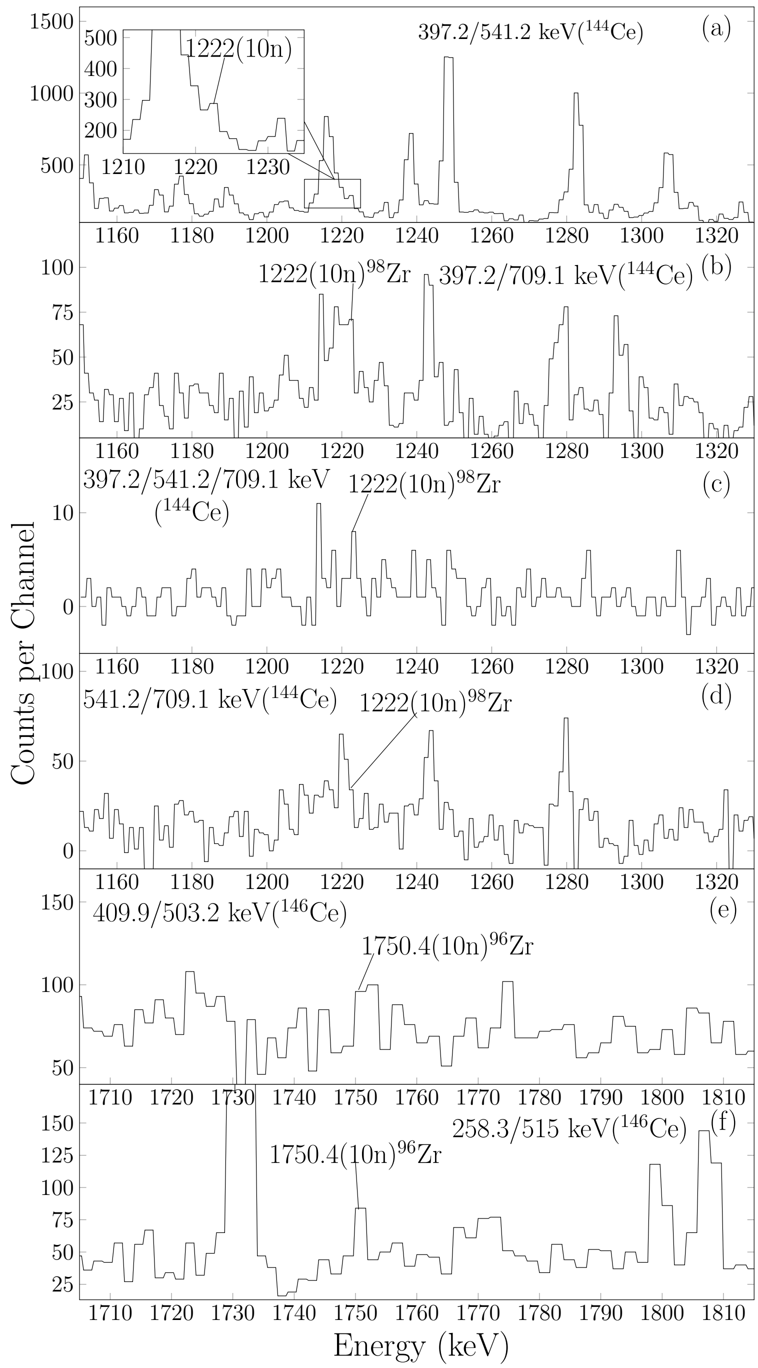

Figure 6.8: Gamma-ray coincidence spectra by gating on (a) 397.2/541.2 keV, (b) 397.2/709.1 keV, (c) 397.2, 541.2 and 709.1 keV and (d) 541.2/709.1 keV transitions in ^{144}Ce to show that there is evidence for the 10 neutron channel at 1222 keV in ^{98}Zr for the ^{98}Zr-^{144}Ce pair. In (e), a double gate on 409.9/503.2 keV transitions in ^{146}Ce to show clear evidence of the 10 neutron for the ^{146}Ce and ^{96}Zr pair at 1750.4 keV by gating on 409.9/503.2 keV. And (f) gives further evidence for the presence of the 1750.4 keV transition by gating on 258.3/515 keV

keV peak which has the expected ratio with the 209.1 keV peak taking into consideration their intensities, efficiency, and internal conversion relative to the ground state transitions. Another challenging channel to measure is the ^{144}Ce-^{97}Zr. There is a strong 1102.8 keV peak feeding into the 4^+ level (938.6 keV) in ^{144}Ce. Hence, the presence of the 11 neutron channel at about the 397.2 keV peak would be influenced by the overlapping two transitions of 1103 keV in both ^{144}Ce and ^{97}Zr. Nevertheless, there is clear evidence of the 11 neutron channel.

Upon completion of the matrix yield of the correlated fragment pairs of Ce-Zr in the spontaneous fission of ^{252}Cf, the yields were next scaled according to Ter-Akopian's independent yield [16] and summed for each isotope of Ce. This summation and Ter-Akopian's calculated data for Ce-Zr, were both normalized such that ^{148}Ce had a value of 100. Then these two data sets were compared to see if Ter-Akopian's calculations could be verified. As can be seen in Fig. 6.6, the present absolute yield data Te-Pd, Nd-Sr and Ce-Zr are in agreement with the previous ones [16], and thus are experimentally confirmed with smaller error limits. The results from the present study show evidence for an "extra hot fission mode" as shown Fig. 6.9. This is the first time this mode is observed in Ce-Zr pairs; it is $\sim$1.0(3)% of the first mode. The observation of this mode in this pair can be explained when one considers that $^{143-145}$Ba and ^{146,148}Ce have been determined to be octupole deformed [124, 125, 126, 127, 2] and may also have hyperdeformation at scission to give these nuclei high internal energy and in turn gives rise to high neutron multiplicities. The second curve (6-11 neutrons) in Fig 6.9 was fitted by restricting the width of the second curve to the width of the first curve (0-7 neutron channels) and the position to 8 neutron channel. If the unfixed width method is used instead, the width of the Ce-Zr first curve is 6% larger than the Ba-Mo width. However, the 10 neutron channel in Ce-Zr pair is obviously above the tail of the first Gaussian in either way.

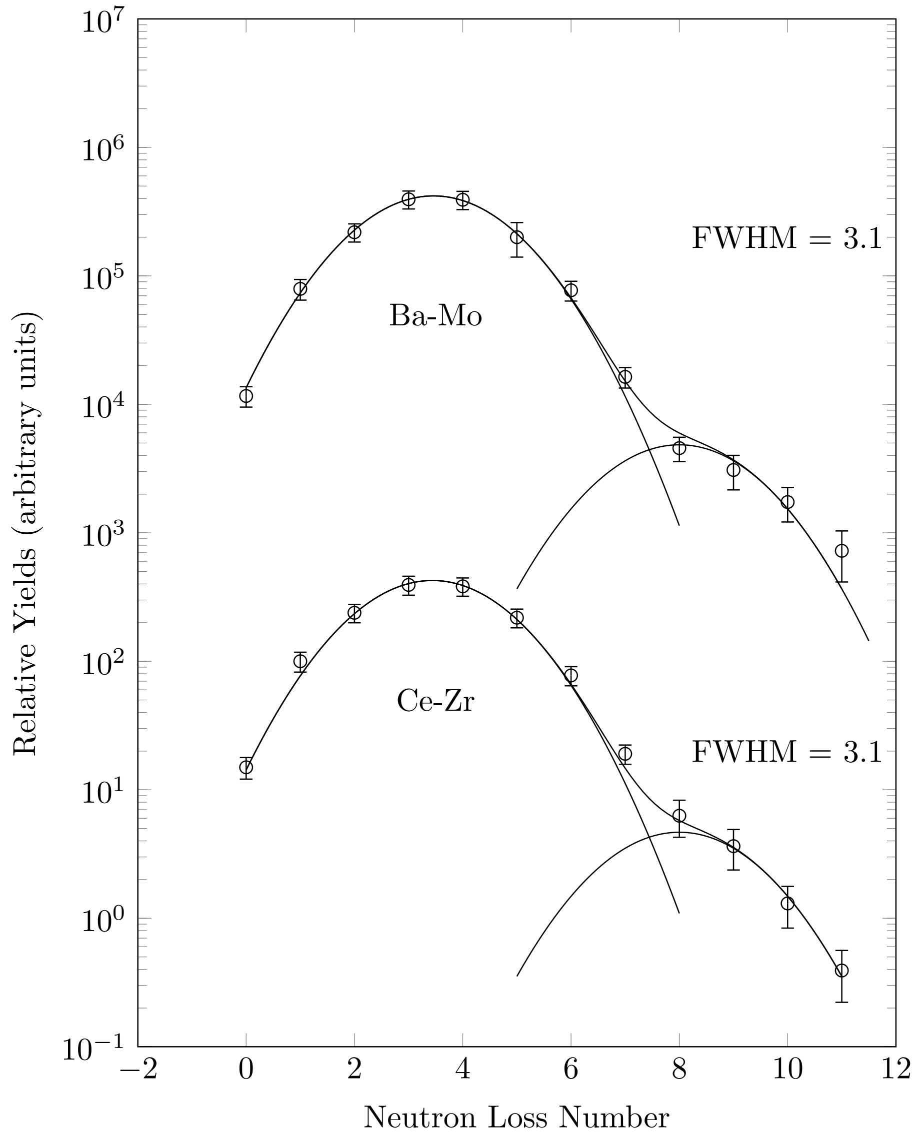

Figure 6.9: The second curve in Ce-Zr was fitted by fixing the width of the second curve (presenting the second mode) to the width of the first curve (presenting the first modes) and also fixing the position to 8 neutron channel. It contributes ~1.0(3)% of the first mode. The second curve in the Ba-Mo fit was also fitted by fixing the width of the second curve to the width of the first curve and fixing the position to 8 neutron channel. It contributes ~1.5(4)% of the first mode.

6.5.5 Ba-Mo Yields

Previously, the yield matrix of the Ba-Mo pairs was measured in [3, 16, 23, 4]. In Ref. [3, 16], the yield matrix was normalized to the independent yields of ^{140,142,144,146}Ba without the contribution of ^{100,101,109,110}Mo. Those Mo isotopes are very weakly populated in ^{252}Cf SF so that the previous results are close to the present work compared to the large difference in Te-Pd and Nd-Sr. In Ref. [23], the 519 keV transition populating the 4^+ g.s. band level in ^{104}Mo and 414 keV transition populating the 4^+ g.s. band level in ^{108}Mo were used to measure their yields to avoid measuring the 192.0 and 192.7 keV g.s. transitions in ^{104,108}Mo, respectively. Such a method is wrong because there is a strong 519 keV transition in ^{103}Mo and a strong 414 keV transition in ^{109}Mo. Therefore, when measuring the 519 keV peak in the Ba partner gate, one would get the summation of the 519 keV from ^{103}Mo and ^{104}Mo. Similarly, when measuring the 414 keV peak in the Ba partner gate, one would get the summation of the 414 keV from ^{108}Mo and ^{109}Mo.

The new yields of Ba-Mo are given in Table 6.7 and Fig. 6.6. The 8-10 neutron yields presented in the present study are much lower than both the ones reported earlier; contributing $\sim$1.5(4)% of the first mode. In the first report [3], the second mode was reported to contribute $\sim$7% of the first mode with significantly lower $\langle$TKE$\rangle$, 153/189 MeV [3]. The second report to have observed this mode [4], reported that it contributed $\sim$3%. The current experimental data have improved statistics over the other two experimental data from which the first and second analysis came. Therefore, one would expect that the second mode would be more pronounced in this experiment. However, this is not the case because with improved statistics comes more complete level schemes that provide new insights on possible contamination that were otherwise not considered in the previous analyses causing either overestimation or underestimation of the yields. Gating on Ba isotopes and Mo isotopes should give the similar yield results. Such cross-checks were used in this experiment to investigate the contamination given that contaminates are more common in Ba-Mo than in Ce-Zr, Te-Pd, Xe-Ru and Nd-Sr pairs.

In detail, in the analysis of Mo-Ba yields, one has to be extra careful when determining the yields of ^{140}Ba-^{104}Mo and the ^{138}Ba-^{104}Mo which correspond to the rare 8 and 10 neutron channels and the ^{140}Ba-^{108}Mo and the ^{138}Ba-^{108}Mo yield which correspond to the 4 and 6 neutron channels. This is because of the possible contamination that arise from the

Table 6.7: New yield matrix for barium and molybdenum from the spontaneous fission of ^{252}Cf. The 8-11 neutron channels are labeled with neutron numbers as superscripts.

Yield	^{138}Ba	^{139}Ba	^{140}Ba	^{141}Ba	^{142}Ba	^{143}Ba	^{144}Ba	^{145}Ba	^{146}Ba	^{147}Ba	^{148}Ba
^{100}Mo					0.004(1)^{10}				0.009(2)		
^{101}Mo									0.017(3)		0.005(1)
^{102}Mo				0.005(2)^{9}	0.015(3)^{8}	0.023(5)	0.09(2)	0.12(2)	0.18(3)	0.18(3)	0.031(6)
^{103}Mo	0.009(3)^{11}	0.004(1)^{10}	<0.005(1)^{9}	0.010(2)^{8}	0.07(1)	0.20(3)	0.42(7)	0.44(7)	0.35(6)	0.21(4)	0.014(3)
^{104}Mo	0.009(2)^{10}	0.007(2)^{9}	0.010(2)^{8}	0.05(1)	0.24(4)	0.53(8)	1.08(17)	0.73(11)	0.37(6)	0.18(3)	0.006(1)
^{105}Mo	0.008(2)^{9}	0.003(1)^{8}	0.022(4)	0.18(3)	0.48(8)	1.01(17)	1.09(19)	0.47(9)	0.10(2)	<0.04	
^{106}Mo	0.015(3)^{8}	0.010(2)	0.09(2)	0.39(7)	1.05(17)	1.09(17)	0.72(12)	0.27(4)	0.02(1)		
^{107}Mo	0.009(2)	0.020(4)	0.13(3)	0.31(6)	0.57(10)	0.30(6)	0.16(3)				
^{108}Mo	0.011(3)	0.028(5)	0.14(3)	0.22(3)	0.22(4)	<0.09	0.05(1)				
^{109}Mo	0.008(2)	0.015(3)	0.034(7)								
^{110}Mo	<0.008	0.008(2)									

unresolved 192.4 keV and 192.9 keV $2^+ \rightarrow 0^+$ transition for ^{104}Mo and ^{108}Mo, respectively (see [5] for similar analysis). In a previous analysis [5], a gate on 602.4/529 keV in ^{140}Ba was used to measure the intensities of 368.6 keV and 371.0 keV transitions in ^{104}Mo and ^{108}Mo, respectively. In such gate, the 369 keV peak has $\sim$ 30 counts and is 1/3 (1/14 in our data) of the 371 keV one. In contrast, as seen in Fig. 6.10 part (b), our data show $\sim$ 9000 counts for the 371 keV peak, while the 369 keV one is just above the background. Thus, it is possible that the ^{140}Ba-^{104}Mo yield was overestimated due to the background fluctuation (10-20 counts) in Ref. [5]. A gate was set on the first two transitions of the ^{108}Mo isotope

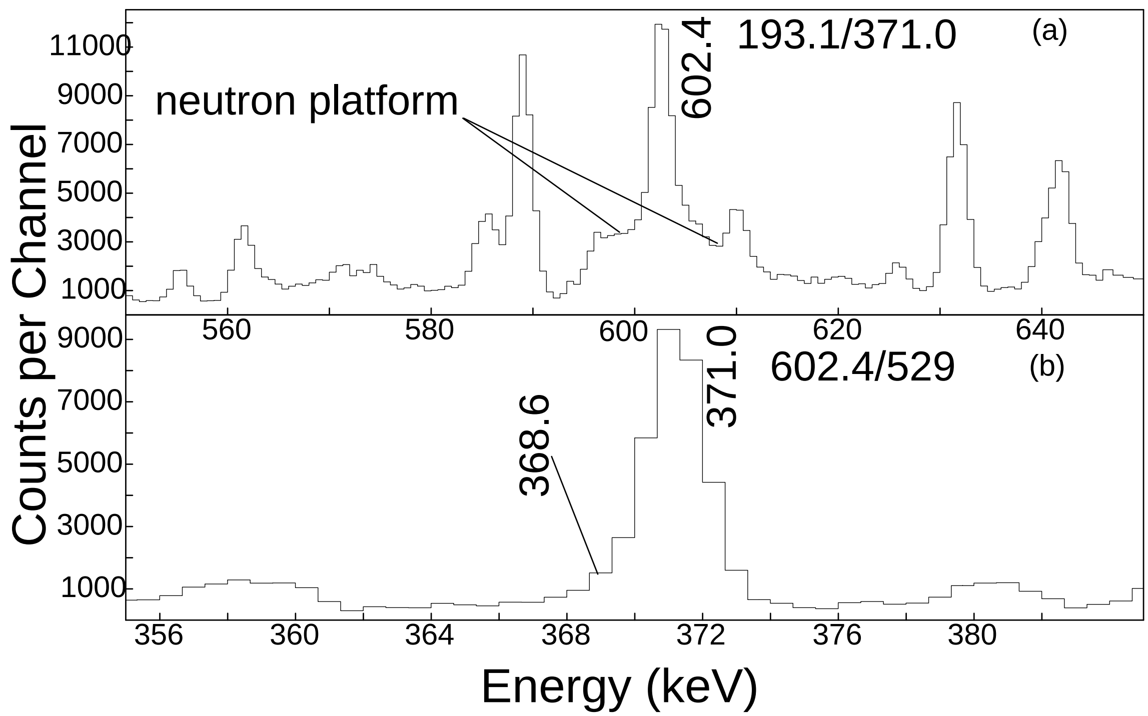

Figure 6.10: Gamma-ray coincidence spectra by gating on (a) 193.1 and 371.0 keV transitions in ^{108}Mo to show the neutron inelastic scattering platform, and (b) 602.4 and 529 keV transitions to show the 369 keV in ^{104}Mo and 371 keV in ^{108}Mo. Part (b) shows difference between Fig. 1 in Ref. [5] using the same gate. See text for more details.

and the ground state transition (1435.7 keV) of ^{138}Ba was measured as well the $(8^+ \rightarrow 6^+)$ transition populating the isomeric state at 2089 keV level because it is very strong in our data. When measuring the yields of ^{138}Ba-^{104}Mo, however, the 192.4 keV from ^{104}Mo has to be avoided to prevent contamination from 192.9 keV from ^{108}Mo since it is strong and can enhance this yield. Instead, gates on 368 keV and 519 keV transitions from ^{104}Mo were set and this time only the 1435.7 keV transition in ^{138}Ba was measured (see Fig. 6.11 (a)). Also in Fig. 6.11 (b) is shown the 9 neutron channel seen in the 94.9-138.1 keV transitions in ^{105}Mo to show the 9 neutron channel at 1435.7 keV in ^{138}Ba.

Furthermore, unlike in Ref. [5] we did not set a gate using the 602 keV from ^{140}Ba when determining the yield of ^{140}Ba-^{108}Mo pair because 602 keV is present in ^{104}Mo from the $8^+ \rightarrow 6^+$ transition feeding into the 1725 keV level and another weaker 602 keV $8^+ \rightarrow 6^+$ transition feeding into the 2685.4 keV level. This means that setting any gate with 602 keV from ^{140}Ba to measure desired peaks in ^{104}Mo would bring in contamination. The other reason is that 602 keV lies on a complex region associated with an inelastic neutron scattering in germanium of the detectors as discussed in Ref. [22]. This neutron platform is not negligible; the background around this region is too high and as a result it is in coincidence with every other peak on the spectra (see Fig. 6.10 (a)). In Ref. [22], the 528.2 keV $4^+ \rightarrow 2^+$ transition was used in the place of the 602.4 keV in ^{140}Ba. However, transitions with energies close to 528 keV are present in ^{104}Mo from $7^- \rightarrow 6^+$ (feeding into the 2083.8 keV level), ^{105}Mo from $21/2^- \rightarrow 19/2^-$ (feeding into the 1352.9 keV level), ^{106}Mo from $6^+ \rightarrow 6^+$ (feeding into the 1033.48 keV level), and ^{108}Mo from $6^+ \rightarrow 4^+$ (feeding into the 564 keV level). Although they are weak transitions, when considering which one to gate on between the ^{104}Mo and ^{140}Ba, they are comparable in intensities when gating on ^{104}Mo which would result in contamination but sufficient when gating on ^{140}Ba. Such cases should also be carefully treated when measuring other high neutron channels with low yields, e.g ^{105,106}Mo-^{140}Ba pairs.

Another approach that has been used in the past to resolve this problem is presented in Ref. [104]. In the analysis of Ref. [104], the intensities of 519 keV ($6^+ \rightarrow 4^+$ transition in ^{104}Mo) and the 414 keV ($4^+ \rightarrow 4^+$ transition in ^{108}Mo) were measured instead of the ground state transitions for the yields. However, there is another 414 keV present and strong in ^{107}Mo from $(15/2)^- \rightarrow (11/2)^+$ (feeding into the 2083.8 keV level). When gating on Ba transitions to measure the 414 keV in ^{108}Mo, the strong 414 keV transition from ^{107}Mo will contaminate the spectra. Whereas, the 519 keV transition is okay in this case because even though it is present in ^{103}Mo it is weaker to contaminate the spectrum. Therefore, a gate on (519/641) keV from ^{104}Mo was used to measure the 602 keV in ^{140}Ba. These two gated transitions are located high enough in the ^{104}Mo level scheme and have no feeding from the two contaminants (602 keV transitions mentioned earlier) in ^{104}Mo. In this case, we used a local background subtraction which was set higher than usual to reduce the contribution from the neutron platform. This too does not completely circumvent the problems but it gave us a good approximation of what the yield should be. For more major overlapping transitions in Ba-Mo pairs to be considered when conducting this analysis refer to Table 6.8. Through this thorough examination of the Ba-Mo yield there is clear evidence of the 9 and 10 neutron channel yields as in Fig. 6.11.

The errors are significantly reduced because of the improved statistics, the use of quadruple coincidence data and improved knowledge of level schemes. To calculate all absolute errors, the experimental data were normalized to values from Wahl's tables [118]. Specifically, the summation of ^{144}Ba yields was normalized to Wahl's value because it was the strongest yield in our experiment. Note that the values from Wahl's tables only considered ground state γ transitions but we have considered the branching ratios from feeding bands. The 15% errors from Wahl's data were added to our absolute errors as well as 5-10 % experiment errors from missing transitions and contamination in our data.

As seen in Fig. 6.6, a similar deviation from a Gaussian fit to the data for the 0 to 7 neutron emission channels is seen at neutron numbers 7, 8, 9 and 10 in the Ba-Mo yields as observed in [3, 4]. In comparison to these results, a noticeable difference is that in the present analysis we have a more complete set of yield pairs; $^{100-110}$Mo and $^{138-148}$Ba. This is not the case for the earlier analyses where ^{139}Ba is missing in [3, 5, 4] and ^{138}Ba in [5]. These are very important components of the analysis as they contribute to the intensity of the second hot mode. Additionally, the 9 and 10 neutron channels were not reported in [5]

Table 6.8: Part of the major overlapping energies transitions in Ba-Mo pairs that could result in contamination. See text for more instructions.

Energy (keV)	Nuclei	E_i to E_f (keV)
110	^{107}Mo ^{109}Mo ^{145}Ba ^{147}Ba	458→348 333→222 618→508 110→0
113	^{103}Mo ^{145}Ba	354→241 113→0
172	^{105}Mo ^{106}Mo ^{107}Mo	796→623 172→0 492→320
185	^{145}Ba ^{147}Ba	463→277 185→0
192	^{104}Mo ^{108}Mo ^{138}Ba	192→0 193→0 2089→1898
250	^{103}Mo ^{147}Ba	354→103 360→110
414	^{107}Mo ^{108}Mo	566→152 979→564
493	^{107}Mo ^{143}Ba	950→458 954→461
519	^{103}Mo	1157→637 1180→561
529	^{104}Mo ^{105}Mo ^{106}Mo ^{108}Mo ^{140}Ba	2612→2083 1882→1353 1563→1033 1508→979 1130→602 1660→1130
602	^{104}Mo ^{140}Ba neutron platform	2326→1725 2685→2083 602→0

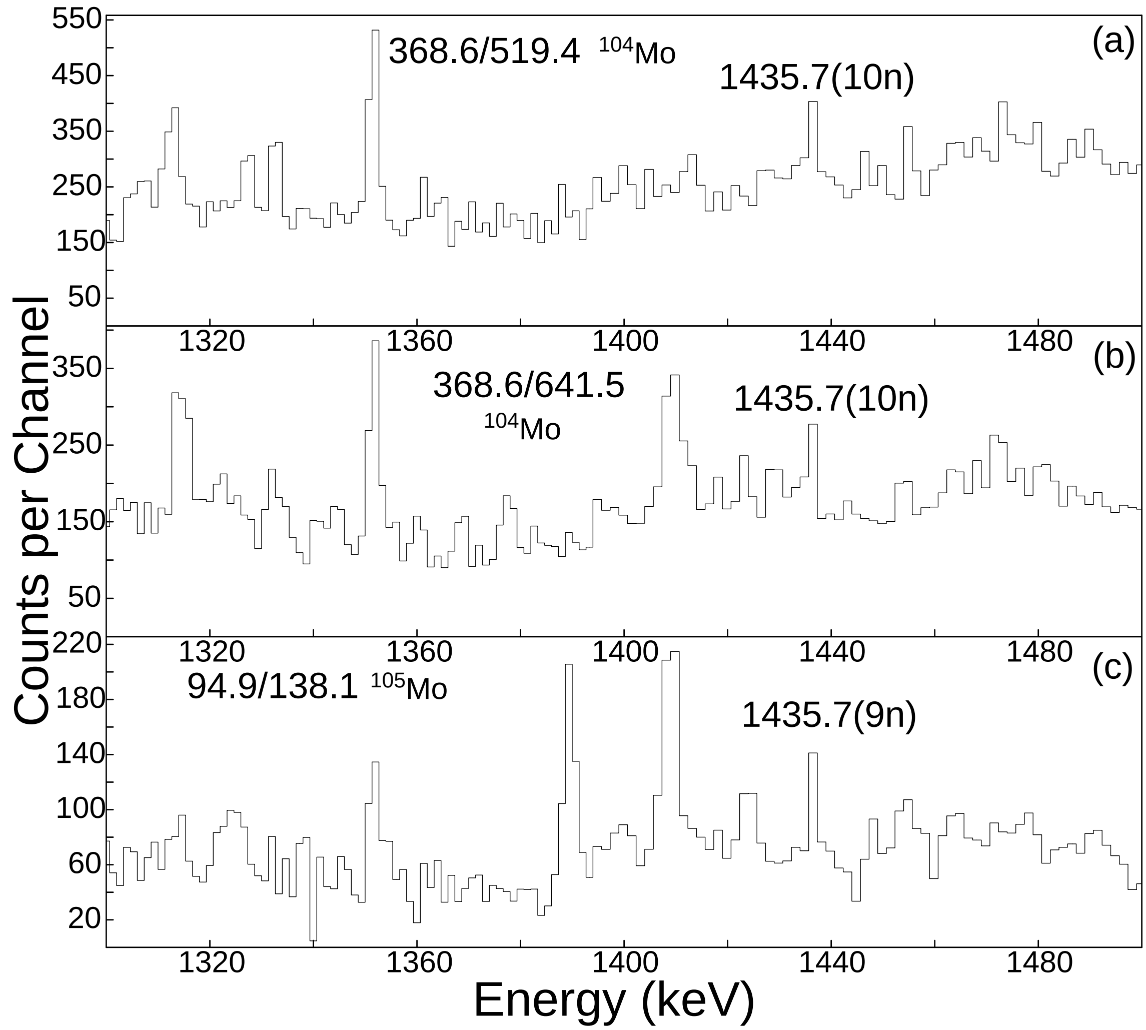

Figure 6.11: Gamma-ray coincidence spectra by gating on (a) 368.6 and 519.4 keV transitions in ^{104}Mo to show evidence for the 10 neutron channel at 1435.7 keV in ^{138}Ba and in (b) another gate on 368.6 and 641.6 keV transitions in ^{104}Mo to give further evidence of the 10 neutron channel in the ^{138}Ba-^{104}Mo. In (c) a gate on 94.9 and 138.1 keV transitions in ^{105}Mo to show evidence for the 9 neutron channel at 1435.7 keV in ^{138}Ba for the Ba-Mo pair.

and [104, 24] (same data set in these two) did not report only the 10 neutron channel. Note that there is a typographical error in the ^{142}Ba-^{102}Mo yield in Ref. [104]. This reported yield is too small (0.007) compared to ^{144}Ba-^{104}Mo (102) in the same reference. The second smallest reported yield in Ref. [104] was 0.35, which is two orders larger than the 0.007 value. However, as shown in Fig 6.11, the 9 and 10 neutron channels are present. And in the current study we have also observed the 11 neutron channel at the 1435 keV

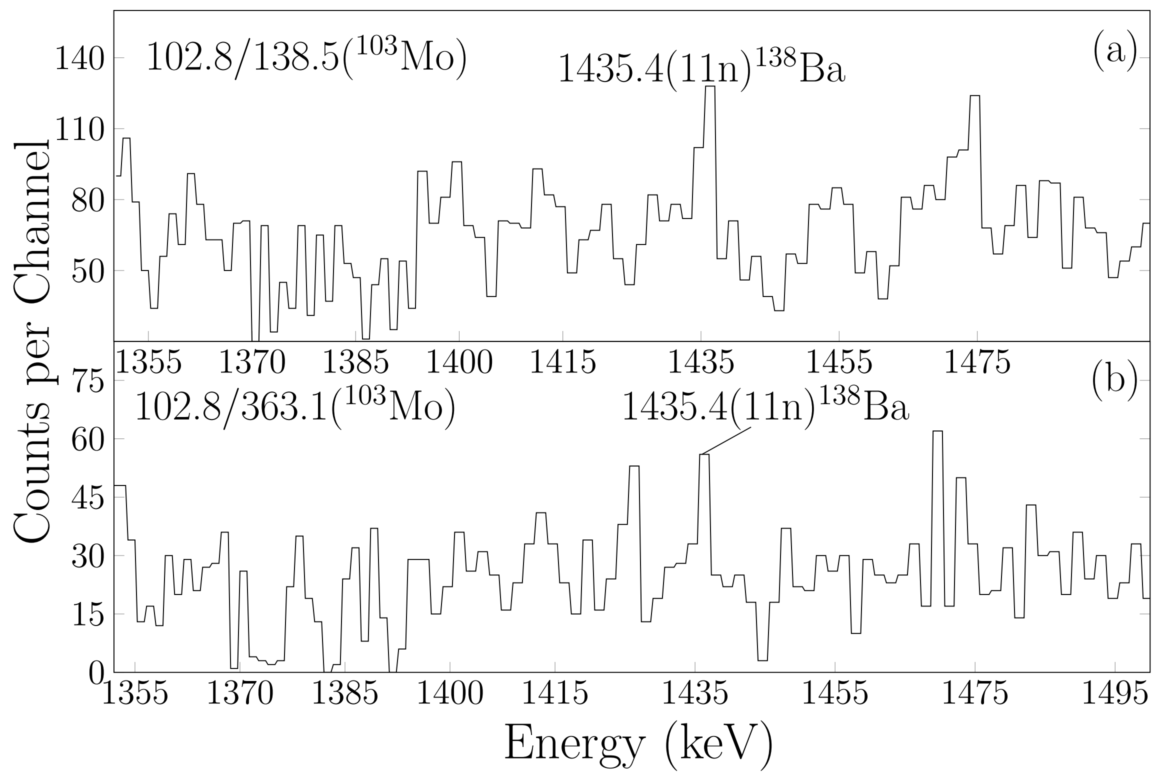

Figure 6.12: Gamma-ray coincidence spectra by gating on (a) 102.8 and 135.5 keV transitions in ^{103}Mo to show evidence for the 11 neutron channel at 1435.7 keV in ^{138}Ba and in (b) another gate on 102.8 and 363.1 keV transitions in ^{103}Mo to give further evidence of the 11 neutron channel in the ^{138}Ba-^{103}Mo pair.

peak in ^{138}Ba as seen in Fig. 6.12. This channel is observed in several gates but in Fig. 6.12 we only show two gates on 102.8/138.5 keV peaks in (a) and 102.8/363.1 keV peaks in (b) and they are both from ^{103}Mo. Also in Fig. 6.9, we show a second Gaussian fit to the 8, 9, and 10 as reported earlier [128] and added the 11 neutron channel. In Ref. [128], we fitted a second Gaussian by means of restricting the peak position of the second mode to greater than 6 neutrons emitted. However, in the present study we were able to obtain a reasonable fit by restricting the peak position of the second fit to ~ 8 and width of the second curve was fixed to the width of the first curve. This new analysis of Ba-Mo fission pairs, coupled with the new analysis of Ce-Zr yields, which shows a reduced “extra hot mode”, and the Te-Pd, Xe-Ru and Nd-Sr yields, which do not exhibit 8, 9, 10 neutron emissions, confirms the existence of this “extra hot mode" in the Ba-Mo and now found in Ce-Zr yields.

6.5.6 Independent Yields

The fission fragment isotopic distributions are compared with the previous results [3], as shown in Figs. 6.13, 6.15, 6.14 and 6.16. The results are deduced from the integral of each isotope in the Tables 6.4, 6.3, 6.5, 6.6, 6.7. Note that, some of the previous results without available experimental data for some fragments were deduced by interpolations. For example, ^{133,135}Te, ^{135,141}Xe, ^{139}Ba, ^{145}Ce, ^{151,153}Nd, ^{97}Sr and ^{109,111,113,115}Pd. The present work shows odd-even effect for the Te, Nd, Sr, and Pd isotopes. This effect was not found in the previous results because of the interpolation method used before [3]. The present results also show odd-even effect at around $^{100-102}$Mo. This may be due to the very weak population in ^{101}Mo so that the corresponding fragment pairs with Ba are hard to measure.

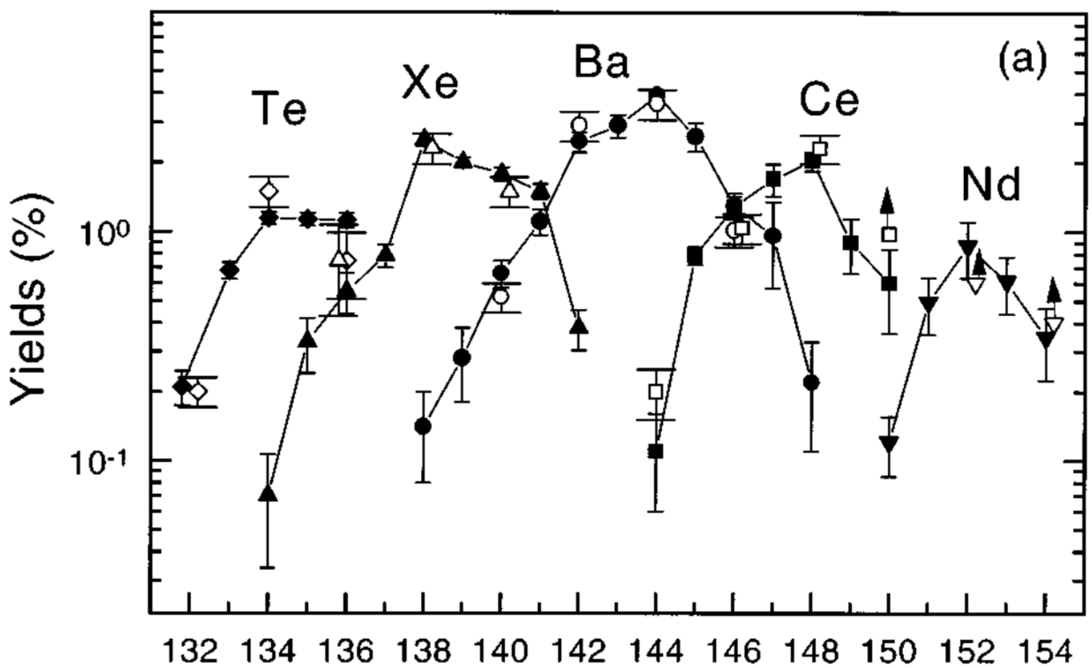

Figure 6.13: Fission fragments distributions deduced from the fragment pair independent yields given Ref. [3]. The black filled symbols are from the experimental data in Ref. [3] and the open symbols are from data given in [6]

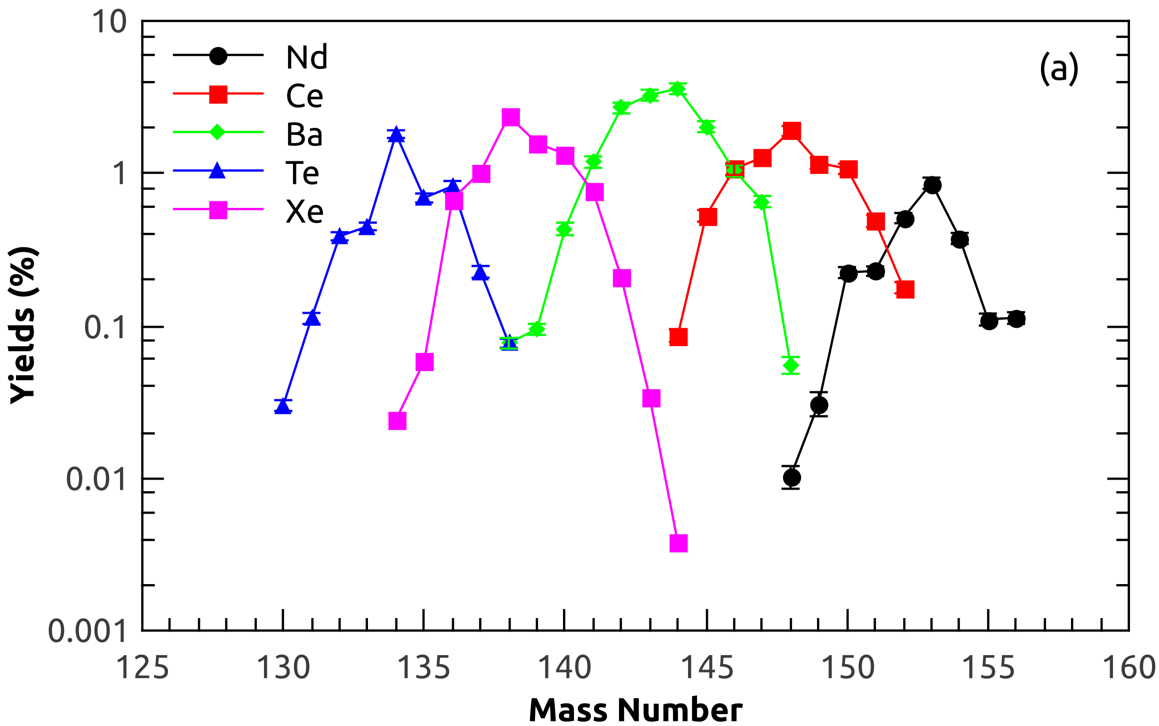

Figure 6.14: Fission fragments distributions deduced from the fragment pair independent yields given Tables 6.4, 6.3, 6.5, 6.6, 6.7.

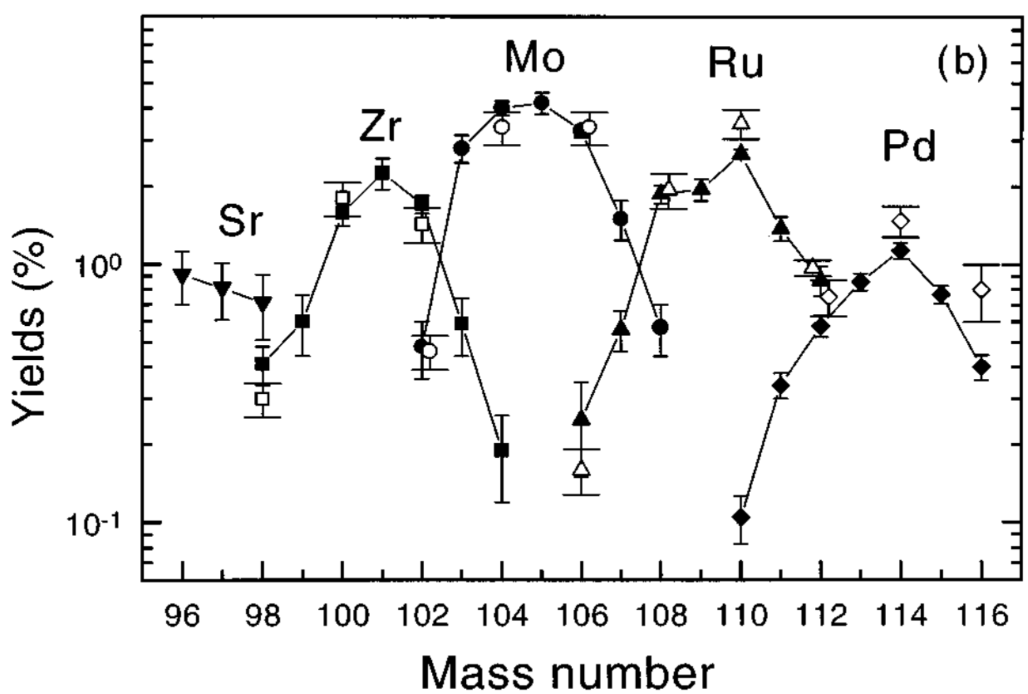

Figure 6.15: Fission fragments distributions deduced from the fragment pair independent yields given Ref. [3]. The black filled symbols are from the experimental data in Ref. [3] and the open symbols are from data given in [6]

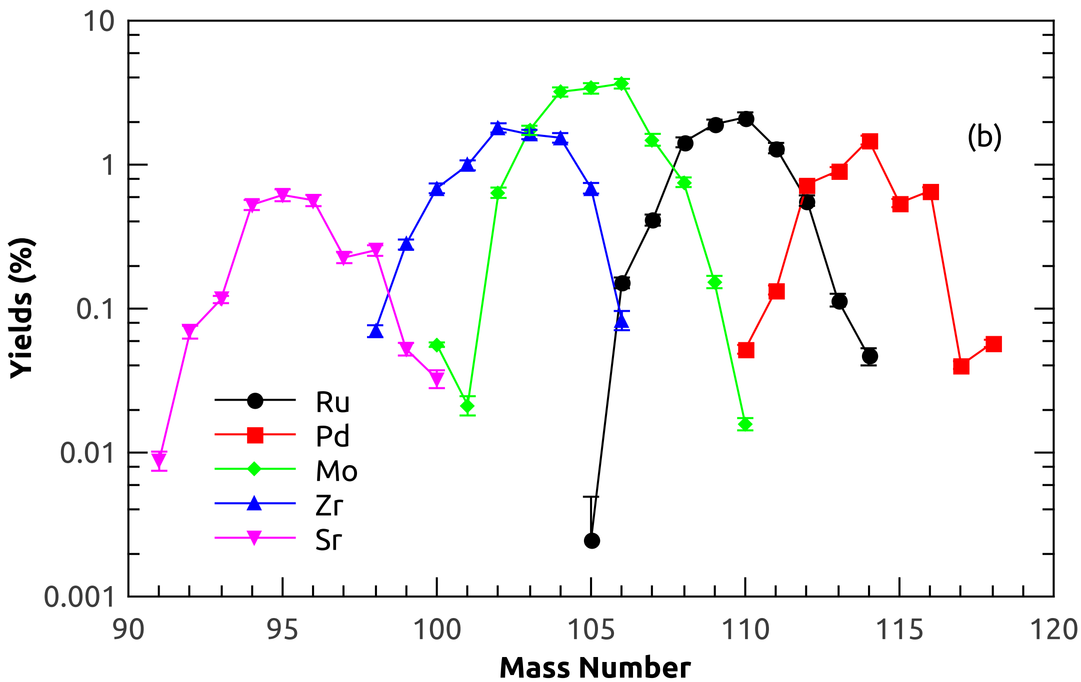

Figure 6.16: Fission fragments distributions deduced from the fragment pair independent yields given Tables 6.4, 6.3, 6.5, 6.6, 6.7.

6.6 Conclusion

In the present work, new yield matrices were determined for Te-Pd, Xe-Ru, Nd-Sr, Ce-Zr and Ba-Mo fission partners from the spontaneous fission of ^{252}Cf. Part of the Te-Pd and Nd-Sr work was done by the REU student Hank Richard. The REU student Andrew Thibeault was partially involved in the measurement of the Ba-Mo yield. A similar deviation from the Gaussian fit to the normal fission mode was found in Ba-Mo for the 8, 9, and 10 neutron channels as found in previous analyses to confirm the existence of the proposed "extra-hot-fission" mode. We have also observed an "extra hot fission mode" for the first time in Ce-Zr pairs. In both cases, 11 neutrons were observed for the first time. The observation of these modes in both pairs can be explained by considering that ^{143,144,145,146}Ba and ^{146,148}Ce have been determined to be octupole deformed which can help give these nuclei high internal energy at scission and in turn gives rise to high neutron multiplicities. This is in addition to the possible hyperdeformation suggested for these nuclei in [3]. Errors are reduced in this newest analysis compared to previous studies because of the greater statistics of the latest Gammasphere experiment and the use of quadruple coincidences in the analysis and improved level schemes. A new experiment is being planned to do fission fragment-γ-γ coincidence studies to investigate details of the fission process and to study new more neutron-rich nuclei. In addition, the investigation will study the existence of an "extra hot mode" observed in Ba-Mo and Ce-Zr fission yields as well as ascertain whether these second modes are a result of hyperdeformation and/or octuple deformation of ^{144,145,146}Ba and ^{146,148}Ce. This work was published in Physical Review [129].

Chapter 7

Conclusion

In summary, high spin states of neutron-rich ^{104,106}Mo have been reinvestigated by analyzing the γ-rays in spontaneous fission of ^{252}Cf with Gammasphere. Both $\gamma-\gamma-\gamma$ and $\gamma-\gamma-\gamma-\gamma$ coincidence data were analyzed. New levels and transitions have been identified in both isotopes. A new ΔI=1 band has been discovered in ^{104}Mo with a tentative 5^- bandhead, and is proposed to form a class of chiral vibrational doublets with another 4^- band previously found. Angualar correlation measurements have been performed to determine the spins and parities in both isotopes. Bands (4) and (5) in these nuclei are proposed as soft chiral vibrational doublet bands. These doublet rotational bands in ^{104}Mo show similar behavior to those in ^{106}Mo but exhibit smaller separation energies. The levels of the 4^- and 5^- chiral doublets in ^{106}Mo have bee reassigned The theoretical calculations support the assignments of these newly observed bands as soft chiral doublet bands built on the $h_{11/2}$ quasineutron and a pseudo spin pair of $(d_{5/2}g_{7/2})$ quasineutrons. TPSM calculations have been performed for the chiral doublet bands in ^{104,106}Mo. The results show reasonably good agreement with the experiement data. PES calculations have been performed, however, more theoretical work is needed to understand the band 6 to 10 structures and configurations in ^{106}Mo.

Furthermore, new yield matrices were determined for Te-Pd, Xe-Ru, Nd-Sr, Ce-Zr and Ba-Mo fission partners from the spontaneous fission of ^{252}Cf. A similar deviation from the Gaussian fit to the normal fission mode was found in Ba-Mo for the 8, 9, and 10 neutron channels as found in previous analyses to confirm the existence of the proposed “extra-hot-fission” mode. We have also observed an “extra hot fission mode” for the first time in Ce-Zr pairs. The observation of these modes in both pairs can be explained by considering that ^{143,144,145,146}Ba and ^{146,148}Ce have been determined to be octupole deformed which can help give these nuclei high internal energy at scission and in turn gives rise to high neutron multiplicities. This is in addition to the possible hyperdeformation suggested for these nuclei. Errors are reduced in this newest analysis compared to previous studies because of the greater statistics of the latest Gammasphere experiment and the use of quadruple coincidences in the analysis and improved level schemes. A new experiment is being planned to do fission fragment-γ-γ coincidence studies to investigate details of the fission process and to study new more neutron-rich nuclei. In addition, the investigation will study the existence of an "second extra hot mode" observed in Ba-Mo and Ce-Zr fission yields as well as ascertain whether these second modes are a result of hyperdeformation and/or octuple deformation of ^{144,145,146}Ba and ^{146,148}Ce.

BIBLIOGRAPHY

[1] J. M. Eldridge, B. Fenker, J. H. Hamilton, C. Goodin, C. J. Zachary, E. Wang, A. V. Ramayya, A. V. Daniel, G. M. Ter-Akopian, Yu. Ts. Oganessian, Y. X. Luo, J. O. Rasmussen, and S. J. Zhu. E2/M1 mixing ratios in transitions from the gamma vibrational bands to the ground state rotational bands of ^{102,104,106,108}Mo, ^{108,110,112}Ru, and ^{112,114,116}Pd. *Eur. Phys. J. A*, 54:15, 2018.

[2] S.-J. Zhu, J. Hamilton H., A. Ramayya V., J. Hwang K., J. Rasmussen O., Y. Luo X., L. K., J.-G. Wang, X.-L. Che, H.-B. Ding, S. Frauendorf, V. Dimitrov, Q. Xu, L. Gu, and Y.-Y. Yang. Search for chiral bands in A $\sim$ 110 neutron-rich nuclei. *Chinese Physics C*, 33:145–147, March 2009.

[3] G. M. Ter-Akopian, J. H. Hamilton, Yu. Ts. Oganessian, A. V. Daniel, J. Kormicki, A. V. Ramayya, G. S. Popeko, B. R. S. Babu, Q.-H. Lu, K. Butler-Moore, W.-C. Ma, E. F. Jones, J. K. Deng, D. Shi, J. Kliman, M. Morháč, J. D. Cole, R. Aryaeinejad, N. R. Johnson, I. Y. Lee, and F. K. McGowan. Yields of correlated fragment pairs in spontaneous fission of ^{252}Cf. *Phys. Rev. C*, 55:1146–1161, Mar 1997.

[4] S.-C. Wu, R. Donangelo, J. O. Rasmussen, A. V. Daniel, J. K. Hwang, A. V. Ramayya, and J. H. Hamilton. New determination of the Ba-Mo yield matrix for ^{252}Cf. *Phys. Rev. C*, 62:041601, Aug 2000.

[5] D. C. Biswas and R.K. Choudhury and M. Cinausero and B. Fornal and D.V. Shetty and G. Viesti and D. Fabris and E. Fioretto and M. Lunardon and G. Nebbia and G. Prete and D. Bazzacco and M. DePoli and D.R. Napoli and C.A. Ur and G. Vedovato. Study of the Mo-Ba partition in ^{252}Cf spontaneous fission. *Eur. Phys. J. A*, 7(2):189–195, 2000.

[6] E. Cheifetz, J. B. Wilhelmy, R. C. Jared, and S. G. Thompson. Determination of the Charge and Mass Distribution in the Fission of ^{252}Cf. *Phys. Rev. C*, 4:1913–1926, Nov 1971.

[7] S. Frauendorf and J. Meng. Tilted rotation of triaxial nuclei. *Nuclear Physics A*, 617(2):131 – 147, 1997.

[8] E. Mergel, C.M. Petrache, G. Lo Bianco, H. Hübel, J. Domscheit, D. Roßbach, G. Schönwaßer, N. Nenoff, A. Neußer, A. Görgen, F. Becker, E. Bouchez, M. Houry, A. Hürstel, Y. Le Coz, R. Lucas, Ch. Theisen, W. Korten, A. Bracco, N. Blasi, F. Camera, S. Leoni, F. Hannachi, A. Lopez-Martens, M. Rejmund, D. Gassmann, P. Reiter, P.G. Thirolf, A. Astier, N. Buforn, M. Meyer, N. Redon, and O. Stezowski. Candidates for chiral doublet bands in ^{136}Nd. *Eur. Phys. J. A*, 15(4):417–420, 2002.

[9] C. Vaman, D. B. Fossan, T. Koike, K. Starosta, I. Y. Lee, and A. O. Macchiavelli. Chiral Degeneracy in Triaxial ^{104}Rh. *Phys. Rev. Lett.*, 92:032501, Jan 2004.

[10] J. Timár, P. Joshi, K. Starosta, V.I. Dimitrov, D.B. Fossan, J. Molnár, D. Sohler, R. Wadsworth, A. Algora, P. Bednarczyk, D. Curien, Zs. Dombrádi, G. Duchene, A. Gizon, J. Gizon, D.G. Jenkins, T. Koike, A. Krasznahorkay, E.S. Paul, P.M. Raddon, G. Rainovski, J.N. Scheurer, A.J. Simons, C. Vaman, A.R. Wilkinson, L. Zolnai, and S. Frauendorf. Experimental evidence for chirality in the odd-A ^{105}Rh. *Physics Letters B*, 598(3):178 – 187, 2004.

[11] P. Joshi, D.G. Jenkins, P.M. Raddon, A.J. Simons, R. Wadsworth, A.R. Wilkinson, D.B. Fossan, T. Koike, K. Starosta, C. Vaman, J. Timár, Zs. Dombrádi, A. Krasznahorkay, J. Molnár, D. Sohler, L. Zolnai, A. Algora, E.S. Paul, G. Rainovski, A. Gizon, J. Gizon, P. Bednarczyk, D. Curien, G. Duchêne, and J.N. Scheurer. Stability of chiral geometry in the odd–odd Rh isotopes: spectroscopy of ^{106}Rh. *Physics Letters B*, 595(1):135 – 142, 2004.

[12] P. Joshi., M. P. Carpenter, D. B. Fossan, T. Koike, E. S. Paul, G. Rainovski, K. Starosta, C. Vaman, and R. Wadsworth. Effect of γ Softness on the Stability of Chiral Geometry: Spectroscopy of ^{106}Ag. *Phys. Rev. Lett.*, 98:102501, Mar 2007.

[13] S. J. Zhu, J. H. Hamilton, A. V. Ramayya, P. M. Gore, J. O. Rasmussen, V. Dimitrov, S. Frauendorf, R. Q. Xu, J. K. Hwang, D. Fong, L. M. Yang, K. Li, Y. J. Chen, X. Q. Zhang, E. F. Jones, Y. X. Luo, I. Y. Lee, W. C. Ma, J. D. Cole, M. W. Drigert, M. Stoyer, G. M. Ter-Akopian, and A. V. Daniel. Soft chiral vibrations in ^{106}Mo. *European Physical Journal A Supplement*, 25:459–462, September 2005.

[14] P. Möller., Ragnar Bengtsson, B. Gillis Carlsson, Peter Olivius, and Takatoshi Ichikawa. Global Calculations of Ground-State Axial Shape Asymmetry of Nuclei. *Phys. Rev. Lett.*, 97:162502, Oct 2006.

[15] Y. X. Luo, S. J. Zhu, J. H. Hamilton, J. O. Rasmussen, A. V. Ramayya, C. Goodin, K. Li, J. K. Hwang, D. Almehed, S. Frauendorf, V. Dimitrov, J.-y. Zhang, X. L. Che, Z. Jang, I. Stefanescu, A. Gelberg, G. M. Ter-Akopian, A. V. Daniel, M. A. Stoyer, R. Donangelo, J. D. Cole, and N. J. Stone. Evolution of chirality from γ soft ^{108}Ru to triaxial ^{110,112}Ru. *Physics Letters B*, 670:307–312, January 2009.

[16] G. M. Ter-Akopian, J. H. Hamilton, Yu. Ts. Oganessian, A. V. Daniel, J. Kormicki, A. V. Ramayya, G. S. Popeko, B. R. S. Babu, Q.-H. Lu, K. Butler-Moore, W.-C. Ma, S. Ćwiok, W. Nazarewicz, J. K. Deng, D. Shi, J. Kliman, M. Morhac, J. D. Cole, R. Aryaeinejad, N. R. Johnson, I. Y. Lee, F. K. McGowan, and J. X. Saladin. New spontaneous fission mode for ^{252}Cf: Indication of hyperdeformed ^{144,145,146}Ba at scission. *Phys. Rev. Lett.*, 77:32–35, Jul 1996.

[17] G. M. Ter-Akopian, J. H. Hamilton, Yu. Ts. Oganessian, J. Kormicki, G. S. Popeko, A. V. Daniel, A. V. Ramayya, Q. Lu, K. Butler-Moore, W. C. Ma, J. K. Deng, D. Shi, J. Kliman, V. Polhorsky, M. Morhac, W. Greiner, A. Sandelescu, J. D. Cole,

R. Aryaeinejad, N. R. Johnson, I. Y. Lee, and F. K. McGowan. Neutron multiplicities and yields of correlated Zr-Ce and Mo-Ba fragment paris in spontaneous fission of ^{252}Cf. *Phys. Rev. Lett.*, 73:1477–1480, Sep 1994.

[18] Yu.V. Pyatkov, V.V. Pashkevich, Yu.E. Penionzhkevich, V.G. Tishchenko, A.V. Unzhakova, H.-G. Ortlepp, P. Gippner, C.-M. Herbach, and W. Wagner. Manifestation of clustering in the ^{252}Cf(sf) and ^{249}Cf(n$_{th}$,f) reactions. *Nuclear Physics A*, 624(2):140 – 156, 1997.

[19] R. Donangelo, J. O. Rasmussen, M. A. Stoyer, and J. H. Hamilton. Cluster aspects of ^{252}Cf spontaneous fission. *International Journal of Modern Physics E*, 07(06):669–676, 1998.

[20] Ulrich Brosa, Siegfried Grossmann, and Andreas Müller. Nuclear scission. *Physics Reports*, 197(4):167 – 262, 1990.

[21] N. Schultz. (privite communication) in ref. [4].

[22] S.-C. Wu, R. Donangelo, J. O. Rasmussen, A. V. Daniel, J. K. Hwang, A. V. Ramayya, and J. H. Hamilton. Resolution of complex γ spectra from triple-coincidence data: Ba-Mo split in ^{252}Cf spontaneous fission. *Nuclear Instruments and Methods in Physics Research A*, 480:776–781, March 2002.

[23] C. Goodin, D. Fong, J. K. Hwang, A. V. Ramayya, J. H. Hamilton, K. Li, Y. X. Luo, J. O. Rasmussen, S. C. Wu, M. A. Stoyer, T. N. Ginter, S. J. Zhu, R. Donangelo, G. M. Ter-Akopian, A. V. Daniel, G. S. Popeko, A. M. Rodin, and A. S. Fomichev. New results for the intensity of bimodal fission in barium channels of the spontaneous fission of ^{252}Cf. *Phys. Rev. C*, 74:017309, Jul 2006.

[24] Ramayya, A. V and Hwang, J. K. and Hamilton, J. H. Binary and ternary spontaneous fission in ^{252}Cf. *Romanian Reports in Physics*, pages 595–608, 2007.

[25] Fujia Yang and Joseph H. Hamilton. *Modern Atomic and Nuclear Physics*. World Scientific, Hackensack, NJ, revised edition, 2010.

[26] Kenneth S. Krane. *Introductory Nuclear Physics*. John Wiley & Sons, Inc., New York, 1988.

[27] C. J. Chiara, J. J. Carroll, M. P. Carpenter, J. P. Greene, D. J. Hartley, R. V. F. Janssens, G. J. Lane, J. C. Marsh, D. A. Matters, M. Polasik, J. Rzadkiewicz, D. Seweryniak, S. Zhu, S. Bottoni, A. B. Hayes, and S. A. Karamian. Isomer depletion as experimental evidence of nuclear excitation by electron capture. *Nature*, 554:216, 2018.

[28] Richard. A. Dunlap. *The Physics of Nuclei and Particles*. Brooks/Cole, 2$^{\mathrm{nd}}$ edition, 2004.

[29] Judah M. Eisenberg and Walter Greiner. *Nuclear Models*, volume 1. North-Holland Physics Publishing, Amsterdam, 3$^{\mathrm{rd}}$ edition, 1987.

[30] R. Casten. *Nuclear Structure From a Simple Perspective*, volume 13 of *Oxford Studies in Nuclear Physics*. Oxford University Press, New York, 1990.

[31] P. O. Lipas. Perturbation corrections to energies of collective states in deformed even nuclei. *Nuclear Physics*, 39:468 – 478, 1962.

[32] Leo Louis Riedinger. *Studies of the Collective States in ^{152}Gd, ^{152}Sm, and ^{154}Gd*. PhD thesis, Vanderbilt University, Nashville, TN, 1969.

[33] Eugene R. Marshalek. Self-Consistent Perturbation of Hartree-Fock-Bogoliubov Equations and Nuclear Rotational Spectra. II. *Physical Review*, 158:993–1010, Jun 1967.

[34] J. B. Gupta. The nature of $K^{\pi} = 0_2^+, 0_3^+$ bands in ^{158}Gd. *Nuclear Physics A*, 990:162 – 182, 2019.

[35] T. Kibédi, T. W. Burrows, M. B. Trzhaskovskaya, P. M. Davidson, and C. W. Nestor. Evaluation of theoretical conversion coefficients using BrIcc. *Nuclear Instruments and Methods in Physics Research Section A: Accelerators, Spectrometers, Detectors and Associated Equipment*, 589(2):202 – 229, 2008.

[36] Howard Matis. *Nuclear Science—A Guide to the Nuclear Science Wall Chart*. 2019 Contemporary Physics Education Project (CPEP), Berkeley, California, 5^{th} edition, 2019.

[37] Ramamurti Shankar. *Principles of Quantum Mechanics*. Springer, New York, 2^{nd} edition, 1980.

[38] G. E. Brown, J. A. Evans, and D. J. Thouless. Vibrations of spherical nuclei. *Nuclear Physics*, 24(1):1 – 17, 1961.

[39] John David Jackson. *Classical Electrodynamics*. John Wiley & Sons, Inc., 3^{rd} edition, 1999.

[40] H. Frauenfelder, R. M. Steffen, S. R. de Groot, H. A. Tolhoek, and W. J. Huiskamp. Angular distribution of nuclear radiation. In K. Siegbahn, editor, *Alpha-, Beta- and Gamma-Ray Spectroscopy*, volume II, chapter XIX, pages 997–1195. North-Holland Publishing Company, 1965.

[41] Aage Bohr and Ben R. Mottelson. *Nuclear Structure*. W. A. Benjamin Inc., New York, 1975.

[42] D. C. Radford. ESCL8R and LEVIT8R: software for interactive graphical analysis of HPGe coincidence data sets. Technical Report TASCC-P-94-29, Canada. At. Energy Comm., Chalk River, Ontario, Nov 1994.

[43] Enhong Wang. *Studies of Neutron-rich Nuclei from ^{252}Cf and $^{238}U+^{9}Be$ Fission Fragments*. PhD thesis, Vanderbilt University, Nashville, TN, 2015.

[44] Nathan Brewer. *Measurements from the Prompt and Delayed Radiation of Fission Fragments: Deformation Properties of Neutron Rich Nuclei*. PhD thesis, Vanderbilt University, Nashville, TN, 2013.

[45] A. Navin, M. Rejmund, S. Bhattacharyya, R. Palit, G.H. Bhat, J.A. Sheikh, A. Lemasson, S. Bhattacharya, M. Caamaño, E. Clément, O. Delaune, F. Farget, G. de France, and B. Jacquot. Evolution of triaxial shapes at large isospin: Rh isotopes. *Physics Letters B*, 767:480 – 484, 2017.

[46] I. Hamamoto. Oblate deformation of light neutron-rich even-even nuclei. *Phys. Rev. C*, 89:057301, May 2014.

[47] I. Hamamoto and B R. Mottelson. Further examination of prolate-shape dominance in nuclear deformation. *Phys. Rev. C*, 79:034317, Mar 2009.

[48] A.S. Davydov and G.F. Filippov. Rotational states in even atomic nuclei. *Nuclear Physics*, 8:237 – 249, 1958.

[49] L. Wilets and M. Jean. Surface Oscillations in Even-Even Nuclei. *Phys. Rev.*, 102:788–796, May 1956.

[50] N.V. Zamfir and R.F. Casten. Signatures of γ softness or triaxiality in low energy nuclear spectra. *Physics Letters B*, 260(3):265 – 270, 1991.

[51] Y. Toh, C. J. Chiara, E. A. McCutchan, W. B. Walters, R. V. F. Janssens, M. P. Carpenter, S. Zhu, R. Broda, B. Fornal, B. P. Kay, F. G. Kondev, W. Królas, T. Lauritsen, C. J. Lister, T. Pawłat, D. Seweryniak, I. Stefanescu, N. J. Stone, J. Wrzesiński, K. Higashiyama, and N. Yoshinaga. Evidence for rigid triaxial deformation at low energy in ^{76}Ge. *Phys. Rev. C*, 87:041304, Apr 2013.

[52] E. A. McCutchan, Dennis Bonatsos, N. V. Zamfir, and R. F. Casten. Staggering in γ-band energies and the transition between different structural symmetries in nuclei. *Phys. Rev. C*, 76:024306, Aug 2007.

[53] V. I. Dimitrov, S. Frauendorf, and F. Dönau. Chirality of Nuclear Rotation. *Phys. Rev. Lett.*, 84:5732–5735, Jun 2000.

[54] K. Starosta, T. Koike, C. J. Chiara, D. B. Fossan, D. R. LaFosse, A. A. Hecht, C. W. Beausang, M. A. Caprio, J. R. Cooper, R. Krücken, J. R. Novak, N. V. Zamfir, K. E. Zyromski, D. J. Hartley, D. L. Balabanski, Jing-ye Zhang, S. Frauendorf, and V. I. Dimitrov. Chiral Doublet Structures in Odd-Odd $N = 75$ Isotones: Chiral Vibrations. *Phys. Rev. Lett.*, 86:971–974, Feb 2001.

[55] I. Kuti, Q. B. Chen, J. Timár, D. Sohler, S. Q. Zhang, Z. H. Zhang, P. W. Zhao, J. Meng, K. Starosta, T. Koike, E. S. Paul, D. B. Fossan, and C. Vaman. Multiple Chiral Doublet Bands of Identical Configuration in ^{103}Rh. *Phys. Rev. Lett.*, 113:032501, Jul 2014.

[56] J.A. Sheikh, G.H. Bhat, Y. Sun, and R. Palit. Multi-phonon γ-vibrational bands in odd-mass nuclei studied by triaxial projected shell model approach. *Physics Letters B*, 688(4):305 – 308, 2010.

[57] G.H. Bhat, J.A. Sheikh, W.A. Dar, S. Jehangir, R. Palit, and P.A. Ganai. Triaxial projected shell model description of high-spin band-structures in ^{103,105}Rh isotopes. *Physics Letters B*, 738:218 – 222, 2014.

[58] G.H. Bhat, J.A. Sheikh, and R. Palit. Triaxial projected shell model study of chiral rotation in odd–odd nuclei. *Physics Letters B*, 707(2):250 – 254, 2012.

[59] Stefan Frauendorf. Spontaneous symmetry breaking in rotating nuclei. *Rev. Mod. Phys.*, 73:463–514, Jun 2001.

[60] T. Koike, K. Starosta, and I. Hamamoto. Chiral Bands, Dynamical Spontaneous Symmetry Breaking, and the Selection Rule for Electromagnetic Transitions in the Chiral Geometry. *Phys. Rev. Lett.*, 93:172502, Oct 2004.

[61] S.Y. Wang, B. Qi, L. Liu, S.Q. Zhang, H. Hua, X.Q. Li, Y.Y. Chen, L.H. Zhu, J. Meng, S.M. Wyngaardt, P. Papka, T.T. Ibrahim, R.A. Bark, P. Datta, E.A. Lawrie, J.J. Lawrie, S.N.T. Majola, P.L. Masiteng, S.M. Mullins, J. Gál, G. Kalinka, J. Molnár, B.M. Nyakó, J. Timár, K. Juhász, and R. Schwengner. The first candidate for chiral nuclei in the A$\sim$80 mass region: ^{80}Br. *Physics Letters B*, 703(1):40 – 45, 2011.

[62] Takeshi Koike, S.kinoshita , Y.ma , Y.miura , K.shirotori , H.tamura , M.ukai , Tomohiko Suzuki, Takasi Endo, Masaki Fujita, Yukari Miyashita, M.ohguma , N.sato , T.shinozuka , M.tateoka , T.wakui , A.yamazaki , Tomonori Fukuchi, Janos Timar, and Y.y.fu . Chirality in the mass 80 region: ^{79}Kr. *International Journal of Modern Physics E*, 20:520–525, 05 2011.

[63] J. A. Alcántara-Núñez, J. R. B. Oliveira, E. W. Cybulska, N. H. Medina, M. N. Rao, R. V. Ribas, M. A. Rizzutto, W. A. Seale, F. Falla-Sotelo, K. T. Wiedemann, V. I. Dimitrov, and S. Frauendorf. Magnetic dipole and electric quadrupole rotational structures and chirality in ^{105}Rh. *Phys. Rev. C*, 69:024317, Feb 2004.

[64] P. Joshi, A. R. Wilkinson, T. Koike, D. B. Fossan, S. Finnigan, E. S. Paul, P. M. Raddon, G. Rainovski, K. Starosta, A. J. Simons, C. Vaman, and R. Wadsworth. First evidence for chirality in Tc isotopes: Spectroscopy of ^{100}Tc. *European Physical Journal A*, 24:23–29, April 2005.

[65] P. Joshi, M. P. Carpenter, D. B. Fossan, T. Koike, E. S. Paul, G. Rainovski, K. Starosta, C. Vaman, and R. Wadsworth. Effect of γ Softness on the Stability of Chiral Geometry: Spectroscopy of ^{106}Ag. *Phys. Rev. Lett.*, 98:102501, Mar 2007.

[66] T. Suzuki, G. Rainovski, T. Koike, T. Ahn, M. P. Carpenter, A. Costin, M. Danchev, A. Dewald, R. V. F. Janssens, P. Joshi, C. J. Lister, O. Möller, N. Pietralla, T. Shinozuka, J. Timár, R. Wadsworth, C. Vaman, and S. Zhu. Lifetime measurement of candidate chiral doublet bands in the ^{103,104}Rh isotopes with the recoil-distance Doppler-shift method in inverse kinematics. *Phys. Rev. C*, 78:031302, Sep 2008.

[67] J. Sethi, R. Palit, S. Saha, T. Trivedi, G. H. Bhat, J. A. Sheikh, P. Datta, J. J. Carroll, S. Chattopadhyay, R. Donthi, U. Garg, S. Jadhav, H. C. Jain, S. Karamian, S. Kumar, M. S. Litz, D. Mehta, B. S. Naidu, Z. Naik, S. Sihotra, and P. M. Walker. Structure of nearly degenerate dipole bands in ^{108}Ag. *Physics Letters B*, 725:85–91, August 2013.

[68] D. Tonev, M. S. Yavahchova, N. Goutev, G. de Angelis, P. Petkov, R. K. Bhowmik, R. P. Singh, S. Muralithar, N. Madhavan, R. Kumar, M. Kumar Raju, J. Kaur, G. Mohanto, A. Singh, N. Kaur, R. Garg, A. Shukla, Ts. K. Marinov, and S. Brant. Candidates for Twin Chiral Bands in ^{102}Rh. *Phys. Rev. Lett.*, 112:052501, Feb 2014.

[69] E. O. Lieder, R. M. Lieder, R. A. Bark, Q. B. Chen, S. Q. Zhang, J. Meng, E. A. Lawrie, J. J. Lawrie, S. P. Bvumbi, N. Y. Kheswa, S. S. Ntshangase, T. E. Madiba, P. L. Masiteng, S. M. Mullins, S. Murray, P. Papka, D. G. Roux, O. Shirinda, Z. H. Zhang, P. W. Zhao, Z. P. Li, J. Peng, B. Qi, S. Y. Wang, Z. G. Xiao, and C. Xu. Resolution of Chiral Conundrum in ^{106}Ag: Doppler-Shift Lifetime Investigation. *Phys. Rev. Lett.*, 112:202502, May 2014.

[70] N. Rather, P. Datta, S. Chattopadhyay, S. Rajbanshi, A. Goswami, G. H. Bhat, J. A. Sheikh, S. Roy, R. Palit, S. Pal, S. Saha, J. Sethi, S. Biswas, P. Singh, and H. C. Jain. Exploring the Origin of Nearly Degenerate Doublet Bands in ^{106}Ag. *Phys. Rev. Lett.*, 112:202503, May 2014.

[71] S. Zhu, U. Garg, B. K. Nayak, S. S. Ghugre, N. S. Pattabiraman, D. B. Fossan, T. Koike, K. Starosta, C. Vaman, R. V. F. Janssens, R. S. Chakrawarthy, M. Whitehead, A. O. Macchiavelli, and S. Frauendorf. A Composite Chiral Pair of Rotational Bands in the Odd-*A* Nucleus ^{135}Nd. *Phys. Rev. Lett.*, 91:132501, Sep 2003.

[72] E. Grodner, J. Srebrny, A. A. Pasternak, I. Zalewska, T. Morek, Ch. Droste, J. Mierzejewski, M. Kowalczyk, J. Kownacki, M. Kisieliński, S. G. Rohoziński, T. Koike, K. Starosta, A. Kordyasz, P. J. Napiorkowski, M. Woli ńska Cichocka, E. Ruchowska, W. Płóciennik, and J. Perkowski. ^{128}Cs as the Best Example Revealing Chiral Symmetry Breaking. *Phys. Rev. Lett.*, 97:172501, Oct 2006.

[73] S. Mukhopadhyay, D. Almehed, U. Garg, S. Frauendorf, T. Li, P. V. Madhusudhana Rao, X. Wang, S. S. Ghugre, M. P. Carpenter, S. Gros, A. Hecht, R. V. F. Janssens, F. G. Kondev, T. Lauritsen, D. Seweryniak, and S. Zhu. From Chiral Vibration to Static Chirality in ^{135}Nd. *Phys. Rev. Lett.*, 99:172501, Oct 2007.

[74] D. L. Balabanski, M. Danchev, D. J. Hartley, L. L. Riedinger, O. Zeidan, Jing-ye Zhang, C. J. Barton, C. W. Beausang, M. A. Caprio, R. F. Casten, J. R. Cooper, A. A. Hecht, R. Krücken, J. R. Novak, N. V. Zamfir, and K. E. Zyromski. Possible assignment of chiral twin bands in ^{188}Ir. *Phys. Rev. C*, 70:044305, Oct 2004.

[75] P. L. Masiteng, E. A. Lawrie, T. M. Ramashidzha, R. A. Bark, B. G. Carlsson, J. J. Lawrie, R. Lindsay, F. Komati, J. Kau, P. Maine, S. M. Maliage, I. Matamba, S. M. Mullins, S. H. T. Murray, K. P. Mutshena, A. A. Pasternak, I. Ragnarsson, D. G. Roux, J. F. Sharpey-Schafer, O. Shirinda, and P. A. Vymers. Close near-degeneracy in a pair of four-quasiparticle bands in ^{194}Tl. *Physics Letters B*, 719:83–88, February 2013.

[76] A. Guessous, N. Schulz, W. R. Phillips, I. Ahmad, M. Bentaleb, J. L. Durell, M. A. Jones, M. Leddy, E. Lubkiewicz, L. R. Morss, R. Piepenbring, A. G. Smith, W. Ur-

ban, and B. J. Varley. Harmonic Two-Phonon γ-Vibrational State in Neutron-Rich ^{106}Mo. *Phys. Rev. Lett.*, 75:2280–2283, Sep 1995.

[77] A. Guessous, N. Schulz, M. Bentaleb, E. Lubkiewicz, J. L. Durell, C. J. Pearson, W. R. Phillips, J. A. Shannon, W. Urban, B. J. Varley, I. Ahmad, C. J. Lister, L. R. Morss, K. L. Nash, C. W. Williams, and S. Khazrouni. Prompt γ-ray spectroscopy of the ^{104}Mo and ^{108}Mo fission fragments. *Phys. Rev. C*, 53:1191–1196, Mar 1996.

[78] V. Dimitrov, F. Dönau, and S. Frauendorf. Left-Handed Nuclei. *AIP Conference Proceedings*, 656(1):151–159, 2003.

[79] E. F. Jones, P. M. Gore, S. J. Zhu, J. H. Hamilton, A. V. Ramayya, J. K. Hwang, R. Q. Xu, L. M. Yang, K. Li, Z. Jiang, Z. Zhang, S. D. Xiao, X. Q. Zhang, W. C. Ma, J. D. Cole, M. W. Drigert, I. Y. Lee, J. O. Rasmussen, Y. X. Luo, and M. A. Stoyer. Collective bands in ^{104,106,108}Mo. *Physics of Atomic Nuclei*, 69:1198–1203, July 2006.

[80] B. D. Kern, K. Sistemich, W. D. Lauppe, and H. Lawin. The Beta decay of ^{104}Nb and the level scheme of ^{104}Mo. *Z. Phys. A*, 306:161–170, 1982.

[81] Zhu Sheng jiang (S J Zhu), Wang Mu-ge, J H Hamilton, A V Ramayya, B R S Babu, W C Ma, Long Gui-lu, Deng Jing-kang, Zhu Ling-yan, Li Ming, T N Ginter, J Komicki, J D Cole, R Aryaeinejad, Y K Dardenne, M W Drigert, J O Rasmussen, Ts Yu Oganessian, M A Stoyer, S Y Chu, K E Gregorich, M F Mohar, S G Prussin, I Y Lee, N R Johnson, and F K McGowan. Reflection Asymmetric Shapes in the Neutron-Rich ^{140,143}Ba Isotopes. *Chinese Physics Letters*, 14(8):569–572, aug 1997.

[82] W. Urban et al. Octupole correlations in neutron-rich, even-even barium isotopes. *Nucl. Phys. A*, 613:107–131, 1997.

[83] Venkova, Ts., Porquet, M. -G., Deloncle, I., Petkov, P., Astier, A., Prévost, A., Azaiez, F., Bogachev, A., Buta, A., Curien, D., Dorvaux, O., Duchêne, G., Durell, J.,

Gall, B. J. P., Houry, M., Khalfallah, F., Lucas, R., Meyer, M., Piqueras, I., Redon, N., Roach, A., Rousseau, M., Stézowski, O., and Theisen, Ch. New high-spin states of $^{142}_{58}$Ce and $^{140}_{56}$Ba from fusion-fission reactions: Proton excitations in the N = 84 isotones. *Eur. Phys. J. A*, 34(4):349–353, 2007.

[84] Yang L. M., Zhu Sheng-Jiang, Li Ke, J H Hamilton, A V Ramayya, J K Hwang, X Q Zhang, Zhu Ling-Yan, Gan Cui-Yun, M Sakhaee, Long Gui-Lu, Xu Rui-Qing, Zhang Zheng, Jiang Zhuo, Jon Myong-Gil, W C Ma, B R S Babu, J Komicki, E F Jones, J D Cole, R Aryaeinejad, M W Drigert, I Y Lee, J O Rasmussen, M A Stoyer, G M Ter-Akopian, and A V Daniel. Collective Bands in Neutron-Rich ^{104}Mo Nucleus. *Chinese Physics Letters*, 18(1):24–26, Jan 2001.

[85] H. Hua, C. Y. Wu, D. Cline, A. B. Hayes, R. Teng, R. M. Clark, P. Fallon, A. Goergen, A. O. Macchiavelli, and K. Vetter. Triaxiality and the aligned $h_{11/2}$ neutron orbitals in neutron-rich Zr and Mo isotopes. *Phys. Rev. C*, 69:014317, Jan 2004.

[86] S. J. Zhu, E. H. Wang, J. H. Hamilton, A. V. Ramayya, Y. X. Liu, N. T. Brewer, Y. X. Luo, J. O. Rasmussen, Z. G. Xiao, Y. Huang, G. M. Ter-Akopian, and Ts. Oganessian. Coexistence of reflection asymmetric and symmetric shapes in ^{144}Ba. *Phys. Rev. Lett.*, 124:032501, Jan 2020.

[87] S. Biswas, R. Palit, S. Frauendorf, U. Garg, W. Li, G. H. Bhat, J. A. Sheikh, J. Sethi, S. Saha, Purnima Singh, D. Choudhury, J. T. Matta, A. D. Ayangeakaa, W. Dar, V. Singh, and S. Sihotra. Longitudinal Wobbling in ^{133}La, 2017.

[88] Peter Ring and Peter Schuck. *The Nuclear Many-Body Problem*. Springer, Verlag Berlin Heidelberg, 1980.

[89] K. Hara and S. Iwasaki. On the quantum number projection: (I). General theory. *Nuclear Physics A*, 332(1):61 – 68, 1979.

[90] K. Hara and S. Iwasaki. On the quantum number projection: (iii). simultaneous j- and n-projection. *Nuclear Physics A*, 348(2):200 – 220, 1980.

[91] S. N. T. Majola, D. J. Hartley, L. L. Riedinger, J. F. Sharpey-Schafer, J. M. Allmond, C. Beausang, M. P. Carpenter, C. J. Chiara, N. Cooper, D. Curien, B. J. P. Gall, P. E. Garrett, R. V. F. Janssens, F. G. Kondev, W. D. Kulp, T. Lauritsen, E. A. McCutchan, D. Miller, J. Piot, N. Redon, M. A. Riley, J. Simpson, I. Stefanescu, V. Werner, X. Wang, J. L. Wood, C.-H. Yu, and S. Zhu. Observation of γ vibrations and alignments built on non-ground-state configurations in ^{156}Dy. *Phys. Rev. C*, 91:034330, Mar 2015.

[92] Yang Sun, Kenji Hara, Javid A. Sheikh, Jorge G. Hirsch, Victor Velázquez, and Mike Guidry. Multiphonon γ-vibrational bands and the triaxial projected shell model. *Phys. Rev. C*, 61:064323, May 2000.

[93] Sven Gösta Nilsson, Chin Fu Tsang, Adam Sobiczewski, Zdzislaw Szymański, Slawomir Wycech, Christer Gustafson, Inger-Lena Lamm, Peter Möller, and Björn Nilsson. On the nuclear structure and stability of heavy and superheavy elements. *Nuclear Physics A*, 131(1):1–66, 1969.

[94] S. Jehangir *e*t al. (in preparation).

[95] J. A. Sheikh, G. H. Bhat, Y. Sun, G. B. Vakil, and R. Palit. Triaxial projected shell model study of γ-vibrational bands in even-even Er isotopes. *Phys. Rev. C*, 77:034313, Mar 2008.

[96] J. A. Sheikh, G. H. Bhat, Yan-Xin Liu, Fang-Qi Chen, and Yang Sun. Mixing of quasiparticle excitations and γ vibrations in transitional nuclei. *Phys. Rev. C*, 84:054314, Nov 2011.

[97] C. L. Zhang, G. H. Bhat, W. Nazarewicz, J. A. Sheikh, and Yue Shi. Theoretical study of triaxial shapes of neutron-rich Mo and Ru nuclei. *Phys. Rev. C*, 92:034307, Sep 2015.

[98] G. H. Bhat, J. A. Sheikh, Y. Sun, and R. Palit. Unified description of rotational-, γ-, and quasiparticle-band structures in neutron-rich mass $\sim$110 region. *Nucl. Phys.*, A947:127–141, March 2016.

[99] J. A. Sheikh, G. H. Bhat, Waheed A Dar, Sheikh Jehangir, and Prince A Ganai. Microscopic nuclear structure models and methods: chiral symmetry, wobbling motion andγ–bands. *Physica Scripta*, 91(6):063015, may 2016.

[100] F.R. Xu, P.M. Walker, J.A. Sheikh, and R. Wyss. Multi-quasiparticle potential-energy surfaces. *Physics Letters B*, 435(3):257 – 263, 1998.

[101] W. Nazarewicz, J. Dudek, R. Bengtsson, T. Bengtsson, and I. Ragnarsson. Microscopic study of the high-spin behaviour in selected a $\simeq$ 80 nuclei. *Nuclear Physics A*, 435(2):397 – 447, 1985.

[102] H.C. Pradhan, Y. Nogami, and J. Law. Study of approximations in the nuclear pairing-force problem. *Nuclear Physics A*, 201(2):357 – 368, 1973.

[103] Darleane C. Hoffman, G. P. Ford, J. P. Balagna, and L. R. Veeser. Neutron multiplicity measurements of cf and fm isotopes. *Phys. Rev. C*, 21:637–646, Feb 1980.

[104] C. Goodin, D. Fong, J. K. Hwang, A. V. Ramayya, J. H. Hamilton, K. Li, Y. X. Luo, J. O. Rasmussen, S. C. Wu, M. A. Stoyer, T. N. Ginter, S. J. Zhu, R. Donangelo, G. M. Ter-Akopian, A. V. Daniel, G. S. Popeko, A. M. Rodin, and A. S. Fomichev. New results for the intensity of bimodal fission in barium channels of the spontaneous fission of ^{252}Cf. *Phys. Rev. C*, 74:017309, Jul 2006.

[105] V.V. Pashkevich. On the asymmetric deformation of fissioning nuclei. *Nuclear Physics A*, 169(2):275–293, 1971.

[106] E. K. Hulet, J. F. Wild, R. J. Dougan, R. W. Lougheed, J. H. Landrum, A. D. Dougan, M. Schadel, R. L. Hahn, P. A. Baisden, C. M. Henderson, R. J. Dupzyk, K. Sümmerer, and G. R. Bethune. Bimodal symmetric fission observed in the heaviest elements. *Phys. Rev. Lett.*, 56:313–316, Jan 1986.

[107] T. Rząca-Urban, W. Urban, A. G. Smith, I. Ahmad, and A. Syntfeld-Każuch. Unexpected $5/2^-$ spin of the ground state in ^{147}Ba: No octupole deformation in ground states of odd-*A* Ba isotopes. *Phys. Rev. C*, 87:031305, Mar 2013.

[108] G. S. Simpson, W. Urban, J. A. Pinston, J. C. Angelique, I. Deloncle, H. R. Faust, J. Genevey, U. Köster, T. Materna, R. Orlandi, A. Scherillo, A. G. Smith, J. F. Smith, T. Rząca-Urban, I. Ahmad, and J. P. Greene. Near-yrast structure of $n = 93$ neutron-rich lanthanide nuclei. *Phys. Rev. C*, 81:024313, Feb 2010.

[109] J. Marcellino, E. H. Wang, C. J. Zachary, J. H. Hamilton, A. V. Ramayya, G. H. Bhat, J. A. Sheikh, A. C. Dai, W. Y. Liang, F. R. Xu, J. K. Hwang, N. T. Brewer, Y. X. Luo, J. O. Rasmussen, S. J. Zhu, G. M. Ter-Akopian, and Yu. Ts. Oganessian. One- and two-phonon γ-vibrational bands in neutron-rich ^{107}Mo. *Phys. Rev. C*, 96:034319, Sep 2017.

[110] W. Urban, Ch. Droste, T. Rząca-Urban, A. Złomaniec, J. L. Durell, A. G. Smith, B. J. Varley, and I. Ahmad. Near-yrast structure of the ^{109}Mo nucleus. *Phys. Rev. C*, 73:037302, Mar 2006.

[111] W. Urban, T. Rząca-Urban, A. Syntfeld-Każuch, A. G. Smith, and I. Ahmad. Band structure of ^{149}Ce. *Phys. Rev. C*, 86:017301, Jul 2012.

[112] W. Urban, J. A. Pinston, T. Rząca-Urban, E. Wolska, J. Genevey, G. S. Simpson, A. G. Smith, J. L. Durell, B. Varley, and I. Ahmad. Mapping neutron levels in the $a \sim 100$ region: The $\nu 3/2^{+}$ [411] band in ^{103}Zr. *Phys. Rev. C*, 79:067301, Jun 2009.

[113] W. Urban, T. Rząca-Urban, J. A. Pinston, J. L. Durell, W. R. Phillips, A. G. Smith, B. J. Varley, I. Ahmad, and N. Schulz. Near-yrast, medium-spin structure of the ^{107}Mo nucleus. *Phys. Rev. C*, 72:027302, Aug 2005.

[114] H. B. Ding, S. J. Zhu, J. H. Hamilton, A. V. Ramayya, J. K. Hwang, K. Li, Y. X. Luo, J. O. Rasmussen, I. Y. Lee, C. T. Goodin, X. L. Che, Y. J. Chen, and M. L. Li. Identification of band structures and proposed one- and two-phonon γ-vibrational bands in ^{105}Mo. *Phys. Rev. C*, 74:054301, Nov 2006.

[115] Y. X. Luo, J. O. Rasmussen, J. H. Hamilton, A. V. Ramayya, S. Frauendorf, J. K. Hwang, N. J. Stone, S. J. Zhu, N. T. Brewer, E. Wang, I. Y. Lee, G. M. Ter-Akopian, S. H. Liu, A. V. Daniel, Y. T. Oganessian, M. A. Stoyer, R. Donangelo, W. C. Ma, J. D. Cole, Y. Shi, and F. R. Xu. New Insights Into the Nuclear Structure in Neutron-Rich ^{112,114,115,116,117,118}Pd. In J. H. Hamilton and V. Ramayya Akunuri, editors, *Fission and Properties of Neutron-Rich Nuclei - Proceedings of the Fifth International Conference on ICFN5. Edited by Hamilton Joseph H and Ramayya Akunuri V. Published by World Scientific Publishing Co. Pte. Ltd., 2014. ISBN #9789814525435, pp. 49-57*, pages 49–57, September 2014.

[116] Y. X. Luo, J. O. Rasmussen, A. V. Ramayya, J. H. Hamilton, X. Q. Zhang, J. K. Hwang, C. J. Beyer, J. Kormicki, G. M. Ter-Akopian, Yu. Ts. Oganessian, A. V. Daniel, K. E. Gregorich, T. N. Ginter, P. Zielinski, C. M. Folden, I. Y. Lee, P. Fallon, A. Macchiavelli, R. Donangelo, M. A. Stoyer, S. Asztalos, and S. C. Wu. Fission γ spectra and levels in ^{139}Ba. *Physical Review C*, 64:054306, Oct 2001.

[117] B. Moon, C.-B. Moon, P.-A. Söderström, A. Odahara, R. Lozeva, B. Hong, F. Browne, H. S. Jung, P. Lee, C. S. Lee, A. Yagi, C. Yuan, S. Nishimura, P. Doornenbal, G. Lorusso, T. Sumikama, H. Watanabe, I. Kojouharov, T. Isobe, H. Baba, H. Sakurai, R. Daido, Y. Fang, H. Nishibata, Z. Patel, S. Rice, L. Sinclair, J. Wu, Z. Y. Xu, R. Yokoyama, T. Kubo, N. Inabe, H. Suzuki, N. Fukuda, D. Kameda, H. Takeda, D. S. Ahn, Y. Shimizu, D. Murai, F. L. Bello Garrote, J. M. Daugas, F. Didierjean, E. Ideguchi, T. Ishigaki, S. Morimoto, M. Niikura, I. Nishizuka, T. Komatsubara, Y. K. Kwon, and K. Tshoo. Nuclear structure and β-decay schemes for Te nuclides beyond $N = 82$. *Phys. Rev. C*, 95:044322, Apr 2017.

[118] A. C. Wahl. Nuclear-Charge Distribution and Delayed-Neutron Yields for Thermal-Neutron-Induced Fission of ^{235}U, ^{233}U, and ^{239}Pu and for Spontaneous Fission of ^{252}Cf. *Atomic Data and Nuclear Data Tables*, 39:1, 1988.

[119] Yu. Khazov, I. Mitropolsky, and A. Rodionov. Nuclear data sheets for a = 131. *Nuclear Data Sheets*, 107(11):2715 – 2930, 2006.

[120] C. Gautherin, M. Houry, W. Korten, Y. Le Coz, R. Lucas, X.H. Phan, Ch. Theisen, Ch. Badimon, G. Barreau, T.P. Doan, G. Pedemay, G. Bélier, M. Girod, V. Méot, S. Peru, A. Astier, L. Ducroux, M. Meyer, and N. Redon. New isomeric states in ^{152,154,156}Nd produced by spontaneous fission of ^{252}Cf. *Eur. Phys. J. A*, 1(4):391–397, 1998.

[121] W. Urban, J. A. Pinston, G. S. Simpson, A. G. Smith, J. F. Smith, T. Rząca-Urban, and I. Ahmad. The $11/2^{-}[505]$ neutron extruder orbital in ^{159}Sm. *Phys. Rev. C*, 80:037301, Sep 2009.

[122] G. S. Simpson, W. Urban, J. Genevey, R. Orlandi, J. A. Pinston, A. Scherillo, A. G. Smith, J. F. Smith, I. Ahmad, and J. P. Greene. Two-quasiparticle isomers and bands of ^{154,156}Nd and ^{156,158,160}Sm. *Phys. Rev. C*, 80:024304, Aug 2009.

[123] B. Musangu, E. H. Wang, J. H. Hamilton, C. J. Zachary, A Thibeault, J. M. Eldridge, A. V. Ramayya, W. H. Brantley, J. O. Rasmussen, Y. X. Luo, G. M. Ter-Akopian, Yu. Ts. Oganessian, and S. J. Zhu. New measurement of Zr-Ce yields matrix for ^{252}Cf. In J. H. Hamilton, A. V. Ramayya, and P. Talou, editors, *Proceedings of the Sixth International Conference on Fission and Properties of Neutron-Rich Nuclei*, pages 255–259, Singapore, 2017. World Scientific.

[124] J. H. Hamilton, A. V. Ramayya, J. K. Hwang, S. J. Greiner, W.and Zhu, A. Sandelescu, A. Floresscu, J. Kormicki, G. Ter-Akopian, Y. Oganessian, A. V. Daniel, G. S. Popeko, J. Kliman, M. Morhac, J. D. Cole, R. Aryaeinejad, M. W. Drigert, W. E. Collins, W. C. Ma, E. F. Jones, L. K. Peker, P. M. Gore, G. Drafta, B. R. S. Babu, G. Wang, and J. K. Deng. Cold spontaneous fission processes of ^{252} Cf and the structure of neutron rich Ba and La nuclei. *Acta Physica Slovaca*, pages 31–42, Dec 1998.

[125] B. Bucher, S. Zhu, C. Y. Wu, R. V. F. Janssens, D. Cline, A. B. Hayes, M. Albers, A. D. Ayangeakaa, P. A. Butler, C. M. Campbell, M. P. Carpenter, C. J. Chiara, J. A. Clark, H. L. Crawford, M. Cromaz, H. M. David, C. Dickerson, E. T. Gregor, J. Harker, C. R. Hoffman, B. P. Kay, F. G. Kondev, A. Korichi, T. Lauritsen, A. O. Macchiavelli, R. C. Pardo, A. Richard, M. A. Riley, G. Savard, M. Scheck, D. Seweryniak, M. K. Smith, R. Vondrasek, and A. Wiens. Direct Evidence of Octupole Deformation in Neutron-Rich ^{144}Ba. *Phys. Rev. Lett.*, 116:112503, Mar 2016.

[126] E. H. Wang *et al.* (Submitted to Phys. Rev. C).

[127] Y. J. Chen, S. J. Zhu, J. H. Hamilton, A. V. Ramayya, J. K. Hwang, M. Sakhaee, Y. X. Luo, J. O. Rasmussen, K. Li, I. Y. Lee, X. L. Che, H. B. Ding, and M. L. Li. Search for octupole correlations in neutron-rich ^{148}Ce nucleus. *Phys. Rev. C*, 73:054316, May 2006.

[128] A. H. Thibeault, E. H. Wang, C. J. Zachary, J. H. Hamilton, A. V. Ramayya, B. M Musangu, J. O. Rasmussen, Y. X. Luo, G. M. Ter-Akopian, Yu. Ts. Oganessian, and S. J. Zhu. New Determination of the Mo-Ba yield matrix for ^{252}Cf. In J. H. Hamilton, A. V. Ramayya, and P. Talou, editors, *Proceedings of the Sixth International Conference on Fission and Properties of Neutron-Rich Nuclei*, pages 255–259, Singapore, 2017. World Scientific.

[129] B. M. Musangu, A. H. Thibeault, T. H. Richards, E. H. Wang, J. H. Hamilton, C. J. Zachary, J. M. Eldridge, A. V. Ramayya, Y. X. Luo, J. O. Rasmussen, G. M. Ter-Akopian, Yu. Ts. Oganessian, and S. J. Zhu. Anomalous neutron yields confirmed for Ba-Mo and newly observed for Ce-Zr from spontaneous fission of ^{252}Cf. *Phys. Rev. C*, 101:034610, Mar 2020.